

THE STABILITY AND TRANSITION OF
THE COMPRESSIBLE BOUNDARY-LAYER
FLOW OVER BROAD ROTATING CONES

Thesis submitted for the degree of Doctor of Philosophy

at the University of Leicester

by

Paul David Towers

Department of Mathematics

2013

This thesis is dedicated to my nephews

Oliver William & Charlie Austin Inder.

Declaration

This thesis outlines research carried out in the Department of Mathematics at the University of Leicester between October 2009 and March 2013. It contains 22,518 words and 29 figures, which does not exceed the word limit set by the College of Science & Engineering. This thesis is my own work and includes nothing which is the result of work done in collaboration. No part of this research has been submitted to any other university or place of learning for any qualification.

Paul David Towers

Department of Mathematics

University of Leicester

March 2013

Summary

The subject of fluid flows over axisymmetric bodies has increased in recent times, as they can be used to model flows over a swept wing, spinning projectiles and aeroengines amongst other things. A better mathematical understanding of the transition from laminar to turbulent flow within the boundary layer could lead to an improvement in the design of such applications.

We consider a compressible fluid flow over a rotating cone, defined by half-angle ψ . The mean flow boundary-layer equations are derived and we conduct a high Reynolds number asymptotic linear stability analysis. The flow is susceptible to instabilities caused by inviscid crossflow modes (*type I*) and modes caused by a viscous-Coriolis balance force (*type II*). Both are considered, along with the effects of changes in the cone half-angle, the magnitude of the local Mach number and the temperature at the cone wall. A surface suction along the cone wall is also analysed.

Acknowledgements

First and foremost I would like to thank my supervisor Dr. Stephen Garrett. His advice and guidance, both academically and on a personal level, has been invaluable throughout my time at Leicester. I would also like to thank Dr. Zahir Hussain for some helpful discussions regarding his own PhD thesis.

I am grateful to the Engineering and Physical Sciences Research Council for the financial support I have received.

My final thank you is to my family and friends for their endless support throughout this process. A special thank you must go to Marie, James, Oliver & Charlie Inder for letting me stay with them upon request during the second half of this project.

Contents

Declaration	i
Summary	ii
Acknowledgements	iii
1 Introduction	1
2 Laminar flow equations	20
2.1 The governing equations	22
2.2 Solution of the governing equations	29
2.3 Physical interpretation	37
2.4 The effect of mass flux on the laminar flow solution	41
3 Inviscid type I modes	44
3.1 Linear perturbation equations	44

3.2	Type I perturbation functions	48
3.3	Leading order eigenmodes	50
3.4	Wall layer solution	57
3.5	First order eigenmodes	59
4	Viscous Type II Modes	62
4.1	Upper deck solutions	65
4.2	Main deck solutions	69
4.3	Lower deck solutions	71
4.4	First order lower-deck solutions	75
4.5	Wavenumber and waveangle predictions	87
5	Conclusions	95
5.1	Current work	98
5.2	Future work	102
	Bibliography	106

List of Figures

1.1	Experimental visualisation of the flow over a disk with radius 200mm rotating at 1500 revolutions per minute. Taken by Kohama (1984a).	2
1.2	A numerical study into the neutral stability curves for an incompressible flow over a rotating disk, showing the upper branch <i>type I</i> modes and the lower branch <i>type II</i> modes. Taken from Malik (1986).	4
1.3	Space–time diagrams for disturbances defined as (a) convectively unstable and (b) absolutely unstable. Taken from Lingwood (1996)	5
1.4	A comparison for the required wave angle for the onset of the type I instability for experimental, asymptotic (ϕ) and numerical studies (ϵ). Taken from Garrett, Hussain & Stephen (2009) .	11

1.5	Experimental visualisation of the flow over a cone with half angle $\psi = 15^\circ$ rotating at 670 revolutions per minute. Taken by Kobayashi, Kohama & Kurosawa (1983).	17
2.1	Geometrical setup for the rotating cone (taken from Garrett (2002)).	21
2.2	Solution of $\Psi(--)$, $U(-)$, $-V(..)$	31
2.3	Varying wall temperature, increasing vertically from $T_w = 0 - 2$ in 0.4 increments, for constant local Mach numbers M_x	34
2.4	Varying local Mach number, increasing vertically from $M_x = 0 - 10$ in increments of 2, for constant wall temperatures T_w	35
2.5	Numerical solution for (a) $f(-)$, $f'(--)$ and (b) $q(-)$, $q'(--)$	36
2.6	Solution of $U(-)$, $V(--)$ and $W(-)$, for $\psi = 90^\circ$	38
2.7	Physical laminar flow profiles $U(-)$, $V(--)$, $W(..)$ for $\psi = 40^\circ$ (uppermost) $- 90^\circ$, $T_w = 1$ with (a) $M_x = 0.5$ and (b) $M_x = 6$	39
2.8	Physical laminar flow profiles $U(-)$, $V(--)$, $W(..)$ for $\psi = 40^\circ$ (uppermost) $- 90^\circ$, $M_x = 1$ with (a) $T_w = 0.5$ and (b) $T_w = 3$	40
2.9	Varying suction parameter from $a = 0.2$ to $a = 1$ (uppermost) in increments of 0.2, for cone half angles ψ , where $U(-)$, $V(--)$ and $W(-)$	43

3.1 The effective velocity $\overline{U}(-)$ and it's second derivative $\overline{U}''(-)$
 for $\psi = 40^\circ$ (uppermost at $z = 10$)– 90° , where $T_w = M_x = \frac{1}{2}$. . . 51

3.2 Diagram showing the direction of wave numbers and the effective velocity, taken from Garrett, Hussain & Stephen (2009). . . 52

3.3 w_0 for $\psi = 40^\circ$ (uppermost) – 90° where $T_w = \frac{1}{2}, M_x = \frac{1}{2}$ 54

3.4 w_0 for $\psi = 40^\circ$ (uppermost) – 90° where $T_w = \frac{1}{2}, M_x = 1$ 54

3.5 w_0 for $\psi = 40^\circ$ (uppermost) – 90° where $T_w = 1, M_x = 1$ 55

3.6 w_0 for $\psi = 60^\circ, T_w = \frac{1}{2}, M_x = 1$ with suction parameter $a =$
 0(uppermost), 0.1, 0.2. 55

3.7 Asymptotic plots of leading order wavenumber & waveangle predictions for neutrally stable inviscid modes 56

4.1 Diagram of the triple-deck structure. 63

4.2 The graph of $U(0, \theta)$, showing the decay over the region of integration from $\theta = 0$ to $\theta = 5$ 83

4.3 The effective wavenumber $\gamma_0 x^{\frac{1}{2}}$ for fixed $T_w = 0.4, 0.8, 1.0, 1.2, 1.6$.
 The solution for the incompressible case is also given (–). 87

4.4 The correction to the wave angle for fixed $T_w = 0.4, 0.8, 1.0, 1.2, 1.6$.
 The solution for the incompressible case is also given (–). 88

4.5	The correction to the wave angle for $T_w = 1$, with $\psi = 40^\circ - 90^\circ$ in 10° increments.	89
4.6	Asymptotic wavenumber and waveangle predictions for the vis- cous type II modes, for fixed $T_w = M_x = 1$ and varying $\psi =$ $40^\circ - 90^\circ$	92
4.7	Asymptotic wavenumber and waveangle predictions for the vis- cous type II modes, for fixed $\psi = 60^\circ, M_x = 1$ and varying $T_w = 0.4, 0.8, 1.2, 1.6$	93
4.8	Asymptotic wavenumber and waveangle predictions for the vis- cous type II modes, for fixed $\psi = 60^\circ, T_w = 1$ and varying $M_x = 0.3, 0.6, 0.9, 1.2$	94

List of Tables

4.1	The effect of a change in ψ on the maximum local Mach number	
	M_x^{max} allowed for stationary three-dimensional modes of instability to exist.	69

Chapter 1

Introduction

This thesis presents a study of the stability of compressible boundary-layer flows over rotating cones, defined by half-angle ψ . The boundary-layer flow driven by a rotating disk is a special case of the rotating-cone flow when $\psi = 90^\circ$, and that particular geometry has received a huge amount of attention in the literature. Interest in the rotating-disk flow started with the combined theoretical and experimental work by Gregory, Stuart & Walker (1955). Their experimental study showed that a laminar flow was maintained within the small region around the centre of the rotation, with spiral vortices appearing at an increased radial distance. The spiral vortices were observed to be co-rotating and stationary with respect to the disk surface. As the radial position was increased yet further, transition to turbulent flow was observed.

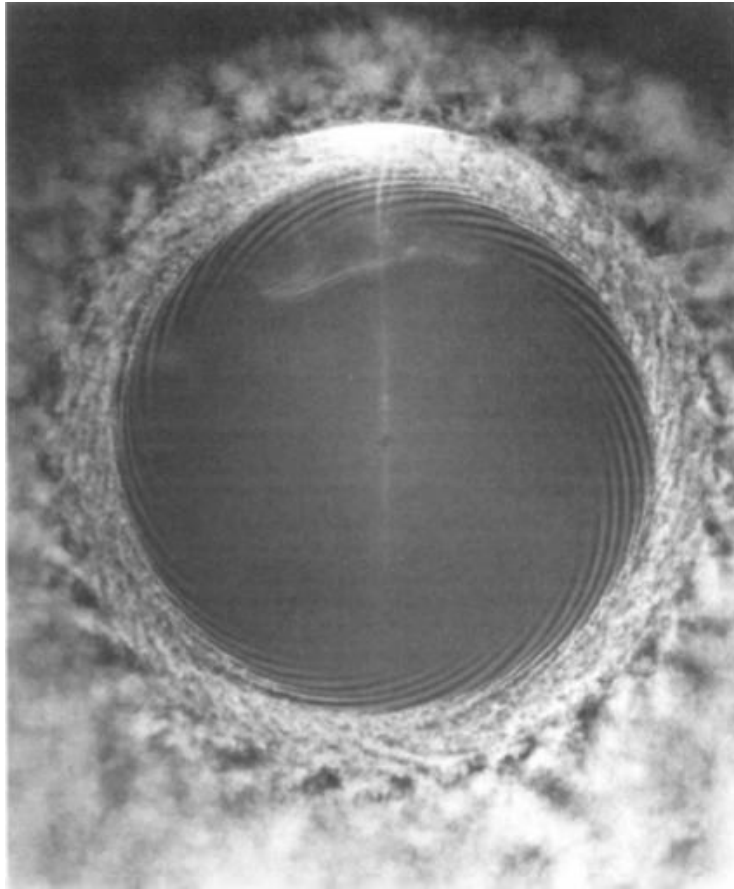


Figure 1.1: Experimental visualisation of the flow over a disk with radius 200mm rotating at 1500 revolutions per minute. Taken by Kohama (1984a).

This is highlighted in Figure 1.1, a flow visualisation taken from experimental work by Kohama (1984a). The cause of the spiral vortices within the boundary layer was confirmed to be the presence of an inviscid cross-flow instability, which is also the dominant convective instability mechanism found for a flow over a swept wing. This connection to the swept-wing flow has

since motivated the huge interest in the rotating disk, not least because of its relatively simple geometry.

Before Gregory, Stuart & Walker (1955), the very first study of the rotating-disk flow was due to Kármán (1921), who obtained the equations that governed steady boundary-layer flow. von Kármán's approach was to solve the Navier–Stokes equations in the appropriate geometry (which are partial differential equations) by using a similarity solution that scaled out the radial dependence, which led to ordinary differential equations which are much easier to solve. The resulting theoretical flow profiles were later verified by Cochran (1934). The aforementioned study by Gregory, Stuart & Walker (1955) followed some years later and was the first to consider the stability of steady boundary-layer flow, however the theoretical component of their study relied on von Kármán's earlier results.

We now present a short summary of the literature relevant to this thesis that includes a summary of developments of the knowledge of the rotating-disk flow and that over related three-dimensional bodies, including the rotating cone. The summary is necessarily short and focussed, and a fuller review of the early work is given by Reed & Saric (1989).

In their stability analysis, Gregory, Stuart & Walker (1955) neglected viscous terms, yielding results for what have become known as the inviscid *type*

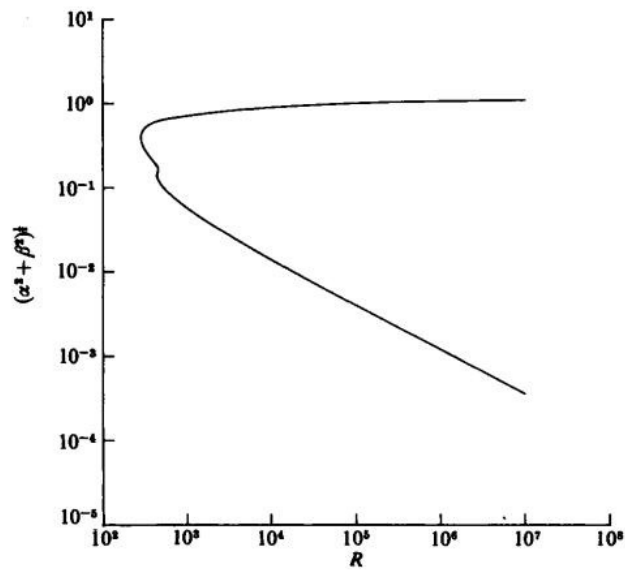


Figure 1.2: A numerical study into the neutral stability curves for an incompressible flow over a rotating disk, showing the upper branch *type I* modes and the lower branch *type II* modes. Taken from Malik (1986).

I modes, shown by the upper branch of Figure 1.2. Some years later, a fuller numerical investigation of the linear stability of the rotating-disk flow was presented by Malik (1986), which was closely followed by a linear asymptotic analysis by Hall (1986). Both approaches demonstrated the existence of an additional instability mode, the *type II* mode shown by the lower branch of Figure 1.2, and good agreement was found between the asymptotic and numerical neutral curves in the high Reynolds-number limit. Hall formally demonstrated that the type II mode was viscous in origin and was caused

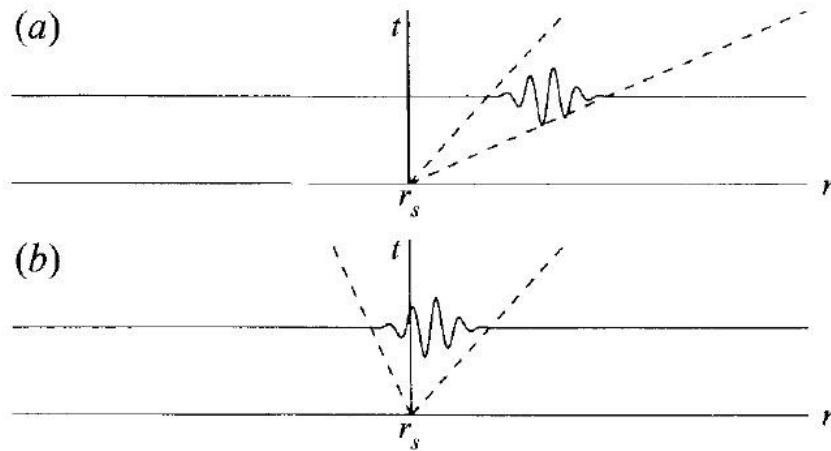


Figure 1.3: Space–time diagrams for disturbances defined as (a) convectively unstable and (b) absolutely unstable. Taken from Lingwood (1996)

by a balance between viscous and Coriolis forces. Type II modes could not, therefore, be described by an inviscid theory. The asymptotic study showed that the type II mode has a triple deck structure and Hall’s study was later extended to consider the non-linear development of the stationary modes by MacKerrell (1987). MacKerrell found that including non-linear terms led to a more unstable flow compared to the linear analysis, suggesting that non-linear effects were destabilising.

In addition to type I and II modes, which are example of convective instabilities and can be associated with the experimentally observed spiral vortices, Lingwood (1995) was the first to show that the flow over a rotating disk was

locally absolutely unstable. A space–time diagram of the evolution of absolute and convective instabilities are shown in Figure 1.3. Lingwood noticed the close match between her predicted critical Reynolds number for the onset of absolute instability and the reported critical Reynolds numbers for the onset of turbulence from various experimental studies over the prior years, for examples see Malik, Wilkinson & Orszag (1981), Kobayashi, Kohama & Takamada (1980). More specifically, experimentally observed values for transition were found to have an average critical Reynolds number of 513, and Lingwood’s prediction for the onset of absolute instability differed by less than 3% of this value. This led to the suggestion that absolute instability may be closely associated with the onset of turbulent flow.

Following this discovery, Lingwood (1996) obtained experimental results for the stability of a rotating-disk flow, considering both unexcited and excited flows. In the case of an unexcited flow, where no artificial disturbance is made to the flow, the stationary waves grew as the Reynolds number is increased, leading to transitional behaviour between $R = 502$ and $R = 514$ and fully turbulent by $R \approx 600$. However, before $R = 502$ there is no prior sign of any features of transition. This region coincides with the region of theoretical absolute instability and added weight to the original assertion that absolute instability is related to the onset of turbulence.

A few years later, Davies & Carpenter (2003) performed direct numerical simulations solving the linearized Navier–Stokes equations directly on a disk of infinite extent. When they made the same homogeneous flow approximation as in Lingwood’s theoretical analysis (i.e. the parallel-flow approximation), they recovered her results in full, with absolute instability clearly present at high Reynolds number. However, when the spatial inhomogeneity of the boundary layer was included there was no evidence that absolute instability gives rise to an unstable global oscillator in the long-time response that would be required to give the onset of transition within a purely linear theory. Indeed their study suggested that convective behaviour eventually dominates at all the Reynolds numbers investigated, even for strongly absolutely unstable regions. Thereby suggesting that absolute instability was not involved in the transition process through linear effects. This result is entirely consistent with Itoh (2001a,b) who had raised the point that the spatial modulation of the dispersion relation, from which instability types are determined, may yield significant effects on the spatial and temporal development of instability waves. Hence, because a parallel-flow approximation causes the dispersion relation to have no dependence on any spatial coordinate, it cannot be justified.

Following this, Pier (2003) demonstrated that a nonlinear approach is required to explain the self-sustained behaviour of the rotating-disk flow that

leads to turbulence. Using the result of Huerre & Monkewitz (1990) that the presence of local absolute instability does not necessarily give rise to linear global instability, Pier suggested that the flow has a primary nonlinear global mode that is fixed by the onset of the local absolute instability which has a secondary absolute instability that triggers the transition to turbulence. Some experimental evidence for a secondary instability exists (Kohama (1984a) and Imayama, Alfredsson & Lingwood (2012)), but the behaviour of the secondary instability and also its relation to the primary absolute instability are not fully understood as yet.

In an attempt to explain Lingwood's original experimental observations in the light of the subsequent theoretical developments, Healey (2010) presents a theory, based on the Ginzburg–Landau equation, that suggests that there can be a linear global instability when there is local instability at the *edge* of the disk. The finite size of experimental disks is of course a crucial difference between experimental and theoretical studies prior to Healey's work, and edge effects were a new addition to the arguments in the literature. The very recent experimental study of Imayama, Alfredsson & Lingwood (2013) finds that edge effects may indeed lead to linear global instability as a first step in the onset of transition. Discussions in the literature continue as to the actual mechanism by which transition to turbulence occurs in the boundary–layer flow over a

rotating disk.

The discovery of absolute instability and the associated interest in the rotating-disk flow within the literature has led to a renewed interest in the instability mechanisms found within boundary-layer flows over other axisymmetric, rotating bodies, such as cones. This flow is the subject of this thesis. Aside from the theoretical interest in the abstract flow, very similar flows exist in engineering applications, for example over the nose of a rotating missile or over rotating aeroengine components. Hence, even though the interest in the rotating disk was initiated by its relationship to the swept-wing flow, the results of studies of rotating-cone flows have a more immediate application.

Early experimental work for the rotating cone in an otherwise still fluid was carried out by Kappesser, Greif & Cornet (1973); Kreith, Ellis & Giesing (1962) and Tein & Campbell (1963). These experiments were limited to measuring the critical Reynolds number for the onset of turbulent flow and very little was known about the mechanisms causing the transition. However, during the 1980s, progress was made towards an understanding of the instabilities at work. In particular, spiral vortices were found to be present in the transitional region of the boundary layer (see Kobayashi, Kohama & Kurosawa (1983); Kobayashi & Izumi (1983); Kohama (1984b)), similar to those observed in the

rotating-disk flow. This breakthrough was found using a high speed strobe light flow visualisation technique which showed the spiral vortices emanating from the surface of the cone. The spiral vortices are stationary with respect to the cone, regardless of the cone's rate of rotation Ω^* .

In contrast to the observations on rotating disks, where counter-rotating vortices are always seen, the structure of the spiral vortices over a cone was seen to depend on the half-angle, ψ , of the cone. In the experimental study by Kobayashi & Izumi (1983), the spiral vortices on cones with slender half-angles are shown to take the form of pairs of counter-rotating vortices, similar to Görtler vortices that are known to arise from centrifugal forces present in the flow field found by Hussain, Stephen & Garrett (2012). However, as the half-angle increases through $\psi = 30^\circ$, the spiral vortices appear to take the form of co-rotating cross-flow vortices, as seen on the rotating disk. As mentioned above, the co-rotating vortices on the rotating disk appear because of an underlying cross-flow instability, and are caused by the inflectional nature of the flow. Hence the observed centrifugal instability for cones with sufficiently small half angle, along with the cross-flow instability for broader cones, show that there is a distinct variation in the dominant instability mechanism for slender cones, which is not seen on broad cones or on a disk (where $\psi = 90^\circ$). (This is further discussed by Garrett, Hussain & Stephen (2009), who have

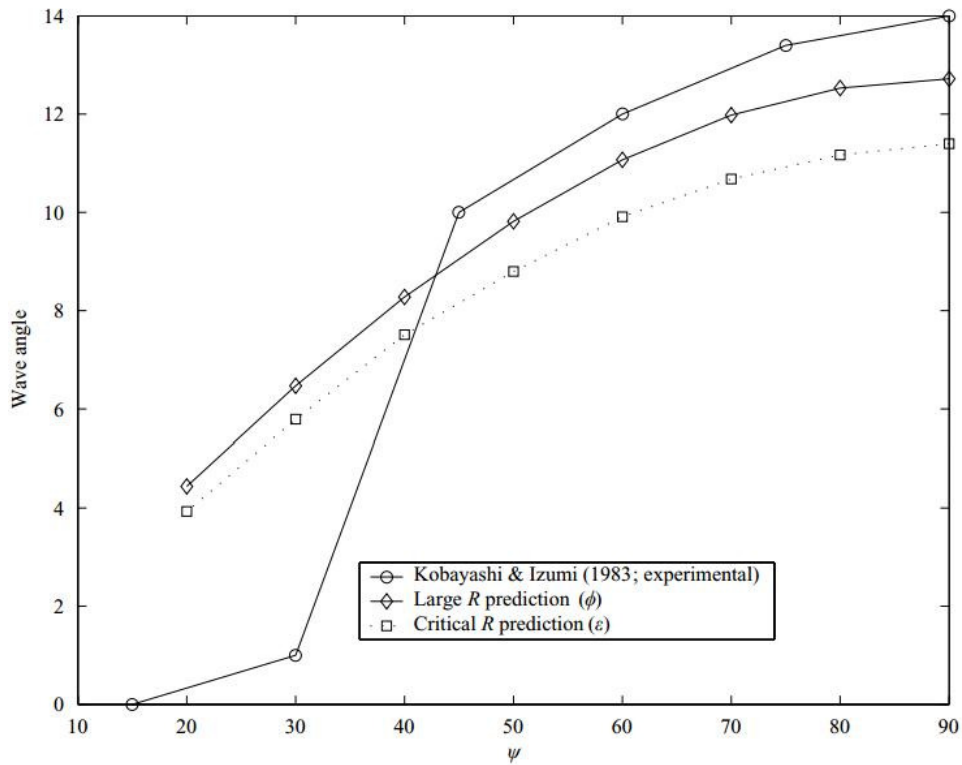


Figure 1.4: A comparison for the required wave angle for the onset of the type I instability for experimental, asymptotic (ϕ) and numerical studies (ϵ). Taken from Garrett, Hussain & Stephen (2009)

recently identified an alternative Görtler-type mode and continue to work on its properties.)

With regards theoretical studies of instabilities within the rotating-cone boundary-layer flows, Garrett (2002) considers the problem in still fluid and uses a numerical approach. A parallel-flow approximation is used in a study

similar to Lingwood (1995) work and also includes both viscous and streamline-curvature effects. The resulting dispersion relation for the rotating-cone flow is then formed and both the convective and absolute instabilities of the problem were investigated at each half-angle. Garrett found that when expressing the transition points found experimentally by Kobayashi & Izumi (1983) in terms of the local Reynolds number, his results for transition were roughly the same for all cones with half-angle $\psi \geq 40^\circ$. This suggests that it may well be possible that the instability mechanism for transition to turbulent flow is the presence of absolute instability for cones with $\psi \geq 40^\circ$. However, for $\psi \leq 40^\circ$ the local Reynolds number at the experimental transition point reduces in magnitude sharply as the half-angle decreases, as shown in Figure 1.4. This suggests that for smaller half angles absolute instability is suppressed and some other transition mechanism must be forcing the turbulent flow.

Recently Hussain (2009) extended Hall's work and presented a linear asymptotic analysis of the type I and type II modes of instability within the boundary-layer flow over the family of rotating cones in otherwise still fluid, as well as the rotating disk and cone within an oncoming axial flow. As would be expected, his results were in good agreement with those of Hall (1986) in the limit $\psi = 90^\circ$. For both numerical and asymptotic results it is seen that an increase in the cone half-angle ψ has a stabilising effect on both the type I and type

II modes of instability, as the predicted value of the critical Reynolds number required to cause the onset of turbulence is increased. As with the numerical results found by Garrett (2002), the asymptotic results are only in agreement with the experimental results for a cone half-angle $\psi \geq 40^\circ$, and a different analysis is needed below this value. Because of this the study presented here will focus on broad cones.

Lingwood (1997) and Lingwood & Garrett (2011) both study the effects of adding a uniform surface suction in the normal direction along the surface of a rotating body. They suggest that suction could be used as a stabilising mechanism by delaying the inset of turbulence, which is in agreement with previous experimental work by Gregory & Walker (1960). In this work we shall also consider a surface suction for the compressible flow, and compare how significant any changes in the flow are compared to the previous results for the incompressible case.

For further studies into the incompressible boundary-layer flow over a rotating cone see Garrett & Peake (2007), Garrett, Hussain & Stephen (2009), Garrett (2010), Garrett, Hussain & Stephen (2010), Hussain, Stephen & Garrett (2012).

The majority of research into boundary-layer stability for incompressible flows

started by finding a basic velocity profile, usually some variation on the well known von Kármán basic steady flow; see Kármán (1921). However, when considering a compressible flow case, the basic flow is much more complex to evaluate. The main cause of this is, as discussed by Stewartson (1964) amongst others, the introduction of several parameters. These include the Prandtl number, which is related to temperature, and the second coefficient of viscosity, also known as the volume viscosity. These do not appear as constants, as they do in the incompressible case. This complication has naturally led to more investigation, and hence greater advances and understanding, of incompressible flows. However, suitable progress relevant to this current study has been made.

Around the same time as Lingwood's studies of absolute instability for an incompressible flow over a rotating disk, Cole (1995) was conducting a study of three-dimensional compressible boundary-layers, where he also concluded that the flow over a rotating disk is absolutely unstable. He numerically solved the three-dimensional inviscid compressible Rayleigh equation, finding branch points leading to absolute instability at scaled Mach numbers 0,1 and 2. The case of a suitably small Mach number, usually approximately $Ma \leq 0.3$, relates to an essentially incompressible flow. Hence for the branch point found with scaled zero Mach number, Cole's results should have compared favourably to the findings by Lingwood. However there were obvious discrepancies be-

tween the two sets of results, with the wave angles corresponding to absolutely unstable flow differing.

Although briefly considered by, amongst others, Solan, Olek & Toren (1983), it was not until the early 1990s that interest in instabilities of compressible flows increased, but the vast majority was focused on mixing layers and shear flows. The first study into the possible absolute and convective stability of a compressible flow over a rotating disk was by Turkyilmazoglu, Cole & Gajjar (2000). The aim was to find the mathematical reasoning behind the differing results of Lingwood and Cole by considering the compressible flow case. In addition, they sought to investigate the effects that compressibility has on the absolute instability of the three-dimensional flow over a rotating disk. It was found that the restrictions assumed by Lingwood, that the disturbances would only grow in the radial direction, could not be justified for a three-dimensional flow. Cole's analysis was found to be valid as at a fixed location the disturbances may grow locally in any direction, not just radially. However, absolute instability was present in both problem formulations. It was also shown that in general compressibility has a stabilizing effect on the flow, and wall heating is found to be destabilizing (with wall cooling having the opposite effect).

Following theoretical work by Hall (1986) and MacKerrell (1987) into the stabilities of a three-dimensional incompressible flow over a rotating disk, Sed-

dougui (1990) conducted a non-linear study into the effects of compressibility on the stationary modes of instability. It was found that compressibility can have a substantial effect on the stationary viscous modes, as for sufficiently large Mach numbers they cannot exist. However, when the stationary modes do exist, the results show that they are similar in form to those found by MacKerrell for the incompressible case, with any differences being dependent on the wall temperature and not the compressibility itself.

Turkyilmazoglu has been at the forefront of recent research into the stationary and non-stationary modes of instability found for a compressible flow over a rotating disk. A study into the non-stationary viscous lower branch modes (see Turkyilmazoglu (2005)) were similar with the findings by Seddougui, in that he proved that the compressible neutral modes only exist for limited Mach number, and that there exists a critical frequency value for which no solutions are found. Again a triple deck asymptotic structure was studied, rather than using a parallel-flow approximation, and concluded that the linear modes are stabilized by high wall cooling and destabilized for wall insulation and heat transfer cases as the local Mach number grows.

However, in a later study (see Turkyilmazoglu (2007)), it was found that the reverse effect was observed for the evolution of the non-linear modes. By considering finite amplitudes the non-stationary modes which have negative

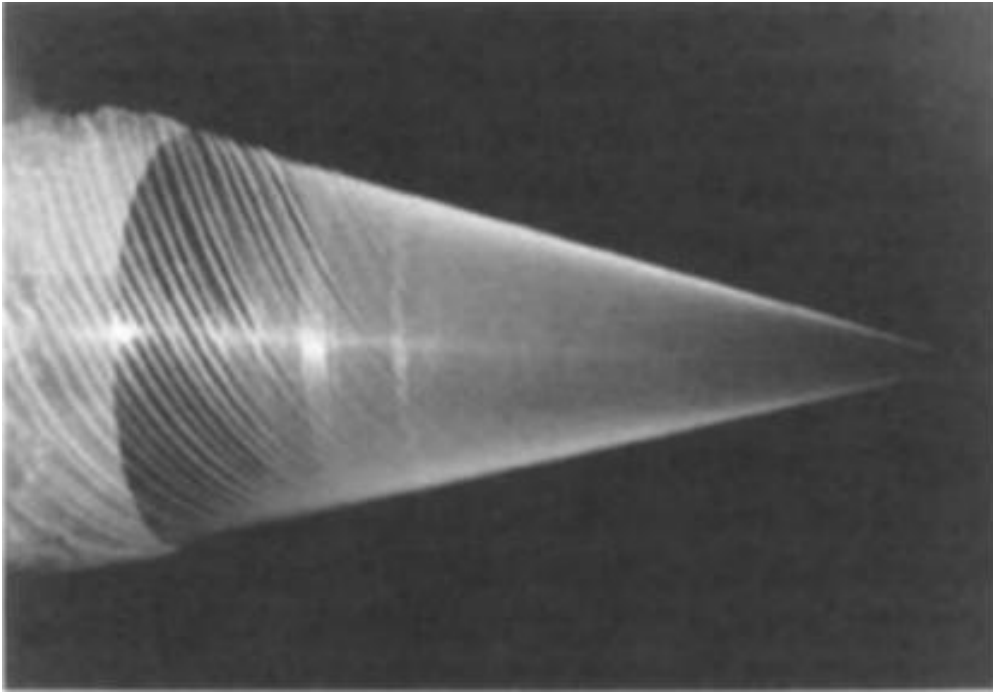


Figure 1.5: Experimental visualisation of the flow over a cone with half angle $\psi = 15^\circ$ rotating at 670 revolutions per minute. Taken by Kobayashi, Kohama & Kurosawa (1983).

frequencies are similar to those found by Seddougui for the stationary modes. But differences were found for the positive frequency waves, especially when considering wall cooling, where it is shown that non-linearity is destabilizing for all modes.

The motivation for this thesis is to extend previous work by Hall (1986), Seddougui (1990) and Hussain (2009), to consider the effect of compressibility on

a rotating cone flow for half angle ψ . This configuration has industrial applications, such as spinning projectiles and aeroengines. Understanding the instability mechanisms of the rotating–cone flow will enable us to find ways of controlling the laminar–turbulent transition within the boundary layer. This would lead to performance improvements in the aforementioned applications. For example, for spinning projectiles, being able to control turbulence within the boundary layer would have a positive effect on control and accurate targeting. In aeroengines it would help fuel efficiency by reducing drag. We will consider how changes in the cone’s wall temperature effects the stability characteristics, as well as changes in the local Mach number. A surface suction along the cone wall will also be considered by introducing a non-zero boundary condition in the normal direction.

We begin by formulating the mean flow equations, commonly known as the Kármán equations. Here we will consider the effects of wall temperature, local Mach number and surface suction on the basic flow profiles. Theoretically, we would expect changes in these parameters to effect the basic flow profiles in a similar way to the instability modes, hence it is important to know how these alter the flow. The linear disturbance equations are then formulated, from which we identify the upper branch inviscid modes. These are referred to as the type I modes, where the instabilities captured are those away from

the cone wall. We study the change in behaviour as the half angle ψ is varied, as well as the effect of a surface suction. The viscous type II modes are then considered, which captures the instabilities near to the cone wall. In the literature the type I modes are said to be caused by a crossflow instability, and the type II modes cause by a streamline curvature instability. We will discuss the results in relation to the previous studies into compressible and incompressible boundary-layer flows over rotating bodies.

Chapter 2

Laminar flow equations

We shall consider a cone placed in an otherwise still compressible fluid, which rotates about its axis of symmetry with angular velocity Ω^* (where superscript $*$ denotes dimensional quantities). The fluid flow is driven by the rotation of the cone, and we shall take into account the effects of streamline curvature and Coriolis forces. The angle between the cone's surface and its axis of symmetry is defined as the cone half-angle ψ .

The geometry is shown in Figure 2.1 and is formulated using Cartesian coordinates (X^*, Y^*, Z^*) with the origin placed at the tip of the cone. This is then transformed to the orthogonal curvilinear coordinates (x^*, θ, z^*) which respectively represent a streamwise coordinate, an azimuthal coordinate and

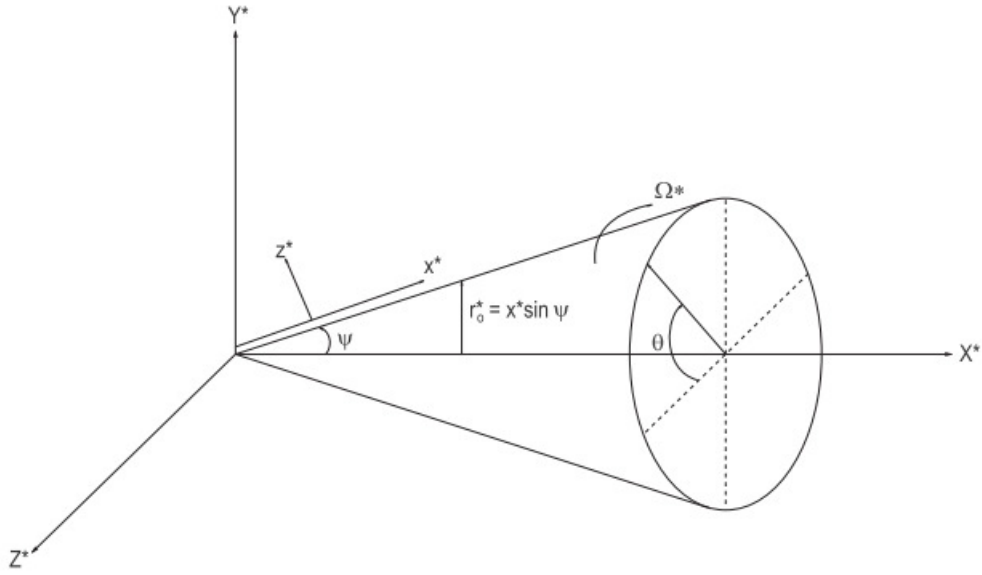


Figure 2.1: Geometrical setup for the rotating cone (taken from Garrett (2002)).

a surface-normal coordinate. The coordinate transformation is given by

$$X^* = x^* \cos \psi - z^* \sin \psi, \quad (2.1)$$

$$Y^* = (x^* \sin \psi + z^* \cos \psi) \sin \theta, \quad (2.2)$$

$$Z^* = (x^* \sin \psi + z^* \cos \psi) \cos \theta; \quad (2.3)$$

with the scale factors of the orthogonal curvilinear coordinates (x^*, θ, z^*) being given by $h_x = h_z = 1$ and $h_\theta = h^* = x^* \sin \psi + z^* \cos \psi$, where $r_0^* = x^* \sin \psi$ defines the local surface radius of the cone.

This formulation is consistent with both Garrett (2002) and Hussain (2009),

who consider the incompressible case of the rotating–cone boundary–layer flow. This study of the compressible case is a generalisation of work done by Turkyilmazoglu (2004) for the particular case of a rotating disk ($\psi = 90^\circ$).

2.1 The governing equations

As with the incompressible case we use a continuity equation and the Navier–Stokes equations. As we are considering a compressible fluid these equations alone are not sufficient, due to the fluid having a non–constant density. Hence we also require a state equation and an energy equation. The equations are applied in a reference frame rotating with angular velocity Ω^* about the X^* -axis, and are given by

$$\frac{\partial \rho^*}{\partial t} + \nabla \cdot (\rho^* \mathbf{u}) = 0, \quad (2.4)$$

$$\begin{aligned} \frac{D\mathbf{u}}{Dt} + 2\boldsymbol{\Omega} \times \mathbf{u} + (\boldsymbol{\Omega} \times \boldsymbol{\Omega}) \times \mathbf{r} = & \frac{1}{\rho^*} (\nabla (\lambda^* \nabla \cdot \mathbf{u}) - \nabla p^* \\ & + \nabla \left(\mu^* \sum_{j=1}^3 e_{ij} \right), \end{aligned} \quad (2.5)$$

$$\gamma M_\infty^2 p = \rho T, \quad (2.6)$$

$$\begin{aligned} \rho^* \frac{Dh}{Dt} = & \frac{Dp^*}{Dt} + \nabla \cdot (k^* \nabla T^*) + \mu^* (2e_{11}^2 + 2e_{22}^2 + 2e_{33}^2 \\ & + e_{12}^2 + e_{13}^2 + e_{23}^2) + \lambda^* (\nabla \cdot \mathbf{u})^2, \end{aligned} \quad (2.7)$$

where the Coriolis forcing term $2\boldsymbol{\Omega} \times \mathbf{u}$ appears due to the rotating frame. Note that this is in contrast to Garrett (2002) formulation, who uses a stationary frame and so does not have the Coriolis term.

The vector $\mathbf{u} = (u^*, v^*, w^*)$ denotes the velocity flow field and $\mathbf{r} = (x^*, 0, z^*)$ gives the position vector. The parameters given in Equations (2.4)-(2.7) are defined as: ρ^* the density; p^* the pressure; λ^* the second coefficient of viscosity related to the bulk viscosity; μ^* the dynamical viscosity; M_∞ the free stream Mach number; T^* the temperature; and h the enthalpy (where h is distinct from the previously defined scale factors). The heat capacity ratio γ is the ratio of the heat capacity at constant pressure c_p to the heat capacity at constant volume c_v . The parameter k is that associated with the Prandtl number σ , where $k\sigma = c_p\mu$. The components of the strain tensor e_{ij} are given by,

$$\begin{aligned} e_{11} &= \frac{\partial u^*}{\partial x^*}, \\ e_{12} = e_{21} &= \frac{1}{2} \left(\frac{\partial v^*}{\partial x^*} + \frac{1}{h^*} \frac{\partial u^*}{\partial \theta} - \frac{v^* \sin \psi}{h^*} \right), \\ e_{13} = e_{31} &= \frac{1}{2} \left(\frac{\partial w^*}{\partial x^*} + \frac{\partial u^*}{\partial z^*} \right), \\ e_{22} &= \frac{1}{h^*} \frac{\partial v^*}{\partial \theta} + \frac{w^* \cos \psi}{h^*} + \frac{u^* \sin \psi}{h^*}, \\ e_{23} = e_{32} &= \frac{1}{2} \left(\frac{\partial v^*}{\partial z^*} + \frac{1}{h^*} \frac{\partial w^*}{\partial \theta} - \frac{v^* \cos \psi}{h^*} \right), \\ e_{33} &= \frac{\partial w^*}{\partial z^*}. \end{aligned}$$

The coordinate transform (2.1)-(2.3) applied to the governing Equations (2.4)-(2.7) leads to the following full governing equations for the flow in orthogonal curvilinear coordinates,

$$\begin{aligned} \frac{\partial \rho^*}{\partial t^*} + u^* \frac{\partial \rho^*}{\partial x^*} + w^* \frac{\partial \rho^*}{\partial z^*} + \rho^* \left(\frac{\partial u^*}{\partial x^*} + \frac{\partial w^*}{\partial z^*} \right) + \frac{1}{h^*} \left(v^* \frac{\partial \rho^*}{\partial \theta} + \rho^* \frac{\partial v^*}{\partial \theta} \right. \\ \left. + \rho^* (u^* \sin \psi + w^* \cos \psi) \right) = 0, \quad (2.8) \end{aligned}$$

$$\begin{aligned} \rho^* \left(\frac{\partial u^*}{\partial t^*} + u^* \frac{\partial u^*}{\partial x^*} + \frac{v^*}{h^*} \frac{\partial u^*}{\partial \theta} + w^* \frac{\partial u^*}{\partial z^*} - \frac{v^{*2} \sin \psi}{h^*} - 2\Omega^* v^* \sin \psi \right. \\ \left. - \Omega^{*2} h^* \sin \psi \right) = - \frac{\partial p^*}{\partial x^*} + \lambda^* \left(\frac{\partial^2 u^*}{\partial x^{*2}} + \frac{\partial^2 w^*}{\partial x^* \partial z^*} + \frac{1}{h^*} \left(\frac{\partial^2 v^*}{\partial x^* \partial \theta} \right. \right. \\ \left. \left. + \sin \psi \frac{\partial u^*}{\partial x^*} + \cos \psi \frac{\partial w^*}{\partial x^*} \right) - \frac{\sin \psi}{h^{*2}} \left(\frac{\partial v^*}{\partial \theta} + u^* \sin \psi + w^* \cos \psi \right) \right) \\ + \frac{\partial}{\partial x^*} \left(2\mu^* \frac{\partial u^*}{\partial x^*} \right) + \frac{1}{h^*} \frac{\partial}{\partial \theta} \left(\mu^* \left(\frac{\partial v^*}{\partial x^*} + \frac{1}{h^*} \frac{\partial u^*}{\partial \theta} - \frac{v^* \sin \psi}{h^*} \right) \right) \\ + \frac{\partial}{\partial z^*} \left(\mu^* \left(\frac{\partial w^*}{\partial x^*} + \frac{\partial u^*}{\partial z^*} \right) \right), \quad (2.9) \end{aligned}$$

$$\begin{aligned}
\rho^* \left(\frac{\partial v^*}{\partial t^*} + u^* \frac{\partial v^*}{\partial x^*} + \frac{v^*}{h^*} \frac{\partial v^*}{\partial \theta} + w^* \frac{\partial v^*}{\partial z^*} + \frac{v^*}{h^*} (u^* \sin \psi + w^* \cos \psi) \right. \\
\left. + 2\Omega^* (u^* \sin \psi + w^* \cos \psi) \right) = -\frac{1}{h^*} \frac{\partial p^*}{\partial \theta} + \frac{\lambda^*}{h^*} \left(\frac{\partial^2 u^*}{\partial x^* \partial \theta} + \frac{\partial^2 w^*}{\partial \theta \partial z^*} \right. \\
\left. + \frac{1}{h^*} \left(\frac{\partial^2 v^*}{\partial \theta^2} + \sin \psi \frac{\partial u^*}{\partial \theta} + \cos \psi \frac{\partial w^*}{\partial \theta} \right) \right. \\
\left. + \frac{\partial}{\partial x^*} \left(\mu^* \left(\frac{\partial v^*}{\partial x^*} + \frac{1}{h^*} \frac{\partial u^*}{\partial \theta} - \frac{v^* \sin \psi}{h^*} \right) \right) \right. \\
\left. + \frac{1}{h^*} \frac{\partial}{\partial \theta} \left(2\mu^* \left(\frac{1}{h^*} \frac{\partial v^*}{\partial \theta} + \frac{w^* \cos \psi}{h^*} + \frac{u^* \sin \psi}{h^*} \right) \right) \right. \\
\left. + \frac{\partial}{\partial z^*} \left(\mu^* \left(\frac{\partial v^*}{\partial z^*} + \frac{1}{h^*} \frac{\partial w^*}{\partial \theta} - \frac{v^* \cos \psi}{h^*} \right) \right) \right), \quad (2.10)
\end{aligned}$$

$$\begin{aligned}
\rho^* \left(\frac{\partial w^*}{\partial t^*} + u^* \frac{\partial w^*}{\partial x^*} + \frac{v^*}{h^*} \frac{\partial w^*}{\partial \theta} + w^* \frac{\partial w^*}{\partial z^*} - \frac{v^{*2} \cos \psi}{h^*} - 2\Omega^* v^* \cos \psi \right. \\
\left. - \Omega^{*2} h^* \cos \psi \right) = -\frac{\partial p^*}{\partial z^*} + \lambda^* \left(\frac{\partial^2 u^*}{\partial x^* \partial z^*} + \frac{\partial^2 w^*}{\partial z^{*2}} + \frac{1}{h^*} \left(\frac{\partial^2 v^*}{\partial \theta \partial z^*} \right. \right. \\
\left. \left. + \sin \psi \frac{\partial u^*}{\partial z^*} + \cos \psi \frac{\partial w^*}{\partial z^*} \right) - \frac{\cos \psi}{h^{*2}} \left(\frac{\partial v^*}{\partial \theta} + u^* \sin \psi + w^* \cos \psi \right) \right) \\
+ \frac{\partial}{\partial x^*} \left(\mu^* \left(\frac{\partial w^*}{\partial x^*} + \frac{\partial u^*}{\partial z^*} \right) \right) + \frac{1}{h^*} \frac{\partial}{\partial \theta} \left(\mu^* \left(\frac{\partial v^*}{\partial z^*} + \frac{1}{h^*} \frac{\partial w^*}{\partial \theta} - \frac{v^* \cos \psi}{h^*} \right) \right) \\
+ \frac{\partial}{\partial z^*} \left(2\mu^* \frac{\partial w^*}{\partial z^*} \right), \quad (2.11)
\end{aligned}$$

$$\gamma M_\infty^2 p^* = \rho^* T^*, \quad (2.12)$$

$$\begin{aligned}
\rho^* c_p \left(\frac{\partial T^*}{\partial t^*} + u^* \frac{\partial T^*}{\partial x^*} + \frac{v^*}{h^*} \frac{\partial T^*}{\partial \theta} + w^* \frac{\partial T^*}{\partial z^*} \right) &= \frac{\partial p^*}{\partial t^*} + u^* \frac{\partial p^*}{\partial x^*} + \frac{v^*}{h^*} \frac{\partial p^*}{\partial \theta} \\
&+ w^* \frac{\partial p^*}{\partial z^*} + \frac{1}{h^*} \left(\frac{\partial}{\partial x^*} \left(h^* k^* \frac{\partial T^*}{\partial x^*} \right) + \frac{\partial}{\partial \theta} \left(k^* \frac{\partial T^*}{\partial \theta} \right) + \frac{\partial}{\partial z^*} \left(h^* k^* \frac{\partial T^*}{\partial z^*} \right) \right) \\
&+ \mu^* \left(2 \left(\frac{\partial u^*}{\partial x^*} \right)^2 + 2 \left(\frac{1}{h^*} \frac{\partial v^*}{\partial \theta} + \frac{w^* \cos \psi}{h^*} + \frac{u^* \sin \psi}{h^*} \right)^2 + 2 \left(\frac{\partial w^*}{\partial z^*} \right)^2 \right. \\
&\quad + \left(\frac{\partial v^*}{\partial x^*} + \frac{1}{h^*} \frac{\partial u^*}{\partial \theta} - \frac{v^* \sin \psi}{h^*} \right)^2 + \left(\frac{\partial w^*}{\partial x^*} + \frac{\partial u^*}{\partial z^*} \right)^2 \\
&\quad \left. + \left(\frac{\partial v^*}{\partial z^*} + \frac{1}{h^*} \frac{\partial w^*}{\partial \theta} - \frac{v^* \cos \psi}{h^*} \right)^2 \right) \\
&+ \lambda^* \left(\frac{1}{h^*} \left(\frac{\partial}{\partial x^*} (h^* u^*) + \frac{\partial v^*}{\partial \theta} + \frac{\partial}{\partial z^*} (h^* w^*) \right)^2 \right). \quad (2.13)
\end{aligned}$$

The first stage of this study is to solve the steady form of the above equations with appropriate boundary conditions to obtain the steady, laminar flow profiles for each half-angle ψ . These are no slip on the cone wall, the streamwise velocity component tending to zero and a Coriolis balance enforce both conditions at the edge of the cone boundary layer. Mathematically, these are given by

$$\begin{aligned}
u^* = 0, \quad v^* = 0, \quad w^* = 0, \quad T^* = T_w^* \quad \text{on } z^* = 0, \\
u^* \rightarrow 0, \quad v^* \rightarrow -x^* \Omega^* \sin \psi, \quad T^* \rightarrow T_\infty \quad \text{as } z^* \rightarrow \infty. \quad (2.14)
\end{aligned}$$

where T_w^* is the dimensional temperature at the cone's wall. Note that an isothermal boundary condition for the wall temperature has been chosen. In Seddougui (1990) on a compressible flow over a rotating disk, she also considers

an adiabatic condition where $\frac{\partial T}{\partial z} = 0$ at $z = 0$. However, as we are looking to consider the effects of a change in wall temperature, we have chosen the isothermal condition. We will return to the form of these boundary conditions in the presence of surface mass flux in Section 2.4.

Equations (2.8)-(2.13) are then non-dimensionalised. The characteristic length along the cone surface, l^* , is used to scale any length quantities. The surface normal coordinate is further scaled using the modified boundary layer thickness. Hence we arrive at scaled spatial variables

$$x^* = l^* x, \quad z^* = l^* R^{-\frac{1}{2}} \eta, \quad (2.15)$$

where R is the Reynolds number given by

$$R = \frac{\rho^* l^{*2} \Omega^* \sin \psi}{\mu^*}. \quad (2.16)$$

The velocity quantities are then scaled by

$$\mathbf{u}^* = (u^*, v^*, w^*) = l^* \Omega^* \sin \psi (u(x, \eta), v(x, \eta), R^{-\frac{1}{2}} w(\eta)), \quad (2.17)$$

and the pressure is scaled using

$$p^* = \rho^* \Omega^{*2} l^{*2} \sin^2 \psi p(x, \eta). \quad (2.18)$$

The length scale allows us to define the free-stream Mach number by

$$M_\infty = \frac{\Omega l}{(\gamma R_{gas} T_\infty)^{\frac{1}{2}}}$$

where R_{gas} is the gas constant with $R_{gas} = c_p - c_v$. This free stream value is used to scaled the Mach number. Likewise, all other variables are scaled using their free stream values. Again, this method is consistent with Turkyilmazoglu (2004) in the particular case of $\psi = 90^\circ$.

To obtain the governing steady axisymmetric mean flow equations, we neglect any dependence on time and the azimuthal coordinate θ and apply our scalings to Equations (2.8)-(2.13). We then expand in terms of R and dismiss terms of $O(R^{-\frac{1}{2}})$ due to the assumption of large Reynolds number. Physically this limits the analysis to high rotation rates and/or large characteristic length scales relative to the boundary layer thickness and is entirely appropriate.

This leads to the reduced system of equations

$$u \frac{\partial \rho}{\partial x} + w \frac{\partial \rho}{\partial \eta} + \rho \left(\frac{\partial u}{\partial x} + \frac{\partial w}{\partial \eta} \right) + \frac{\rho u}{x} = 0, \quad (2.19)$$

$$\rho \left(u \frac{\partial u}{\partial x} + w \frac{\partial u}{\partial \eta} - \frac{v^2}{x} - 2v - x \right) = -\frac{\partial p}{\partial x} + \frac{\partial}{\partial \eta} \left(\mu \frac{\partial u}{\partial \eta} \right), \quad (2.20)$$

$$\rho \left(u \frac{\partial v}{\partial x} + w \frac{\partial v}{\partial \eta} + \frac{uv}{x} + 2u \right) = \frac{\partial}{\partial \eta} \left(\mu \frac{\partial v}{\partial \eta} \right), \quad (2.21)$$

$$\cot \psi \left(\frac{v^2}{x} + 2v + x \right) = \frac{\partial p}{\partial \eta}, \quad (2.22)$$

$$\gamma M_\infty^2 p = \rho T, \quad (2.23)$$

$$\rho \left(u \frac{\partial T}{\partial x} + w \frac{\partial T}{\partial \eta} \right) = M_\infty^2 (\gamma - 1) \left(u \frac{\partial p}{\partial x} + w \frac{\partial p}{\partial \eta} + \mu \left(\left(\frac{\partial u}{\partial \eta} \right)^2 + \left(\frac{\partial v}{\partial \eta} \right)^2 \right) \right) + \frac{\partial}{\partial \eta} \left(k \frac{\partial T}{\partial \eta} \right). \quad (2.24)$$

subject to the following boundary conditions

$$\begin{aligned}
 u = 0, \quad v = 0, \quad w = 0, \quad \text{on } \eta = 0, \\
 u \rightarrow 0, \quad v \rightarrow -x \sin \psi \quad \text{as } \eta \rightarrow \infty. \\
 \rho, T, \mu \rightarrow 1, \quad p \rightarrow \frac{1}{\gamma M_\infty^2} \quad \text{as } \eta \rightarrow \infty.
 \end{aligned} \tag{2.25}$$

2.2 Solution of the governing equations

To proceed in reducing the equations to a von Kármán type similarity solution we make further assumptions. We let the fluid satisfy Chapman's viscosity law, that is $\mu = CT$ for some constant C which is found experimentally. This is then used to remove the density terms from the equations using a Doronitsyn-Howarth transformation, shown by Stewartson (1964) and given by

$$y = C^{-\frac{1}{2}} \int_0^\eta \rho d\eta. \tag{2.26}$$

We note that in previous work, notably Seddougui (1990), the constant C remains in the analysis throughout. However, when results are presented no value is given for C and it is assumed that the value $C = 1$ is used. This is justified in the conclusions section of this thesis, and hence we set $C = 1$ throughout the analysis presented here.

The velocity and pressure quantities are then further scaled using

$$(u, v, w, p) = (xU(y), xV(y), W(y), (\gamma M_\infty^2)^{-1}) \quad (2.27)$$

We introduce a stream function satisfying Equation (2.4), and given by

$$U = \frac{d\Psi}{dy} = \Psi'(y), \quad (2.28)$$

$$W = -C^{1/2}T \left(2\Psi + x\Psi' \frac{\partial y}{\partial x} \right). \quad (2.29)$$

Applying this to Equations (2.19)-(2.24) leads to the generalised set of von Kármán equations for the compressible flow over a rotating cone, given by

$$\Psi''' = \Psi'^2 - 2\Psi\Psi'' - (V + 1)^2, \quad (2.30)$$

$$V'' = 2(V + 1)\Psi' - 2\Psi V, \quad (2.31)$$

$$\frac{\partial^2 T}{\partial y^2} + 2\sigma\Psi \frac{\partial T}{\partial y} - x\sigma\Psi' \frac{\partial T}{\partial x} + (\gamma - 1)\sigma x^2 M_\infty^2 (\Psi''^2 + V^2) = 0, \quad (2.32)$$

subject to the boundary conditions

$$\Psi(0) = \Psi'(0) = \Psi(\infty) = V(0) = V(\infty) + 1 = T(\infty) - 1 = 0. \quad (2.33)$$

Note that a prime indicates a spatial derivative with respect to y , the transformed normal variable. We consider solving the coupled ordinary differential equations (2.30)-(2.31) together with the boundary conditions (2.33). An implicit fourth-order Runge-Kutta integration method is used to solve the

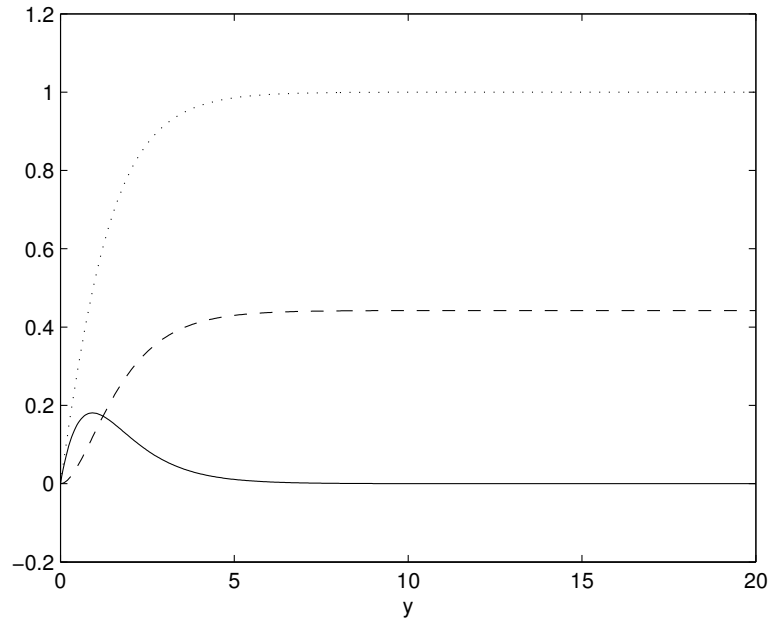


Figure 2.2: Solution of $\Psi(-)$, $U(-)$, $-V(-)$

ODEs. Figure 2.2 shows the solution for the stream function and the stream-wise and negative azimuthal components of the steady laminar flow velocity in the boundary layer of a rotating cone. This is in agreement with the incompressible flow case (Lingwood (1997); Hussain (2009)) due to the removal of the density terms via the Dorotonitsyn-Howarth transformation. However, we will recover the effects of compressibility in §2.3.

In addition to the usual velocity von Kármán equations (2.30)-(2.31), we also have an energy equation (2.32). This contains the extra parameters we must consider due to the effects of compressibility. To proceed further we rewrite

this partial differential equation (PDE) as two ordinary differential equations (ODEs) via the temperature relation originally used by Riley (1964), but used throughout the literature, given by

$$T = 1 - \frac{\gamma - 1}{2} M_x^2 f(y) + (T_w - 1)q(y). \quad (2.34)$$

Here f is a viscous dissipation quantity, q defines a heat conduction term and M_x is the local Mach number defined by $M_x = x \sin \psi M_\infty$. Then (2.32) is expressed as

$$f'' + 2\sigma\Psi f' - 2\sigma\Psi' f = \frac{2\sigma(\Psi''^2 + V'^2)}{\sin^2 \psi} \quad (2.35)$$

$$q'' + 2\sigma\Psi q' = 0 \quad (2.36)$$

We note that Equation (2.36) can be solved analytically, with the solution

$$q(y) = \frac{\int_y^\infty e^{-2\sigma \int_0^y \psi dy} dy}{\int_0^\infty e^{-2\sigma \int_0^y \psi dy} dy} \quad (2.37)$$

The boundary conditions for these ODEs are now considered. The free flow uniform temperature from the boundary equations given in Equation (2.33), along with the heat transfer at the wall, leads to the boundary conditions

$$f(0) = f(\infty) = q(0) - 1 = q(\infty) = 0. \quad (2.38)$$

Using the numerical solutions shown in Figure 2.2 we next solve the ODEs (2.35)-(2.36) subject to the boundary conditions (2.33) and (2.38). We assume

the compressible fluid to be air, which leads to the choice of $\sigma = 0.7$ and $\gamma = 1.4$.

Figure 2.3 shows the temperature distributions for several cases of constant local Mach number with varying wall temperature, which shows agreement with Turkyilmazoglu, Cole & Gajjar (2000) for $M_x = 1$. The effect of the quadratic local Mach number in (2.34) is clear. For $M_x = 1$ the temperature distributions all tend to 1 fairly linearly, whereas in the extreme case given where $M_x = 8$, all profiles grow to a maximum before settling back to 1.

Figure 2.4 shows the temperature distributions for several cases of constant wall temperature with varying local Mach number. Again, it is the local Mach number which is the more dominant parameter. The change in wall temperature merely causes a shift upwards in temperature as expected from Equation (2.34). However, a change in M_x causes a large change in the profiles. For example, near the wall a substantial difference in the temperature can be seen for say $M_x = 2$ and $M_x = 10$.

It is important to note that these laminar flow temperature profiles will play an important role during the stability analysis in later chapters. A change in value of the wall temperature or local Mach number will be seen to effect the stability characteristics of the flow.

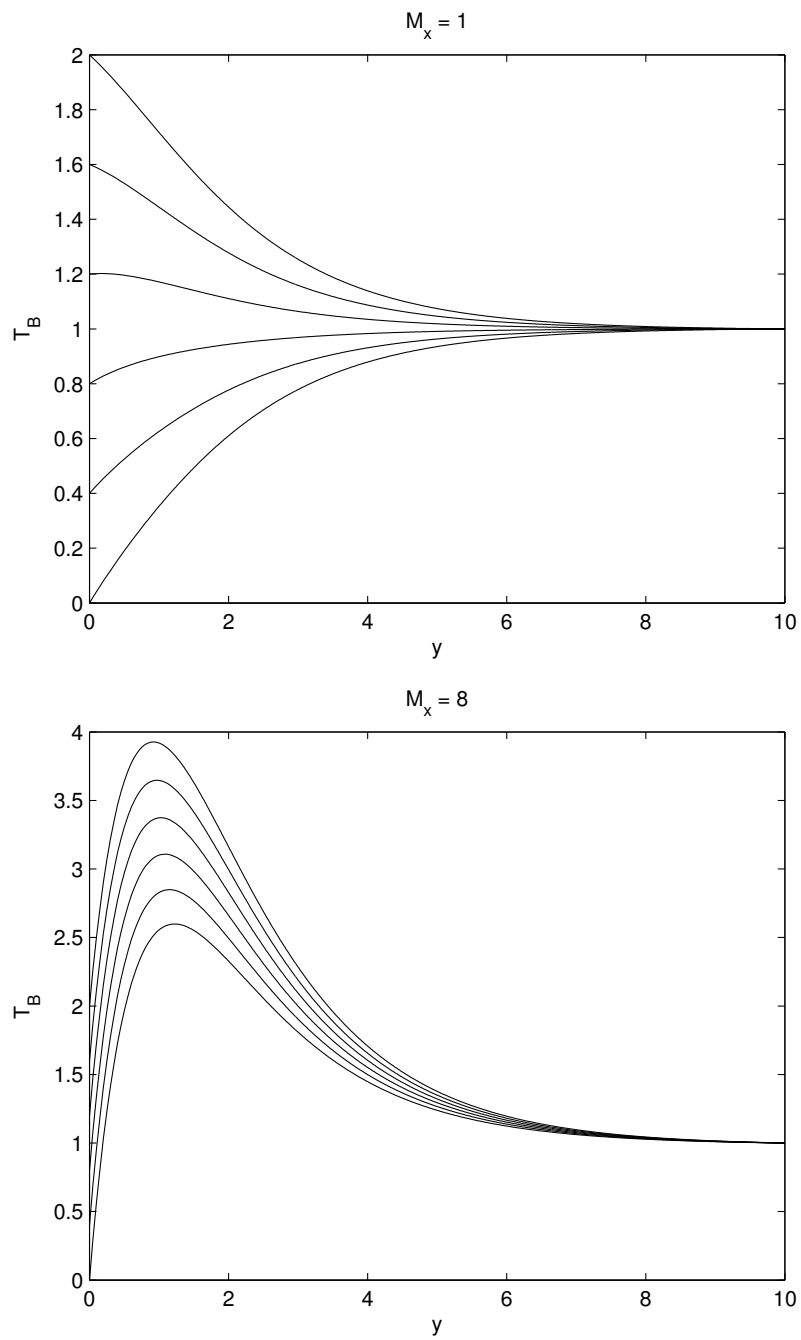


Figure 2.3: Varying wall temperature, increasing vertically from $T_w = 0 - 2$ in 0.4 increments, for constant local Mach numbers M_x .

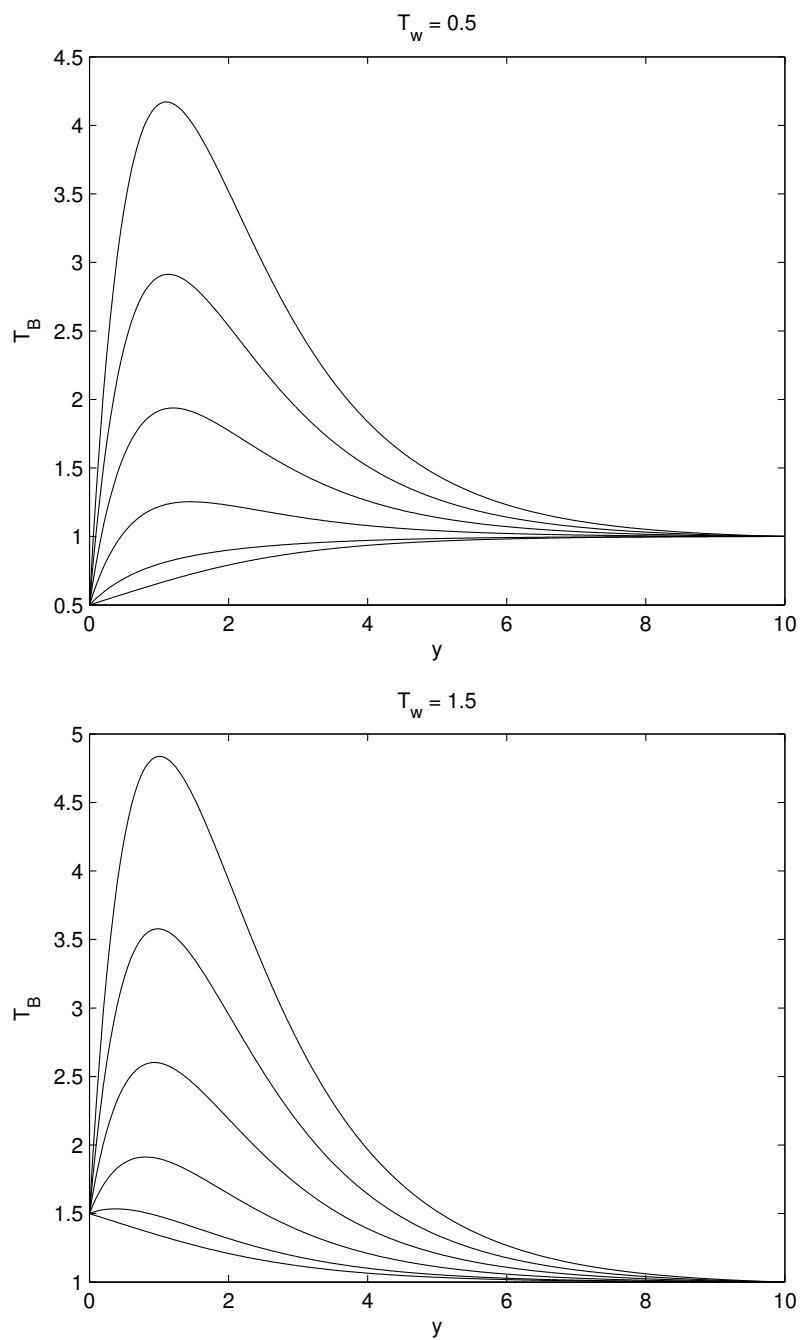


Figure 2.4: Varying local Mach number, increasing vertically from $M_x = 0-10$ in increments of 2, for constant wall temperatures T_w .

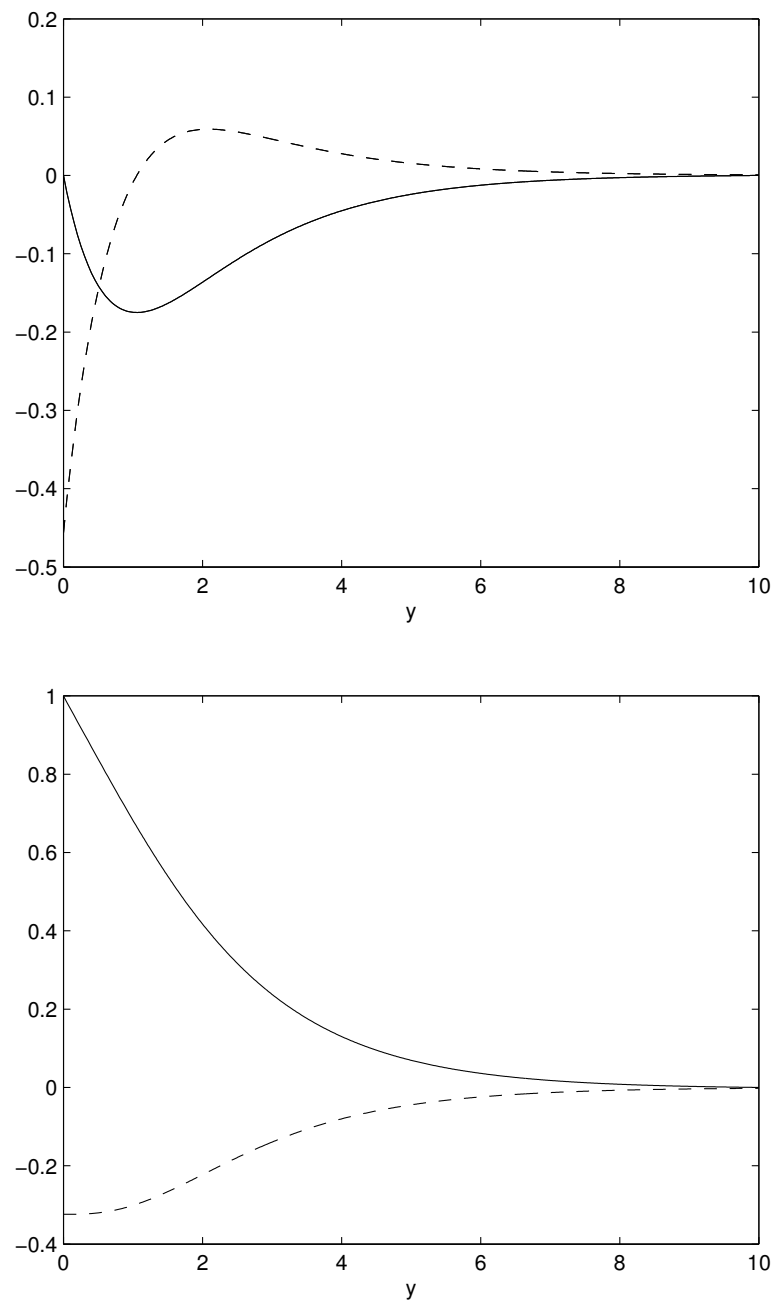


Figure 2.5: Numerical solution for (a) $f(-)$, $f'(-)$ and (b) $q(-)$, $q'(-)$.

2.3 Physical interpretation

To recover the dimensionless spatial quantity z from which we originally started, we invert the transformation (2.26) used to eliminate the density terms and make use of the temperature relation given by Equation (2.34).

By defining $R = \sin \psi R_{90}$, where R_{90} is the Reynolds number in the disk case and set to unity without loss of generality, we obtain

$$z = (\sin \psi)^{-1/2} \left(y - \frac{\gamma - 1}{2} M_x^2 \int_0^y f dy + (T_w - 1) \int_0^y q dy \right).$$

This reintroduces several physical parameters that were originally scaled out, namely wall temperature, cone half-angle and local Mach number, and facilitates a study of the physical effects of compressibility.

Figure 2.7 shows the effect of a change in local Mach number on the laminar flow profiles for $T_w = 1$. Similarly, Figure 2.8 shows the change brought by a change in the wall temperature for $M_x = 1$. It is shown that compressibility has a stretching effect on the flow profiles due to the quadratic local Mach number term, with the wall temperature controlling the magnitude of the heat conduction integral term. The maximum streamwise velocity component U is seen to be delayed by an increase in either the local Mach number or wall temperature, and the azimuthal component V also sees a delay in tending to 1 due to an increase in either value.

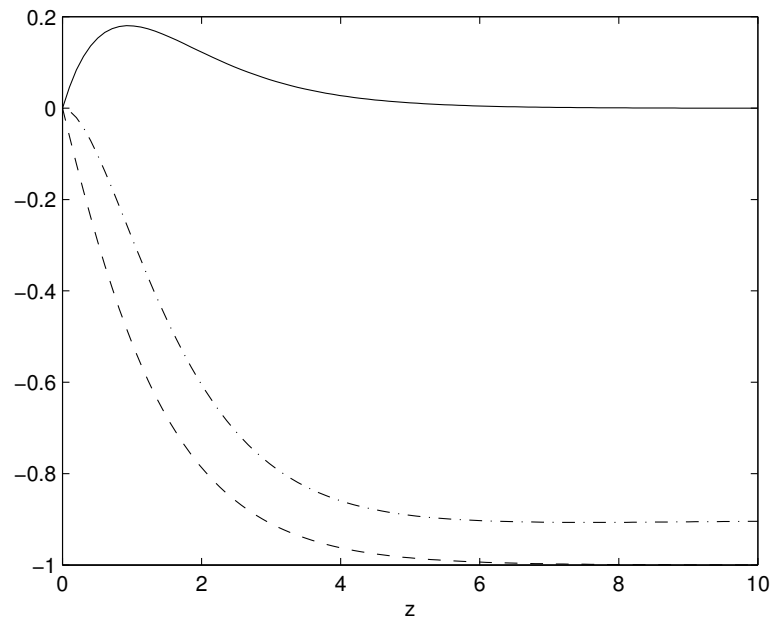


Figure 2.6: Solution of $U(-)$, $V(--)$ and $W(.-)$, for $\psi = 90^\circ$.

A low wall temperature produces similar results to the laminar flow profiles found in Figure 2.6, whereas for an increased wall temperature the W profile is seen to differ, which may suggest wall heating to have a destabilising effect on the flow. This is consistent with previous investigations Turkeyilmazoglu, Cole & Gajjar (2000) and will be considered further during the stability analysis.

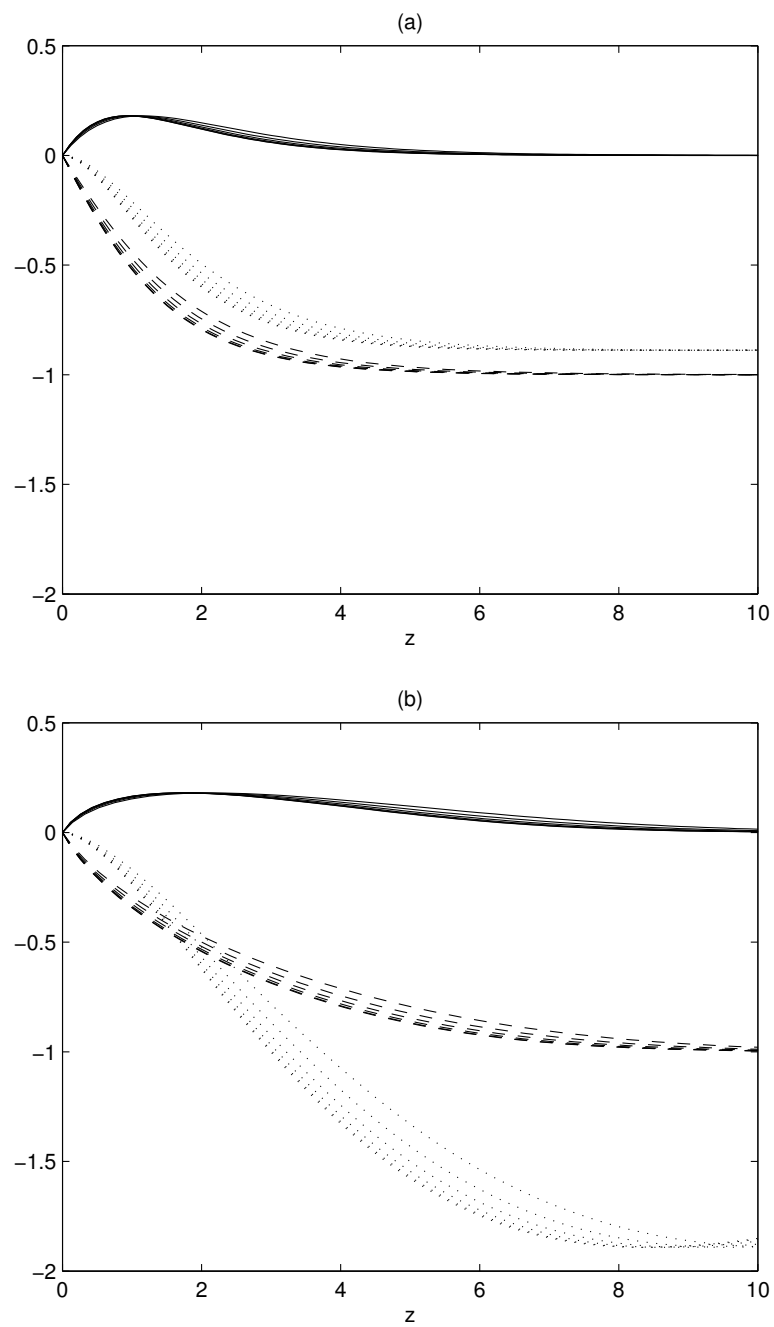


Figure 2.7: Physical laminar flow profiles $U(-)$, $V(--)$, $W(..)$ for $\psi = 40^\circ$ (uppermost) $- 90^\circ$, $T_w = 1$ with (a) $M_x = 0.5$ and (b) $M_x = 6$.

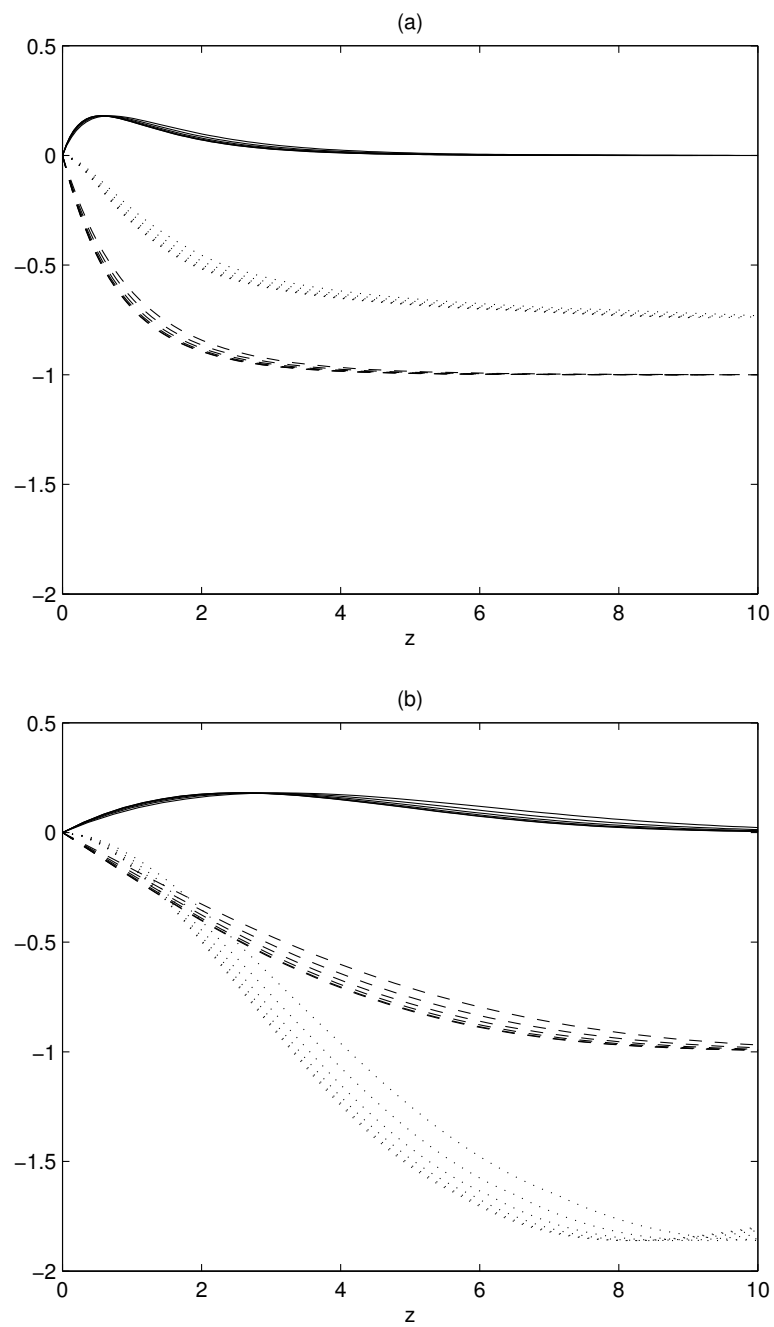


Figure 2.8: Physical laminar flow profiles $U(-)$, $V(--)$, $W(..)$ for $\psi = 40^\circ$ (uppermost) $- 90^\circ$, $M_x = 1$ with (a) $T_w = 0.5$ and (b) $T_w = 3$.

2.4 The effect of mass flux on the laminar flow solution

Introducing a mass flux through the cone surface causes a change in the boundary conditions (2.14). We introduce a suction parameter \bar{a} which replaces the zero boundary condition on the surface in the surface normal coordinate direction. This leads to the revised velocity boundary conditions of

$$\begin{aligned} u = 0, \quad v = 0, \quad w = \frac{\bar{a}}{\sin \psi}, \quad \text{on } \eta = 0, \\ u \rightarrow 0, \quad v \rightarrow -x \sin \psi \quad \text{as } \eta \rightarrow \infty. \end{aligned} \quad (2.39)$$

and modifies the von Kármán boundary conditions 2.33 as follows

$$\Psi(0) - \frac{a}{\sin \psi} = \Psi'(0) = \Psi(\infty) = V(0) = V(\infty) + 1 = T(\infty) - 1 = 0, \quad (2.40)$$

where a is the modified suction parameter $a = \frac{-\bar{a}}{2C^{1/2}T_w}$, and is defined for $-1 \leq a \leq 1$.

Figure 2.9 shows the plots for a uniform suction along the surface of the cone, for various value of half-angle ψ and suction parameter a , with fixed wall temperature $T_w = 0.5$ and C set to unity. The ψ -dependence arises through the normal velocity boundary condition (2.40), and is necessary to ensure a particular value of a represents the same physical surface mass flux across all ψ . Whilst the half angle is shown to have an effect on the wall normal component

W , the given physical velocity components U and V are relatively insensitive to this change. Suction is seen to narrow the boundary layer, as would be expected, and also reducing the magnitude of crossflow velocity. Both of these are expected to have a stabilising effect, as we shall study in later chapters.

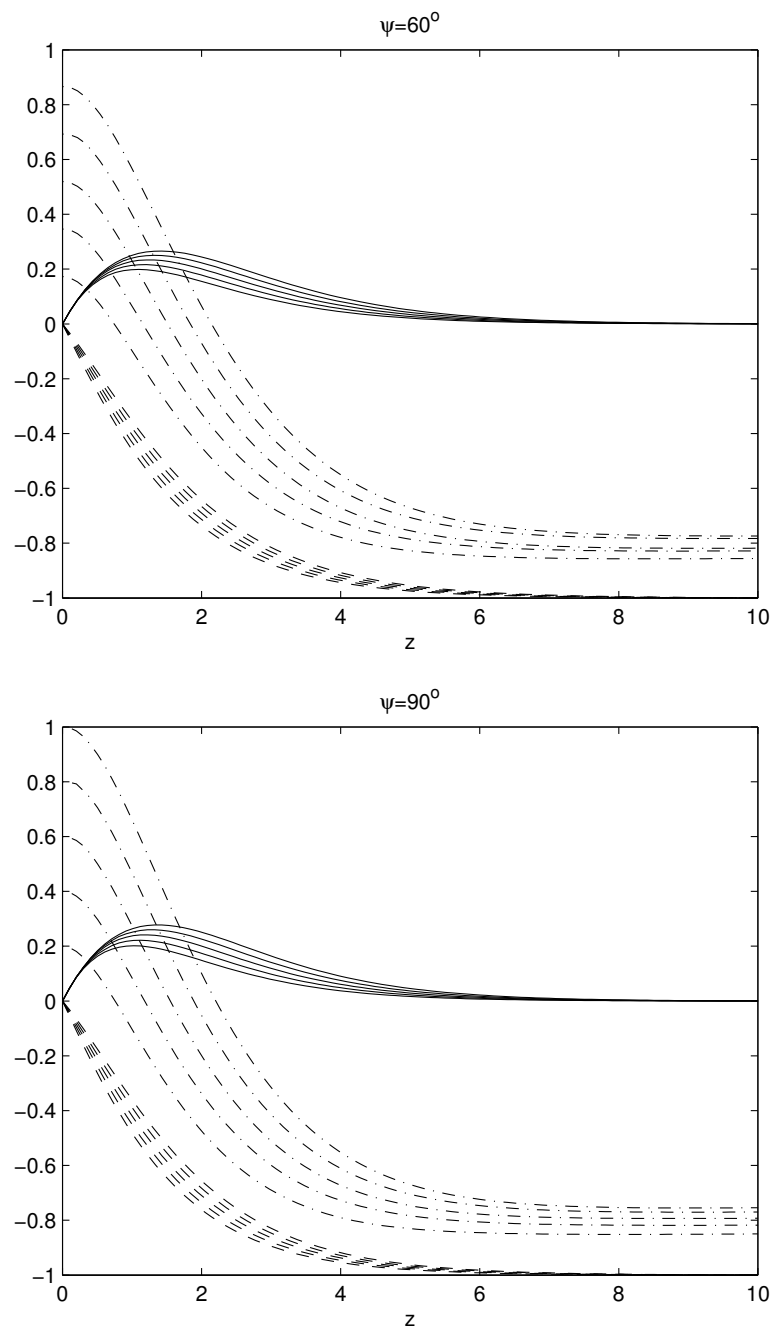


Figure 2.9: Varying suction parameter from $a = 0.2$ to $a = 1$ (uppermost) in increments of 0.2, for cone half angles ψ , where $U(-)$, $V(-)$ and $W(-)$.

Chapter 3

Inviscid type I modes

3.1 Linear perturbation equations

To begin the stability analysis we impose an infinitesimally small perturbation field on the governing equations (2.8)-(2.13). Hence the dimensional quantities become

$$\mathbf{u} \rightarrow \mathbf{u}^* + \hat{\mathbf{u}}, \quad (3.1)$$

$$p^* \rightarrow p^* + \hat{p}, \quad (3.2)$$

$$\rho^* \rightarrow \rho^* + \hat{\rho}, \quad (3.3)$$

$$T^* \rightarrow T^* + \hat{T}, \quad (3.4)$$

where $\hat{\mathbf{u}}, \hat{\rho}, \hat{T}$ are dimensional perturbation quantities. We non-dimensionalise using

$$\hat{\mathbf{u}} = l^* \Omega \sin \psi (\tilde{u}, \tilde{v}, \tilde{w}), \quad (3.5)$$

$$\hat{\rho} = \rho^* \Omega^{*2} l^{*2} \sin^2 \psi \tilde{p}, \quad (3.6)$$

$$\hat{\rho} = \rho_\infty \tilde{\rho}, \quad (3.7)$$

$$\hat{T} = T_\infty \tilde{T}, \quad (3.8)$$

where $\tilde{u}, \tilde{v}, \tilde{w}, \tilde{p}, \tilde{\rho}, \tilde{T}$ are the relevant non-dimensional perturbation quantities.

We expand (2.8)-(2.13) and linearise with respect to the perturbation terms, leading to the full linear perturbation equations

$$\begin{aligned} & \left(xu \frac{\partial}{\partial x} + \frac{xv}{h} \frac{\partial}{\partial \theta} + R^{-\frac{1}{2}} w \frac{\partial}{\partial z} + u + R^{-\frac{1}{2}} \frac{\partial w}{\partial z} + \frac{xu \sin \psi}{h} \right. \\ & \left. + \frac{R^{-\frac{1}{2}} w \cos \psi}{h} \right) \tilde{\rho} + \left(\frac{\partial \tilde{u}}{\partial x} + \frac{1}{h} \frac{\partial \tilde{v}}{\partial \theta} \right) \rho + \left(\frac{\partial \rho}{\partial x} + \frac{\rho \sin \psi}{h} \right) \tilde{u} \\ & \quad + \left(\frac{\partial \rho}{\partial z} + \rho \frac{\partial}{\partial z} + \frac{\rho \cos \psi}{h} \right) \tilde{w} = 0, \end{aligned} \quad (3.9)$$

$$\begin{aligned} & \rho \left\{ \left(xu \frac{\partial}{\partial x} + \frac{xv}{h} \frac{\partial}{\partial \theta} + R^{-\frac{1}{2}} w \frac{\partial}{\partial z} + u \right) \tilde{u} - 2 \left(\frac{v \sin \psi}{h} + 1 \right) \tilde{v} + x \tilde{w} \frac{\partial u}{\partial z} \right\} \\ & + \tilde{\rho} \left(xu^2 + R^{-\frac{1}{2}} xw \frac{\partial u}{\partial z} - \frac{x^2 v^2 \sin \psi}{h} - 2xv - \frac{h}{\sin \psi} \right) = - \frac{\partial \tilde{p}}{\partial x} \\ & + \frac{1}{R} \left\{ 2 \frac{\partial}{\partial x} \left(T \frac{\partial \tilde{u}}{\partial x} + \tilde{T} u \right) + \frac{1}{h} \frac{\partial}{\partial \theta} \left(T \left(\frac{\partial \tilde{v}}{\partial x} + \frac{1}{h} \frac{\partial \tilde{u}}{\partial \theta} - \frac{\tilde{v} \sin \psi}{h} \right) \right. \right. \\ & \quad \left. \left. + \tilde{T} \left(v - \frac{xv \sin \psi}{h} \right) \right) + \frac{\partial}{\partial z} \left(T \left(\frac{\partial \tilde{w}}{\partial x} + \frac{\partial \tilde{u}}{\partial z} \right) + \tilde{T} x \frac{\partial u}{\partial z} \right) \right\}, \end{aligned} \quad (3.10)$$

$$\begin{aligned}
 & \rho \left\{ \left(xu \frac{\partial}{\partial x} + \frac{xv}{h} \frac{\partial}{\partial \theta} + R^{-\frac{1}{2}} w \frac{\partial}{\partial z} + \frac{xu \sin \psi}{h} + \frac{R^{-\frac{1}{2}} w \cos \psi}{h} \right) \tilde{v} \right. \\
 & \quad \left. + \left(\tilde{w} x \frac{\partial}{\partial z} + \frac{\tilde{u} x \sin \psi}{h} + \frac{\tilde{w} x \cos \psi}{h} + \tilde{u} \right) v + 2(\tilde{u} + \tilde{w} \cot \psi) \right\} \\
 & \quad + \tilde{\rho} \left\{ \left(R^{-\frac{1}{2}} x w \frac{\partial}{\partial z} + x u + \frac{x^2 u \sin \psi}{h} + \frac{R^{-\frac{1}{2}} w \cos \psi}{h} \right) v \right. \\
 & \quad \left. + 2(xu + R^{-\frac{1}{2}} w \cot \psi) \right\} = \frac{-1}{h} \frac{\partial \tilde{p}}{\partial \theta} + \frac{1}{R} \left\{ \frac{\partial}{\partial x} \left(T \left(\frac{\partial \tilde{v}}{\partial x} + \frac{1}{h} \frac{\partial \tilde{u}}{\partial \theta} - \frac{\tilde{v} \sin \psi}{h} \right) \right. \right. \\
 & \quad \left. \left. + \tilde{T} \left(v - \frac{xv \sin \psi}{h} \right) \right) + \frac{2}{h^2} \frac{\partial}{\partial \theta} \left(T \left(\frac{\partial \tilde{v}}{\partial \theta} + \tilde{u} \sin \psi + \tilde{w} \cos \psi \right) \right. \right. \\
 & \quad \left. \left. + \tilde{T} \left(xu \sin \psi + R^{-\frac{1}{2}} w \cos \psi \right) \right) + \frac{\partial}{\partial z} \left(T \left(\frac{\partial \tilde{v}}{\partial z} + \frac{1}{h} \frac{\partial \tilde{w}}{\partial \theta} - \frac{\tilde{v} \cos \psi}{h} \right) \right. \right. \\
 & \quad \left. \left. + \tilde{T} \left(x \frac{\partial v}{\partial z} - \frac{xv \cos \psi}{h} \right) \right) \right\},
 \end{aligned} \tag{3.11}$$

$$\begin{aligned}
 & \rho \left\{ \left(xu \frac{\partial}{\partial x} + \frac{xv}{h} \frac{\partial}{\partial \theta} + R^{-\frac{1}{2}} w \frac{\partial}{\partial z} + R^{-\frac{1}{2}} \frac{\partial w}{\partial z} \right) \tilde{w} \right. \\
 & \quad \left. - 2 \left(\frac{xv \cos \psi}{h} + \cot \psi \right) \tilde{v} \right\} + \tilde{\rho} \left(R^{-1} w \frac{\partial w}{\partial z} - \frac{x^2 v^2 \cos \psi}{h} - 2xv \cot \psi \right. \\
 & \quad \left. - \frac{h \cot \psi}{\sin \psi} \right) = -\frac{\partial \tilde{p}}{\partial z} + \frac{1}{R} \left\{ \frac{\partial}{\partial x} \left(T \left(\frac{\partial \tilde{w}}{\partial x} + \frac{\partial \tilde{u}}{\partial z} \right) + \tilde{T} x \frac{\partial u}{\partial z} \right) \right. \\
 & \quad \left. + \frac{1}{h} \frac{\partial}{\partial \theta} \left(T \left(\frac{\partial \tilde{v}}{\partial z} + \frac{1}{h} \frac{\partial \tilde{w}}{\partial \theta} - \frac{\tilde{v} \cos \psi}{h} \right) + \tilde{T} \left(x \frac{\partial v}{\partial z} - \frac{xv \cos \psi}{h} \right) \right) \right. \\
 & \quad \left. + 2 \frac{\partial}{\partial z} \left(T \frac{\partial \tilde{w}}{\partial z} + R^{-\frac{1}{2}} \tilde{T} \frac{\partial w}{\partial z} \right) \right\},
 \end{aligned} \tag{3.12}$$

$$\gamma M_\infty^2 \tilde{p} = \tilde{\rho} T + \rho \tilde{T}, \tag{3.13}$$

$$\begin{aligned}
& \frac{\rho}{M_\infty^2(\gamma-1)} \left(ux \frac{\partial \tilde{T}}{\partial x} + \tilde{u} \frac{\partial T}{\partial x} + \frac{xv}{h} \frac{\partial \tilde{T}}{\partial \theta} + R^{-\frac{1}{2}} w \frac{\partial \tilde{T}}{\partial z} + \tilde{w} \frac{\partial T}{\partial z} \right) \quad (3.14) \\
& + \frac{\tilde{\rho}}{M_\infty^2(\gamma-1)} \left(xu \frac{\partial T}{\partial x} + R^{-\frac{1}{2}} w \frac{\partial T}{\partial z} \right) = xu \frac{\partial \tilde{p}}{\partial x} + \tilde{u} \frac{\partial p}{\partial x} + \frac{xv}{h} \frac{\partial \tilde{p}}{\partial \theta} \\
& \quad + R^{-\frac{1}{2}} w \frac{\partial \tilde{p}}{\partial z} + \tilde{w} \frac{\partial p}{\partial z} + \frac{1}{h\sigma R M_\infty^2(\gamma-1)} \left\{ \frac{\partial}{\partial x} \left(h \frac{\partial \tilde{T}}{\partial x} \right) + \frac{\partial^2 \tilde{T}}{\partial \theta^2} \right. \\
& \quad \left. + \frac{\partial}{\partial z} \left(h \frac{\partial \tilde{T}}{\partial z} \right) \right\} + \frac{\mu}{R} \left\{ 2u \frac{\partial \tilde{u}}{\partial x} + \frac{2}{h^2} \left((xu \sin \psi + R^{-\frac{1}{2}} w \cos \psi) \frac{\partial \tilde{v}}{\partial \theta} \right. \right. \\
& \quad \left. \left. + (xu \sin \psi + R^{-\frac{1}{2}} w \cos \psi) \tilde{u} \sin \psi + (xu \sin \psi + R^{-\frac{1}{2}} w \cos \psi) \tilde{w} \cos \psi \right) \right. \\
& \quad \left. + 2w \frac{\partial \tilde{w}}{\partial z} + 2R^{-\frac{1}{2}} \frac{\partial w}{\partial z} \frac{\partial \tilde{w}}{\partial z} + \left(v - \frac{xv \sin \psi}{h} \right) \frac{\partial \tilde{v}}{\partial x} + \left(\frac{v}{h} - \frac{xv \sin \psi}{h^2} \right) \frac{\partial \tilde{u}}{\partial \theta} \right. \\
& \quad \left. + \left(\frac{xv \sin^2 \psi}{h} - \frac{v \sin \psi}{h} \right) \tilde{v} + x \frac{\partial u}{\partial z} \frac{\partial \tilde{u}}{\partial z} + x \frac{\partial u}{\partial z} \frac{\partial \tilde{w}}{\partial x} + \left(v + x \frac{\partial v}{\partial z} \right. \right. \\
& \quad \left. \left. - \frac{xv \cos \psi}{h} \right) \frac{\partial \tilde{v}}{\partial z} + \left(\frac{v}{h} + \frac{x}{h} \frac{\partial v}{\partial z} - \frac{xv \cos \psi}{h^2} \right) \frac{\partial \tilde{w}}{\partial \theta} + \left(\frac{xv \cos^2 \psi}{h} \right. \right. \\
& \quad \left. \left. - \frac{x \cos \psi}{h} \frac{\partial v}{\partial z} - \frac{v \cos \psi}{h} \right) \tilde{v} \right\} + \frac{\lambda}{Rh} \left\{ xu \tilde{u} \sin^2 \psi + 2hu \tilde{u} \sin \psi \right. \\
& \quad \left. + xu \sin \psi \frac{\partial \tilde{u}}{\partial x} + xu \sin \psi \frac{\partial \tilde{v}}{\partial \theta} + xu \tilde{w} \sin \psi \cos \psi + R^{-\frac{1}{2}} w \tilde{u} \sin \psi \cos \psi \right. \\
& \quad \left. + R^{-\frac{1}{2}} h \tilde{u} \sin \psi \frac{\partial w}{\partial z} + xuh \sin \psi \frac{\partial \tilde{w}}{\partial z} + hu \frac{\partial \tilde{u}}{\partial x} + hu \frac{\partial \tilde{v}}{\partial \theta} + uh \tilde{w} \cos \psi \right. \\
& \quad \left. + uh^2 \frac{\partial \tilde{w}}{\partial z} + R^{-\frac{1}{2}} w \cos \psi \frac{\partial \tilde{u}}{\partial x} + R^{-\frac{1}{2}} h \frac{\partial w}{\partial z} \frac{\partial \tilde{u}}{\partial x} + R^{-\frac{1}{2}} w \cos \psi \frac{\partial \tilde{v}}{\partial \theta} \right. \\
& \quad \left. + R^{-\frac{1}{2}} h \frac{\partial w}{\partial z} \frac{\partial \tilde{v}}{\partial \theta} + R^{-\frac{1}{2}} w \tilde{w} \cos^2 \psi + R^{-\frac{1}{2}} h \tilde{w} \cos \psi \frac{\partial w}{\partial z} \right. \\
& \quad \left. + R^{-\frac{1}{2}} wh \cos \psi \frac{\partial \tilde{w}}{\partial z} + R^{-\frac{1}{2}} h^2 \frac{\partial w}{\partial z} \frac{\partial \tilde{w}}{\partial z} \right\}.
\end{aligned}$$

Note that as well as forming the basis of the following section, these perturbation equations will also be used in the viscous analysis in Chapter 4.

3.2 Type I perturbation functions

To begin the inviscid type I mode analysis we consider the previous incompressible analysis by Hall (1986) for the rotating disk and Hussain (2009) for the rotating cone, along with the compressible rotating disk flow analysis by Turkyilmazoglu, Cole & Gajjar (2000). We seek a normal-mode solution and scale the inviscid mode wavelengths, α and β in the x and θ directions respectively, by the boundary layer-thickness which is $O(R^{-\frac{1}{2}})$.

We choose to define a small parameter $\epsilon = R^{-\frac{1}{6}}$ following the aforementioned previous work, which is entirely appropriate as for an arbitrary Reynolds number domain $R \in (10^4, 10^7)$, $\epsilon \in (0.068, 0.215)$ and $\epsilon \rightarrow 0$ as $R \rightarrow \infty$. We let the perturbation velocity functions depend on the wall normal coordinate z only. Then the perturbations are given by

$$\tilde{u} = u(z) \exp\left(\frac{i}{\epsilon^3} \left\{ \int^x \alpha(x, \epsilon) dx + \beta(\epsilon)\theta \right\}\right), \quad (3.15)$$

with similar expressions for all other perturbations $\tilde{v}, \tilde{w}, \tilde{p}, \tilde{\rho}, \tilde{T}$. The stream-wise and azimuthal wavenumbers are expanded as

$$\alpha = \alpha_0 + \epsilon\alpha_1 + \dots, \quad (3.16)$$

$$\beta = \beta_0 + \epsilon\beta_1 + \dots \quad (3.17)$$

Following Hall (1986) we restrict ourselves to neutral disturbances and find α and β such that the flow is neutrally stable at position x , hence $\alpha, \beta \in \mathbb{R}$. Then

from the experimental study by Gregory, Stuart & Walker (1955), Hall (1986) states that there is an inviscid layer of thickness $O(\epsilon^3)$. However to satisfy the no slip condition on the cone's wall, there must exist a viscous layer. By balancing convection and diffusion terms in the perturbation equations the viscous layer is found to be $O(\epsilon^4)$, and will be considered in §3.4.

In the inviscid layer we expand the perturbation functions as

$$u = u_0(\eta) + \epsilon u_1(\eta) + \dots, \quad (3.18)$$

$$v = v_0(\eta) + \epsilon v_1(\eta) + \dots, \quad (3.19)$$

$$w = w_0(\eta) + \epsilon w_1(\eta) + \dots, \quad (3.20)$$

$$p = p_0(\eta) + \epsilon p_1(\eta) + \dots, \quad (3.21)$$

$$\rho = \rho_0(\eta) + \epsilon \rho_1(\eta) + \dots, \quad (3.22)$$

$$T = T_0(\eta) + \epsilon T_1(\eta) + \dots, \quad (3.23)$$

where $\eta = z\epsilon^{-3}$. Here $\frac{\partial}{\partial x}$, $\frac{\partial}{\partial \theta}$ and $\frac{\partial}{\partial z}$ are effectively transformed to

$$\frac{\partial}{\partial x} \mapsto \frac{\partial}{\partial x} + \frac{i}{\epsilon^3} \{\alpha_0 + \epsilon \alpha_1 + \dots\}, \quad (3.24)$$

$$\frac{\partial}{\partial \theta} \mapsto \frac{i}{\epsilon^3} \{\beta_0 + \epsilon \beta_1 + \dots\}, \quad (3.25)$$

$$\frac{\partial}{\partial z} \mapsto \frac{1}{\epsilon^3} \frac{\partial}{\partial \eta}. \quad (3.26)$$

3.3 Leading order eigenmodes

Substituting the expansions (3.15)–(3.23) into the perturbation equations (3.9)–(3.14) and equating terms of $O(\epsilon^{-3})$ leads to the leading-order eigenmodes given by

$$i\rho_0\bar{\bar{U}} + i\rho\left(u_0\alpha_0 + \frac{v_0\beta_0}{x\sin\psi}\right) + w_0\frac{\partial\rho}{\partial\eta} + \rho w'_0 = 0, \quad (3.27)$$

$$i\rho u_0\bar{\bar{U}} + \rho x w_0 u' = -i\alpha_0 p_0, \quad (3.28)$$

$$i\rho v_0\bar{\bar{U}} + \rho x w_0 v' = -\frac{i\beta_0 p_0}{x\sin\psi}, \quad (3.29)$$

$$i\rho w_0\bar{\bar{U}} = -p'_0, \quad (3.30)$$

$$\frac{\rho}{M_\infty^2(\gamma - 1)}\left(iT_0\bar{\bar{U}} + w_0\frac{\partial T}{\partial\eta}\right) = ip_0\bar{\bar{U}} + w_0\frac{\partial p}{\partial\eta}, \quad (3.31)$$

where $\bar{\bar{U}} = \alpha_0 x u + \frac{\beta_0 v}{\sin\psi}$.

The quantities u_0, v_0, p_0 and T_0 can be eliminated from the above equations and we find an equation in w_0 given by

$$\rho\bar{\bar{U}}w_0'' + (2\rho'\bar{\bar{U}} - \rho\bar{\bar{U}}')w_0' + (\rho''\bar{\bar{U}} - \rho\bar{\bar{U}}'' - \rho\bar{\bar{U}}\gamma_0^2)w_0 = 0 \quad (3.32)$$

The quantity $\gamma_0^2 = \alpha_0^2 + \frac{\beta_0^2}{x^2\sin^2\psi}$ is interpreted as the effective wave number and $\bar{\bar{U}}$ as the effective velocity profile, as previously discussed by Hall (1986) for the rotating disk case. Then Equation (3.32) is the compressible Rayleigh equation which dictates the leading-order stability of the flow.

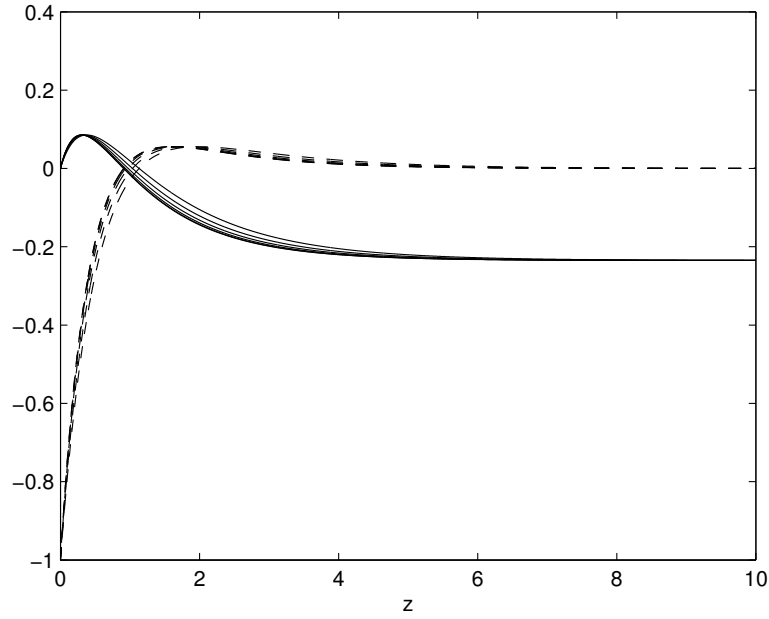


Figure 3.1: The effective velocity $\bar{U}(-)$ and its second derivative $\bar{U}''(-)$ for $\psi = 40^\circ$ (uppermost at $z = 10$)– 90° , where $T_w = M_x = \frac{1}{2}$.

We proceed by solving the eigenvalue problem (3.32) subject to the boundary conditions at the cone wall and in the free-stream given by

$$w_0 = 0 \text{ at } z = 0, \infty, \quad (3.33)$$

where there exists a singularity at that point due to the effective velocity having a root in the domain. We use a numerical method of central finite differences with $z = \bar{z}$ such that $\bar{U} = \bar{U}'' = 0$ at this point, known as the location of the critical layer. This condition requires the effective velocity profile \bar{U} to

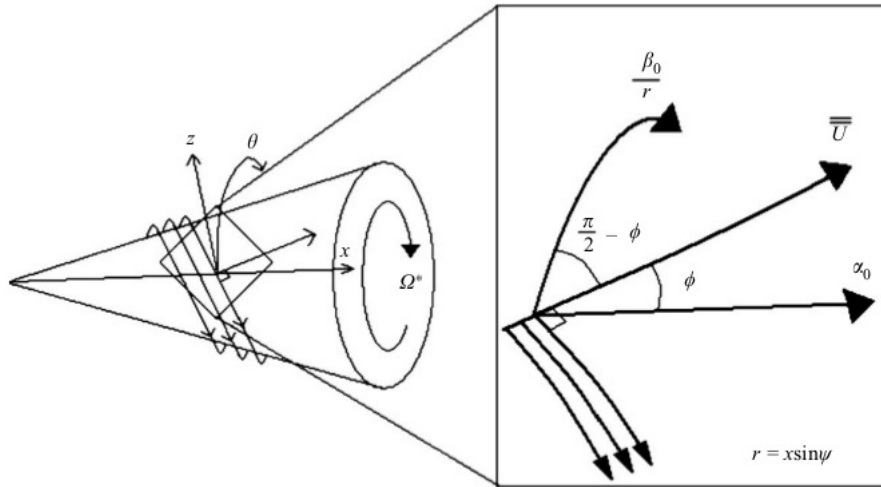


Figure 3.2: Diagram showing the direction of wave numbers and the effective velocity, taken from Garrett, Hussain & Stephen (2009).

have a root and inflexion point at $z = \bar{z}$. To interpret the results physically we consider the spiral vortices that wrap around the cone at an angle to the cone meridian. As shown in Figure 3.2 the normal to these spiral vortices is in the direction of the effective velocity and is at an angle ϕ to the streamwise position vector, which defines our waveangle ϕ . The wavenumbers for neutrally stable modes are given by γ_0 .

Figures 3.3-3.5 show the profile of w_0 for given values of T_w and M_x , with varying ψ . The profile shape is consistent with that of the incompressible case (Hussain (2009)), with a larger value for the velocity peak. This is physically plausible because a non-constant density would suggest that any disturbance

would grow to be greater than in an incompressible fluid before being suppressed. In Figure 3.6 the effect of an active suction parameter is shown. Including a non-zero value for a is seen to have a relatively large effect on the w_0 profile, however an increase in a is then seen to cause little change.

As the suction is turned on the leading-order wall normal perturbation quantity w_0 quickly reduces in magnitude, almost immediately eliminating the effect of the perturbation. This suggests that suction along the cone wall can be used as a stabilising mechanism, which is consistent with previous findings by Gregory & Walker (1960), Lingwood (1997).

Figure 3.7 presents the leading-order wavenumber and waveangle predictions for the inviscid neutrally stable modes, under several different parameter combinations. The wavenumbers are consistent with the incompressible case in that as the half angle grows the wavenumber grows. For the waveangles, as the half angle increases the spiral vortices deviate further from the stream-wise direction, which is in agreement with the incompressible case (Garrett, Hussain & Stephen (2009)), due to an increased rotational shear force on the vortex spirals as the gradient of the cone's surface grows as ψ increases.

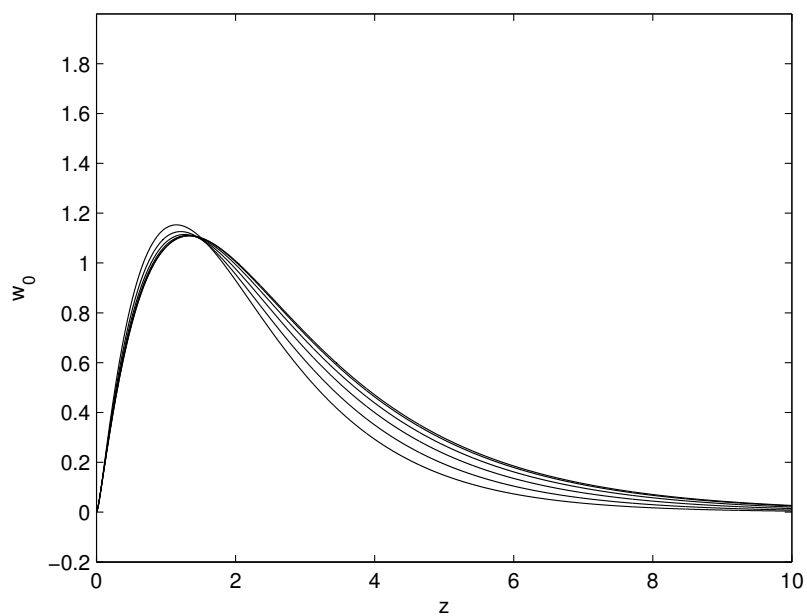


Figure 3.3: w_0 for $\psi = 40^\circ$ (uppermost) – 90° where $T_w = \frac{1}{2}, M_x = \frac{1}{2}$

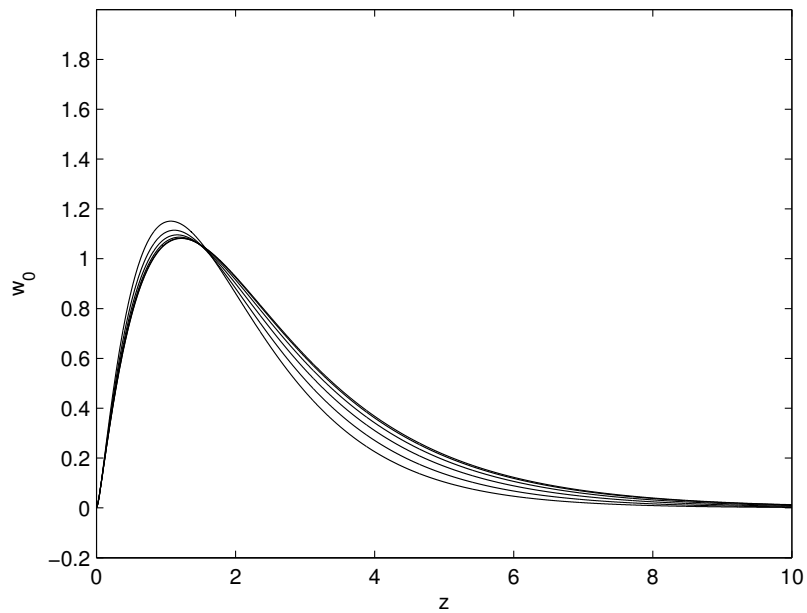


Figure 3.4: w_0 for $\psi = 40^\circ$ (uppermost) – 90° where $T_w = \frac{1}{2}, M_x = 1$

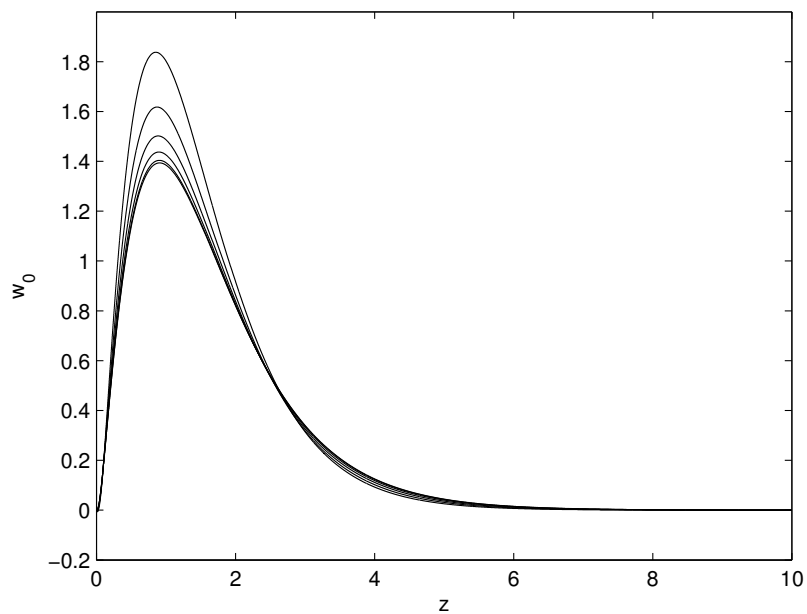


Figure 3.5: w_0 for $\psi = 40^\circ$ (uppermost) – 90° where $T_w = 1, M_x = 1$

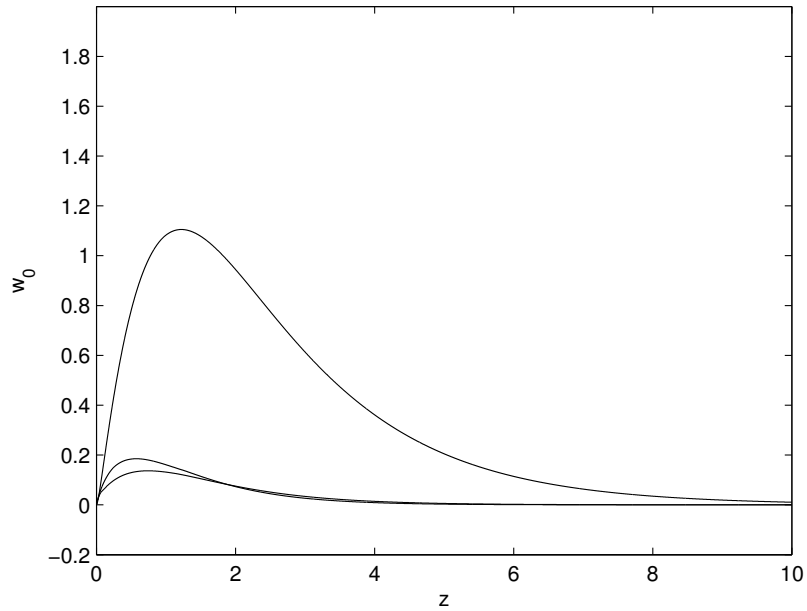


Figure 3.6: w_0 for $\psi = 60^\circ, T_w = \frac{1}{2}, M_x = 1$ with suction parameter $a = 0$ (uppermost), $0.1, 0.2$.

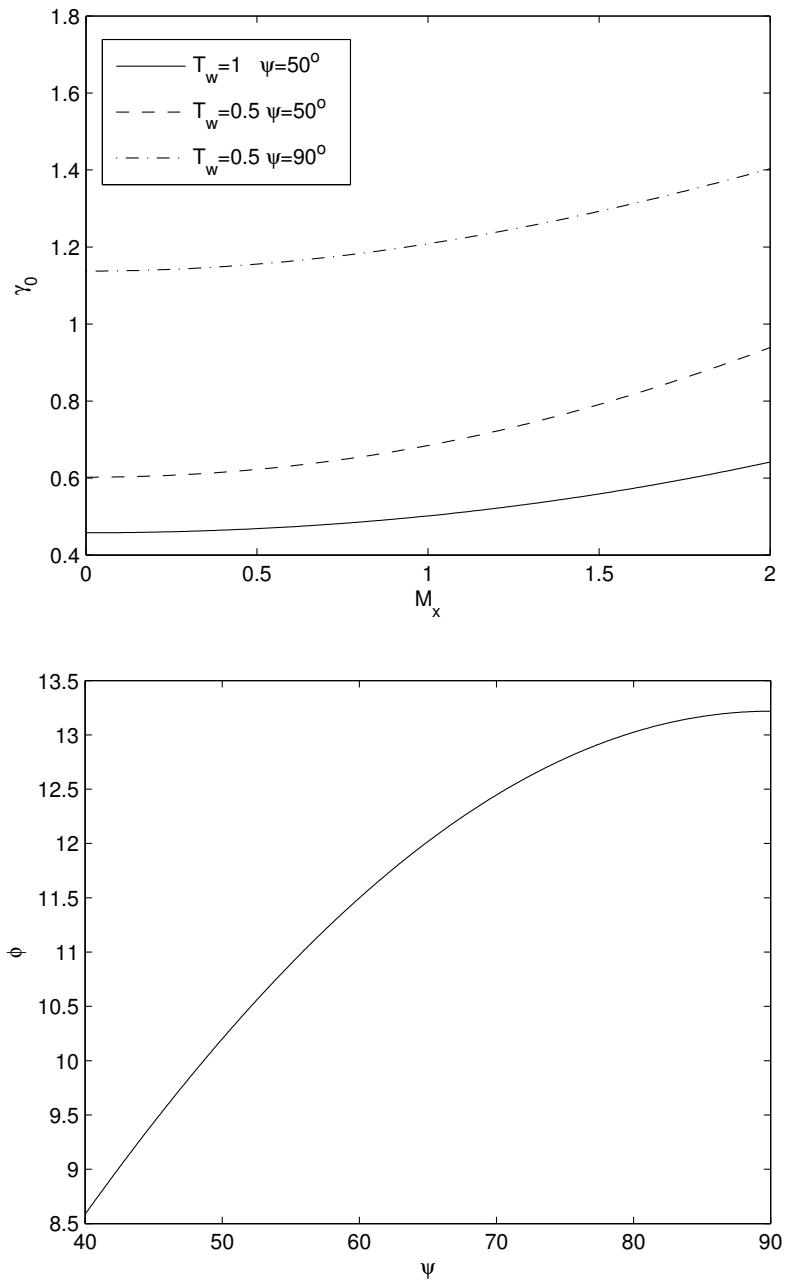


Figure 3.7: Asymptotic plots of leading order wavenumber & waveangle predictions for neutrally stable inviscid modes

3.4 Wall layer solution

We now consider the leading-order inviscid mode solution for the wall layer, which is present to preserve the no slip boundary condition on the cone's surface. The surface-normal coordinate now takes the form $\xi = \epsilon^{-4}z$, where ξ is related to the original surface-normal coordinate by $\eta = \epsilon\xi$. On the cone wall, the basic flow quantities satisfy the no-slip condition, with derivatives linear in ξ such that

$$u = \epsilon u'(0)\xi, \quad (3.34)$$

$$v = \epsilon v'(0)\xi, \quad (3.35)$$

$$w = \epsilon w'(0)\xi. \quad (3.36)$$

We expand the perturbation quantities within the wall layer as

$$\bar{u} = U_0(\xi) + \epsilon U_1(\xi) + \dots, \quad (3.37)$$

$$\bar{v} = V_0(\xi) + \epsilon V_1(\xi) + \dots, \quad (3.38)$$

$$\bar{w} = \epsilon W_0(\xi) + \epsilon^2 W_1(\xi) + \dots, \quad (3.39)$$

$$\bar{p} = \epsilon P_0(\xi) + \epsilon^2 P_1(\xi) + \dots, \quad (3.40)$$

$$\bar{\rho} = \rho_0(\xi) + \epsilon \rho_1(\xi) + \dots, \quad (3.41)$$

$$\bar{T} = T_0(\xi) + \epsilon T_1(\xi) + \dots \quad (3.42)$$

We substitute these expansions into the perturbation equations (3.9)-(3.14) and equate terms of $O(\epsilon^{-3})$ for the continuity equation, terms of $O(\epsilon^{-2})$ for the streamwise velocity, azimuthal velocity and energy equations, and $O(\epsilon^{-1})$ for the surface-normal velocity equation. This leads to

$$\rho \left(i\alpha_0 U_0 + \frac{i\beta_0 V_0}{x \sin \psi} + W_0' \right) + W_0 \frac{\partial \rho}{\partial \xi} = 0, \quad (3.43)$$

$$\begin{aligned} \rho \left(i x u'(0) \xi \alpha_0 U_0 + \frac{i v'(0) \xi \beta_0 U_0}{\sin \psi} + x u'(0) W_0 \right) \\ = -i\alpha_0 P_0 + U_0' \frac{\partial T}{\partial \xi} + T U_0'', \end{aligned} \quad (3.44)$$

$$\begin{aligned} \rho \left(i x u'(0) \xi \alpha_0 V_0 + \frac{i v'(0) \xi \beta_0 V_0}{\sin \psi} + x v'(0) W_0 \right) \\ = -\frac{i P_0 \beta_0}{x \sin \psi} + V_0' \frac{\partial T}{\partial \xi} + T V_0'', \end{aligned} \quad (3.45)$$

$$\rho \left(i x u'(0) \xi \alpha_0 W_0 + \frac{i x v'(0) \xi \beta_0 W_0}{x \sin \psi} \right) = -P_2' + 2W_0' \frac{\partial T}{\partial \xi} + 2T W_0'', \quad (3.46)$$

$$\frac{\rho}{M_\infty^2 (\gamma - 1)} \left(i u'(0) \xi x \alpha_0 T_0 + \frac{i v'(0) \xi \beta_0 T_0}{\sin \psi} + W_1 \frac{\partial T}{\partial \xi} \right) = W_1 \frac{\partial p}{\partial \xi} + \quad (3.47)$$

$$\frac{1}{x \sin \psi \sigma M_\infty^2 (\gamma - 1)} \left(\cos \psi T_2' + x \sin \psi T_0'' \right) + x \mu \left(\frac{\partial u}{\partial \xi} U_0' + \frac{\partial v}{\partial \xi} V_0' \right).$$

Considering $\frac{d}{d\xi}(\alpha_0 \times (3.45)) + \frac{d}{d\xi}(\frac{\beta_0}{x \sin \psi} \times (3.46))$, and eliminating W_0 by using (3.43), we obtain

$$\begin{aligned} \left(T \left(\alpha_0 U_0 + \frac{\beta_0 V_0}{x \sin \psi} \right)' \right)'' \\ - i \xi \left(\alpha_0 x u'(0) + \frac{\beta_0 v'(0)}{\sin \psi} \right) \left(\frac{1}{T} \left(\alpha_0 U_0 + \frac{\beta_0 V_0}{x \sin \psi} \right) \right)' = 0. \end{aligned} \quad (3.48)$$

We will now move onto the next-order problem in the inviscid zone and will discuss the application of this equation in relation to the next-order equations.

3.5 First order eigenmodes

We next consider the first-order relations in the inviscid zone. We follow the method of §3.3 and expand the perturbation equations (3.9)-(3.14) to $O(\epsilon^{-2})$ to find

$$\begin{aligned} i x u (\rho_0 \alpha_1 + \rho_1 \alpha_0) + \frac{i v}{\sin \psi} (\rho_0 \beta_1 + \rho_1 \beta_0) + i \rho (u_0 \alpha_1 + u_1 \alpha_0) \\ + \frac{i \rho}{x \sin \psi} (v_0 \beta_1 + v_1 \beta_0) + w_1 \rho' + \rho w_1' = 0, \end{aligned} \quad (3.49)$$

$$\begin{aligned} i \rho x u (\alpha_1 u_0 + \alpha_0 u_1) + \frac{i \rho v}{\sin \psi} (\beta_1 u_0 + \beta_0 u_1) + \rho x w_1 u' \\ = -i (\alpha_0 p_1 + \alpha_1 p_0), \end{aligned} \quad (3.50)$$

$$\begin{aligned} i \rho x u (\alpha_1 v_0 + \alpha_0 v_1) + \frac{i \rho v}{\sin \psi} (\beta_1 v_0 + \beta_0 v_1) + \rho w_1 x v' \\ = \frac{-i}{x \sin \psi} (\beta_0 p_1 + \beta_1 p_0), \end{aligned} \quad (3.51)$$

$$i \rho x u (\alpha_1 w_0 + \alpha_0 w_1) + \frac{i \rho v}{\sin \psi} (\beta_1 w_0 + \beta_0 w_1) = -p_1', \quad (3.52)$$

$$\begin{aligned} \frac{\rho}{M_\infty^2 (\Gamma - 1)} \left(i u x (\alpha_1 T_0 + \alpha_0 T_1) + \frac{i v}{\sin \psi} (\beta_0 T_1 + \beta_1 T_0) + w_1 \frac{\partial T}{\partial \eta} \right) \\ = i x u (\alpha_1 p_0 + \alpha_0 p_1) + \frac{i v}{\sin \psi} (\beta_0 p_1 + \beta_1 p_0) + w_1 \frac{\partial p}{\partial \eta}. \end{aligned} \quad (3.53)$$

These are the equivalent equations to (3.27)-(3.31) for the disturbance quan-

tities $(u_1, v_1, w_1, p_1, \rho_1, T_1)$, where we find the introduction of inhomogenous cross-terms related to the leading-order quantities $(u_0, v_0, w_0, p_0, \rho_0, T_0)$. The quantities u_1, v_1, p_1 and T_1 are eliminated as in the leading order case. We use the leading-order continuity equation (3.27) to eliminate u_0 , and the leading-order azimuthal velocity equation (3.29) to eliminate v_0 . This leads to the governing equation for the first-order eigenfunction given by

$$\begin{aligned}
 & \rho \bar{\bar{U}} w_1'' + (2\rho' \bar{\bar{U}} - \rho \bar{\bar{U}}') w_1' + (\rho'' \bar{\bar{U}} - \rho \bar{\bar{U}}'' - \rho \bar{\bar{U}} \gamma_0^2) w_1 \\
 & = \left(\beta_1 - \frac{\alpha_1 \beta_0}{\alpha_0} \right) \frac{\rho v'}{\sin \psi} w_0' + \left(\rho \left(\alpha_1 x u + \frac{\beta_1 v}{\sin \psi} \right) \gamma_0^2 \right. \\
 & \quad \left. + \rho \bar{\bar{U}} \left(\alpha_0 \alpha_1 + \frac{\beta_0 \beta_1}{x^2 \sin^2 \psi} \right) \right) \\
 & + \left(\beta_1 - \frac{\alpha_1 \beta_0}{\alpha_0} \right) \left(\frac{\rho v''}{\sin \psi} - \frac{\rho'' v}{\sin \psi} + \frac{\rho \beta_0 \bar{\bar{U}}}{x^2 \sin^2 \psi} \right) w_0.
 \end{aligned} \tag{3.54}$$

From considering the incompressible flow case studied by Hussain (2009), the next step is to asymptotically match the leading order eigensolution in the viscous wall layer (3.48) to the first-order solution in the inviscid zone (3.54). However, this method cannot be followed for the compressible flow case. Hussain (2009) uses the substitution

$$\phi = \left(\alpha_0 U_0 + \beta_0 V_0 / r \right)', \tag{3.55}$$

and let $\tau = \gamma\xi$, where

$$\gamma = \left(i(\alpha_0 r U'(0) + \beta_0 V'(0)) \right)^{\frac{1}{3}}. \quad (3.56)$$

This transforms the incompressible flow version of equation (3.48) into the ordinary differential equation

$$\phi_{\tau\tau} - \tau\phi = 0. \quad (3.57)$$

This has an analytic solution given by an Airy function which is then matched to the incompressible flow version of Equation (3.54). Due to the complication of the added temperature distribution terms in Equation (3.48), such a substitution is not possible. As no adequate alternative has been found, the problem is left open and the equations are included for completeness.

There is a gap in the literature on this problem for theoretical studies into compressible flows over rotating boundary layers. It is suggested that this problem is revisited in a later study to find a way of extending the method for the incompressible case such that a solution can be found when taking into account the added terms found in the compressible analysis.

Chapter 4

Viscous Type II Modes

In this chapter we consider a triple deck structure to study the stability of the stationary viscous modes, following the method used for the compressible rotating disk case by Seddougui (1990). Rather than the previous condition for the inviscid modes, where we required $\overline{\overline{U}} = \overline{\overline{U}}' = 0$ at the location of the critical layer, the condition used for the viscous stationary modes is that at leading order the effective wall shear is given by $\alpha u' x \sin \psi + \beta v' = 0$. This will be discussed in more detail as we progress.

We base the analysis around the small parameter

$$\epsilon = R^{-\frac{1}{16}}, \tag{4.1}$$

which as in §3 is entirely suitable as we are considering a high Reynolds-

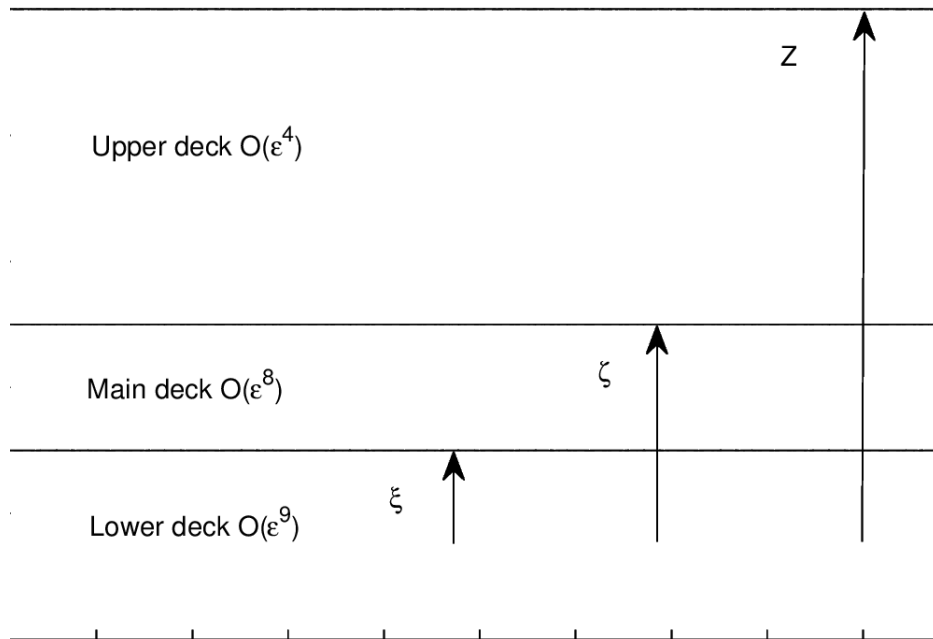


Figure 4.1: Diagram of the triple-deck structure.

number flow and $\epsilon \rightarrow 0$ as $R \rightarrow \infty$. Then the upper, main and lower decks are of thickness $O(\epsilon^4)$, $O(\epsilon^8)$ and $O(\epsilon^9)$ respectively. The triple deck structure follows that found by Smith (1979) for the Blasius flow, and is shown in Figure 4.1. The triple deck structure is used to remove a singularity caused by flow separation. The separation occurs when the part of the boundary layer closest to the cone wall reverses in flow direction, caused by an adverse pressure gradient. The fluid then becomes detached from the cone wall, leading to the spiral vortices seen experimentally. The upper deck is inviscid and irrotational and creates a pressure gradient which drives the flow in the lower deck. The

main deck is also inviscid with no pressure change across the layer. All viscous effects are contained in the lower deck, which has to satisfy the no slip condition on the surface of the cone.

We seek a stationary normal modes solution for the axial flow perturbation given by

$$\tilde{u} = u(Z)\exp\left(\frac{i}{\epsilon^4}\left\{\int^x \alpha(x, \epsilon)dx + \beta(\epsilon)\theta\right\}\right) \quad (4.2)$$

with similar expressions for the other perturbations $\tilde{v}, \tilde{w}, \tilde{p}, \tilde{\rho}, \tilde{T}$. The stream-wise and azimuthal wavenumbers are expanded as

$$\alpha = \alpha_0 + \epsilon^2\alpha_1 + \epsilon^3\alpha_2 + \dots, \quad (4.3)$$

$$\beta = \beta_0 + \epsilon^2\beta_1 + \epsilon^3\beta_2 + \dots, \quad (4.4)$$

where the $O(\epsilon)$ terms are zero. As with the inviscid modes, we require $\alpha, \beta \in \mathbb{R}$ such that the flow is neutrally stable at position x .

4.1 Upper deck solutions

We let $z = \epsilon^4 Z$ so that Z is $O(1)$ in the upper deck. We expand the perturbations in the form

$$\bar{u} = \epsilon^3 u_0^U(Z) + \epsilon^4 u_1^U(Z) + \dots, \quad (4.5)$$

$$\bar{v} = \epsilon^3 v_0^U(Z) + \epsilon^4 v_1^U(Z) + \dots, \quad (4.6)$$

$$\bar{w} = \epsilon^3 w_0^U(Z) + \epsilon^4 w_1^U(Z) + \dots, \quad (4.7)$$

$$\bar{p} = \epsilon^3 p_0^U(Z) + \epsilon^4 p_1^U(Z) + \dots, \quad (4.8)$$

$$\bar{\rho} = \epsilon^3 \rho_0^U(Z) + \epsilon^4 \rho_1^U(Z) + \dots, \quad (4.9)$$

$$\bar{T} = \epsilon^3 T_0^U(Z) + \epsilon^4 T_1^U(Z) + \dots \quad (4.10)$$

Substituting these into the perturbation equations (3.9)-(3.14) and equating terms of $O(\epsilon^{-1})$ gives the leading-order equations

$$ixu\alpha_0\rho_0^U + \frac{iv\beta_0\rho_0^U}{\sin\psi} + i\rho\alpha_0u_0^U + \frac{i\rho\beta_0v_0^U}{x\sin\psi} + \frac{d\rho}{dZ}w_0^U + \rho\frac{dw_0^U}{dZ} = 0, \quad (4.11)$$

$$i\rho xu\alpha_0u_0^U + \frac{i\rho v\beta_0u_0^U}{\sin\psi} + \rho xu'w_0^U = -i\alpha_0p_0^U, \quad (4.12)$$

$$i\rho xv\alpha_0v_0^U + \frac{i\rho v\beta_0v_0^U}{\sin\psi} + \rho xv'w_0^U = -\frac{i\beta_0p_0^U}{x\sin\psi}, \quad (4.13)$$

$$i\rho xu\alpha_0w_0^U + \frac{i\rho v\beta_0w_0^U}{\sin\psi} = -\frac{dp_0^U}{dZ}, \quad (4.14)$$

$$\begin{aligned} \frac{\rho}{M_\infty^2(\gamma-1)} \left(ixu\alpha_0T_0^U + \frac{iv\beta_0T_0^U}{\sin\psi} + \frac{dT}{dZ}w_0^U \right) - \frac{dp}{dZ}w_0^U \\ = ixu\alpha_0p_0^U + \frac{i\beta_0vp_0^U}{\sin\psi}. \end{aligned} \quad (4.15)$$

In the upper deck, the basic-flow quantities take the free stream values from (2.33), given by $u = 0, v = -1, \rho = 1, T = 1$ and p is constant. This leads to the modified equations

$$-\frac{i\beta_0\rho_0^U}{\sin\psi} + i\alpha_0u_0^U + \frac{i\beta_0v_0^U}{x\sin\psi} + \frac{dw_0^U}{dZ} = 0, \quad (4.16)$$

$$\frac{\beta_0u_0^U}{\sin\psi} = \alpha_0p_0^U, \quad (4.17)$$

$$v_0^U = \frac{p_0^U}{x}, \quad (4.18)$$

$$\frac{i\beta_0w_0^U}{\sin\psi} = \frac{dp_0^U}{dZ}, \quad (4.19)$$

$$\frac{T_0^U}{M_\infty^2(\gamma - 1)} = p_0^U. \quad (4.20)$$

Reducing these equations into a single equation in p_0^U leads to

$$\frac{d^2p_0^U}{dZ^2} - \Gamma^2p_0^U = 0, \quad (4.21)$$

where the leading order wavenumber is defined by

$$\Gamma^2 = \alpha_0^2 + \frac{\beta_0^2}{x^2\sin^2\psi}(1 - M_x^2). \quad (4.22)$$

Rejecting solutions which grow as $z \rightarrow \infty$ leaves us with the solutions

$$u_0^U = \frac{\alpha_0 \sin \psi C}{\beta_0} e^{-\Gamma z}, \quad (4.23)$$

$$v_0^U = \frac{C}{x} e^{-\Gamma z}, \quad (4.24)$$

$$w_0^U = \frac{i \sin \psi \Gamma C}{\beta_0} e^{-\Gamma z}, \quad (4.25)$$

$$p_0^U = C e^{-\Gamma z}, \quad (4.26)$$

$$\rho_0^U = M_\infty^2 \sin^2 \psi C e^{-\Gamma z}, \quad (4.27)$$

$$T_0^U = (\gamma - 1) M_\infty^2 C e^{-\Gamma z}, \quad (4.28)$$

where $C = \text{constant}$.

For three-dimensional stationary modes to exist the following relation must hold,

$$\alpha_0^2 + \frac{\beta_0^2}{x^2 \sin^2 \psi} (1 - M_x^2) > 0. \quad (4.29)$$

Hence for $0 \leq M_x < 1$, there will exist three-dimensional modes for all real α_0 and β_0 . However, for $M_x > 1$, solutions still exist as long as the condition (4.29) holds. As stated by Hall (1986), in order for three-dimensional stationary modes to exist, the effective wall shear must be equal to zero at leading order.

Hence we require

$$\alpha_0 \frac{\partial U}{\partial z} + \frac{\beta_0}{x \sin \psi} \frac{\partial V}{\partial z} = 0 \text{ at } z = 0, \quad (4.30)$$

where U and V are the basic flow quantities given in (2.27).

We find the streamline and azimuthal velocity gradients by finding the value of the solution to Equations (2.30)–(2.31) at $z = 0$, and have the values

$$\frac{\partial U(0)}{\partial z} = 0.51023, \quad \frac{\partial V(0)}{\partial z} = -0.61592, \quad (4.31)$$

leading to

$$\frac{\alpha_0 x \sin \psi}{\beta_0} = 1.2071. \quad (4.32)$$

Hence by rearranging (4.29) we find that the three-dimensional stationary modes exist for

$$0 \leq M_x < 1.5674. \quad (4.33)$$

We note that as the local Mach number M_x depends on the half-angle ψ , a change in ψ will effect the upper limit of M_x for solutions to exist. To show this change we define $M_{90} = xM_\infty$, the local Mach number for the rotating disk case, which leads to $M_x = \sin \psi M_{90}$. We set $M_{90} = 1.5674$, which is the upper limit for $\psi = 90$, and vary the half angle. The change is shown in Table 4.1.

ψ	40	50	60	70	80	90
M_x^{max}	1.0075	1.2007	1.3574	1.4729	1.5436	1.5674

Table 4.1: The effect of a change in ψ on the maximum local Mach number M_x^{max} allowed for stationary three-dimensional modes of instability to exist.

4.2 Main deck solutions

In the main deck, we scale the wall normal and pressure perturbations in the same way as before. We scale all other perturbations by the difference in the order of ϵ between the upper and main decks, so in effect we multiply the upper deck expansions by ϵ^{-4} to obtain the main deck expansions. This means we use

$$\bar{u} = \epsilon^{-1}u_0^M(\zeta) + u_1^M(\zeta) + \dots, \tag{4.34}$$

$$\bar{v} = \epsilon^{-1}v_0^M(\zeta) + v_1^M(\zeta) + \dots, \tag{4.35}$$

$$\bar{w} = \epsilon^3w_0^M(\zeta) + \epsilon^4w_1^M(\zeta) + \dots, \tag{4.36}$$

$$\bar{p} = \epsilon^3p_0^M(\zeta) + \epsilon^4p_1^M(\zeta) + \dots, \tag{4.37}$$

$$\bar{\rho} = \epsilon^{-1}\rho_0^M(\zeta) + \rho_1^M(\zeta) + \dots, \tag{4.38}$$

$$\bar{T} = \epsilon^{-1}T_0^M(\zeta) + T_1^M(\zeta) + \dots \tag{4.39}$$

Substituting these expansions into the perturbation equations (3.9)-(3.14) leads

to the main deck equations at $O(\epsilon^{-5})$ given by

$$ixu\alpha_0\rho_0^M + \frac{iv\beta_0\rho_0^M}{\sin\psi} + i\rho\alpha_0u_0^M + \frac{i\rho\beta_0v_0^M}{x\sin\psi} + \frac{d\rho}{d\zeta}w_0^M + \rho\frac{dw_0^M}{d\zeta} = 0, \quad (4.40)$$

$$ixu\alpha_0u_0^M + \frac{iv\beta_0u_0^M}{\sin\psi} + xu'w_0^M = 0, \quad (4.41)$$

$$ixu\alpha_0v_0^M + \frac{iv\beta_0v_0^M}{\sin\psi} + xv'w_0^M = 0, \quad (4.42)$$

$$\frac{dp_0^M}{d\zeta} = 0, \quad (4.43)$$

$$\frac{\rho}{M_\infty^2(\gamma-1)} \left(ixu\alpha_0T_0^M + \frac{iv\beta_0T_0^M}{\sin\psi} + \frac{dT}{d\zeta}w_0^M \right) = 0. \quad (4.44)$$

Prandtl matching between the upper and main decks implies that

$$\lim_{\zeta \rightarrow \infty} p_0^M(\zeta) = \lim_{Z \rightarrow 0} p_0^U(Z) = C \quad (4.45)$$

From (4.43) $p_0^M(\zeta) = \text{constant}$, hence $p_0^M(\zeta) = C$. Eliminating u_0^M and v_0^M from the continuity equation (4.40) and integrating the resulting equation leads to the main deck equations given by

$$u_0^M = \frac{\sin^2\psi\Gamma C xu'}{\beta_0^2}, \quad (4.46)$$

$$v_0^M = \frac{\sin^2\psi\Gamma C xv'}{\beta_0^2}, \quad (4.47)$$

$$w_0^M = -\frac{i\sin^2\psi\Gamma C}{\beta_0^2} \left(\alpha_0xu + \frac{\beta_0v}{\sin\psi} \right), \quad (4.48)$$

$$p_0^M = C, \quad (4.49)$$

$$\rho_0^M = \frac{\sin^2\psi\Gamma C}{\beta_0^2} \frac{d\rho}{d\zeta}, \quad (4.50)$$

$$T_0^M = \frac{M_\infty^2(\gamma-1)\sin^2\psi\Gamma C}{\beta_0^2} \frac{dT}{d\zeta}, \quad (4.51)$$

after matching with the previous upper deck equations. Here the wall normal velocity w_0^M satisfies the usual no slip condition at $\zeta = 0$, whereas u_0^M and v_0^M do not. This is because of the condition of zero wall shear at leading order given in (4.30), and we are required to choose α_0 and β_0 to satisfy this condition.

4.3 Lower deck solutions

We now let $z = \epsilon^3 \xi$, such that $\xi = O(1)$ in the lower deck. For small ζ we expand the basic flow components u, v, ρ and T , which in terms of ξ are given by

$$u = \epsilon u_0 \xi + \epsilon^2 u_1 \xi^2 + \epsilon^3 u_2 \xi^3 + \dots, \quad (4.52)$$

$$v = \epsilon v_0 \xi + \epsilon^2 v_1 \xi^2 + \epsilon^3 v_2 \xi^3 + \dots, \quad (4.53)$$

$$\rho = \rho_w + \epsilon \rho_0 \xi + \epsilon^2 \rho_1 \xi^2 + \dots, \quad (4.54)$$

$$T = T_w + \epsilon T_0 \xi + \epsilon^2 T_1 \xi^2 + \dots, \quad (4.55)$$

where ρ_w and T_w are the density and the temperature at the cone's wall respectively. The basic flow terms are now given by

$$u_{j-1} = \frac{1}{j!} \frac{\partial^j u}{\partial z^j} \Big|_{\zeta=0} \quad (4.56)$$

with similar expressions for v_{j-1} , ρ_{j-1} and T_{j-1} . The lower deck perturbation fields are given by

$$\bar{u} = \frac{u_{-1}^L(\xi)}{\epsilon} + u_0^L(\xi) + \epsilon u_1^L(\xi) + \dots, \quad (4.57)$$

$$\bar{v} = \frac{v_{-1}^L(\xi)}{\epsilon} + v_0^L(\xi) + \epsilon v_1^L(\xi) + \dots, \quad (4.58)$$

$$\bar{w} = \epsilon^3 w_0^L(\xi) + \epsilon^4 w_1^L(\xi) + \dots, \quad (4.59)$$

$$\bar{p} = \epsilon^3 p_0^L(\xi) + \epsilon^4 p_1^L(\xi) + \dots, \quad (4.60)$$

$$\bar{\rho} = \frac{\rho_{-1}^L(\xi)}{\epsilon} + \rho_0^L(\xi) + \epsilon \rho_1^L(\xi) + \dots, \quad (4.61)$$

$$\bar{T} = \frac{T_{-1}^L(\xi)}{\epsilon} + T_0^L(\xi) + \epsilon T_1^L(\xi) + \dots, \quad (4.62)$$

Upon matching with the leading order terms from the main deck solutions, and substituting in the basic flow expansions, this leads to the lower deck perturbation terms (in term of ξ) given by

$$\bar{u} = \frac{\sin^2 \psi x \Gamma C}{\epsilon \beta_0^2} (u_0 + 2\epsilon u_1 \xi + \dots) + \frac{u_{-1}^L}{\epsilon} + u_0^L + \epsilon u_1^L + \dots, \quad (4.63)$$

$$\bar{v} = \frac{\sin^2 \psi x \Gamma C}{\epsilon \beta_0^2} (v_0 + 2\epsilon v_1 \xi + \dots) + \frac{v_{-1}^L}{\epsilon} + v_0^L + \epsilon v_1^L + \dots, \quad (4.64)$$

$$\begin{aligned} \bar{w} = & - \frac{i \sin^2 \psi \Gamma C \epsilon^5}{\beta_0^2} \left\{ \left(\alpha_0 u_1 x + \frac{\beta_0 v_1}{\sin \psi} \right) \xi^2 + \epsilon \left(\alpha_0 x u_2 + \frac{\beta_0 v_2}{\sin \psi} \right) \xi^3 + \dots \right\} \\ & + \epsilon^6 w_0^L + \epsilon^7 w_1^L + \dots, \end{aligned} \quad (4.65)$$

$$\bar{p} = \epsilon^3 p_0^L + \epsilon^4 p_1^L + \dots, \quad (4.66)$$

$$\bar{\rho} = \frac{\sin^2 \psi \Gamma C}{\epsilon \beta_0^2} (\rho_0 + 2\epsilon \rho_1 \xi + \dots) + \frac{\rho_{-1}^L}{\epsilon} + \rho_0^L + \epsilon \rho_1^L + \dots, \quad (4.67)$$

$$\bar{T} = \frac{M_\infty^2 (\gamma - 1) \sin^2 \psi \Gamma C}{\epsilon \beta_0^2} (T_0 + 2\epsilon T_1 \xi + \dots) + \frac{T_{-1}^L}{\epsilon} + T_0^L + \epsilon T_1^L + \dots \quad (4.68)$$

Substituting these relations into the perturbations equations yields the lower deck governing equations. We first concentrate on the continuity equation, where equating terms at $O(\epsilon^{-5})$ yields

$$\left(x u \alpha_0 + \frac{\beta_0 v}{\sin \psi} \right) \rho_{-1}^L + \rho \left(\alpha_0 u_{-1}^L + \frac{\beta_0 v_{-1}^L}{x \sin \psi} \right) = 0, \quad (4.69)$$

and at $O(\epsilon^{-4})$ we find

$$\left(x u \alpha_0 + \frac{\beta_0 v}{\sin \psi} \right) \rho_0^L + \rho \left(\alpha_0 u_0^L + \frac{\beta_0 v_0^L}{x \sin \psi} \right) = 0, \quad (4.70)$$

We next consider the streamwise perturbation equation. Equating terms of $O(\epsilon^{-3})$ leads to the governing ordinary differential equation for $u_{-1}^L(\xi)$, given

by

$$\frac{d^2 u_{-1}^L}{d\xi^2} - i\rho \left(\alpha_0 x u_1 + \frac{\beta_0 v_1}{\sin \psi} \right) \xi^2 u_{-1}^L = 0 \quad (4.71)$$

The boundary conditions for this ordinary differential equation are given by the no slip condition and the zero wall normal perturbation at $O(\epsilon^{-1})$. Hence

$$u_{-1}^L = -\frac{\sin^2 \psi x \Gamma C u_0}{\beta_0^2} \quad \text{for } \xi = 0, \quad (4.72)$$

$$u_{-1}^L \rightarrow 0 \quad \text{as } \xi \rightarrow \infty. \quad (4.73)$$

Taking equation (4.71) and using the substitution

$$\nu = \sqrt{2} \Delta^{\frac{1}{4}} \xi, \quad (4.74)$$

where

$$\Delta = \frac{i}{T_w} \left(\alpha_0 x u_1 + \frac{\beta_0 v_1}{\sin \psi} \right). \quad (4.75)$$

This leads to the parabolic cylinder ordinary differential equation for u_{-1}^L ,

$$\frac{d^2 u_{-1}^L}{d\nu^2} - \frac{\rho^2}{4} u_{-1}^L = 0, \quad (4.76)$$

subject to the boundary conditions

$$u_{-1}^L = -\frac{\sin^2 \psi x \Gamma C u_0}{\beta_0^2} \quad \text{for } \nu = 0, \quad (4.77)$$

$$u_{-1}^L \rightarrow 0 \quad \text{as } \nu \rightarrow \infty. \quad (4.78)$$

Solving this ordinary differential equation subject to these boundary conditions, and taking only solutions which decay as $\nu \rightarrow \infty$, leads to the solution for u_{-1}^L given by

$$u_{-1}^L(\xi) = -\frac{\sin^2 \psi x \Gamma C u_0}{\beta_0^2} \frac{U(0, \sqrt{2} \Delta^{\frac{1}{4}} \xi)}{U(0, 0)} \quad (4.79)$$

where $U(0, \sqrt{2} \Delta^{\frac{1}{4}} \xi)$ is a parabolic cylinder function, values for which are given in Abramowitz & Stegun (1964).

We find the solution for v_{-1}^L by considering the condition (4.30) and is given by

$$v_{-1}^L(\xi) = \frac{\alpha_0 \sin^3 \psi x^2 \Gamma C u_0}{\beta_0^3} \frac{U(0, \sqrt{2} \Delta^{\frac{1}{4}} \xi)}{U(0, 0)}. \quad (4.80)$$

Then using the energy and state equations we find

$$T_{-1}^L(\xi) = -\frac{\sin^2 \psi \Gamma C T_0}{\beta_0^2} \frac{U(0, \sqrt{2} \sigma^{\frac{1}{4}} \Delta^{\frac{1}{4}} \xi)}{U(0, 0)} \quad (4.81)$$

$$\rho_{-1}^L(\xi) = -\frac{\sin^2 \psi \Gamma C \rho_0}{\beta_0^2} \frac{U(0, \sqrt{2} \sigma^{\frac{1}{4}} \Delta^{\frac{1}{4}} \xi)}{U(0, 0)} \quad (4.82)$$

4.4 First order lower-deck solutions

Our next aim is to find the next order values $u_0^L(\xi)$ and $v_0^L(\xi)$. To do this we must first solve for $w_1^L(\xi)$, which requires looking at the next order approximation to the perturbation equations. Considering the continuity equation at

$O(\epsilon^{-3})$ yields

$$i\alpha_0 u_1^L + \frac{i\beta_0 v_1^L}{x \sin \psi} + \frac{dw_0^L}{d\xi} = -\frac{i \sin^2 \psi x \Gamma C}{\beta_0^2} \left(\alpha_1 u_0 + \frac{\beta_1 v_0}{x \sin \psi} \right) \quad (4.83)$$

$$-i \left(\alpha_1 u_{-1}^L + \frac{\beta_1 v_{-1}^L}{x \sin \psi} \right) - \frac{ix\alpha_0 u_1 \xi^2 \rho_{-1}^L}{\rho_w},$$

and the surface-normal perturbation equation at $O(\epsilon^{-6})$ yields

$$\frac{dp_0}{d\xi} = 0. \quad (4.84)$$

Matching with the main deck pressure solution leads to

$$p_0^L(\xi) = C. \quad (4.85)$$

The streamwise perturbation expansion at $O(\epsilon^{-1})$ leads to

$$\begin{aligned}
 & \rho_w \left\{ i \left(x\alpha_1 u_1 \xi^2 + x\alpha_2 u_0 \xi + \frac{\beta_1 v_1 \xi^2}{\sin \psi} + \frac{\beta_2 v_0 \xi}{\sin \psi} \right) \left(\frac{\sin^2 \psi \Gamma C x u_0}{\beta_0^2} + u_{-1}^L \right) \right. \\
 & + i \left(x\alpha_0 u_2 \xi^3 + x\alpha_1 u_0 \xi + \frac{\beta_0 v_2 \xi^3}{\sin \psi} + \frac{\beta_1 v_0 \xi}{\sin \psi} \right) \left(\frac{2 \sin^2 \psi \Gamma C x \xi u_1}{\beta_0^2} + u_0^L \right) \\
 & + i \xi^2 \left(x\alpha_0 u_1 + \frac{\beta_0 v_1}{\sin \psi} \right) u_1^L - 2 \left(\frac{\sin^2 \psi x \Gamma C v_0}{\beta_0^2} + v_{-1}^L \right) \\
 & \quad - \frac{3i \sin^2 \psi \Gamma C x u_2 \xi^4}{\beta_0^2} \left(\alpha_0 u_1 x + \frac{\beta_0 v_1}{\sin \psi} \right) \\
 & \quad \left. - \frac{2i \sin^2 \psi \Gamma C x u_1 \xi^4}{\beta_0^2} \left(\alpha_0 x u_2 + \frac{\beta_0 v_2}{\sin \psi} \right) + 2x u_1 \xi w_0^L \right\} \\
 & + \rho_0 \xi \left\{ i \left(x\alpha_0 u_2 \xi^3 + x\alpha_1 u_0 \xi + \frac{\beta_0 v_2 \xi^3}{\sin \psi} + \frac{\beta_1 v_0 \xi}{\sin \psi} \right) \left(\frac{\sin^2 \psi \Gamma C x u_0}{\beta_0^2} + u_{-1}^L \right) \right. \\
 & \quad + i \left(x\alpha_0 u_1 \xi^2 + \frac{\beta_0 v_1 \xi^2}{\sin \psi} \right) \left(\frac{2 \sin^2 \psi \Gamma C x \xi u_1}{\beta_0^2} + u_0^L \right) \\
 & \quad + i \left(x\alpha_0 u_0 \xi + \frac{\beta_0 v_0 \xi}{\sin \psi} \right) u_1^L - \frac{2i \sin^2 \psi \Gamma C x u_1 \xi^3}{\beta_0^2} \left(\alpha_0 u_1 x + \frac{\beta_0 v_1}{\sin \psi} \right) \\
 & \quad - \frac{i \sin^2 \psi \Gamma C x u_0 \xi^3}{\beta_0^2} \left(\alpha_0 x u_2 + \frac{\beta_0 v_2}{\sin \psi} \right) + x u_0 w_0^L - \frac{\sin^2 \psi \Gamma C x}{\xi \beta_0^2} \left. \right\} \\
 & \quad + \rho_1 \xi^2 \left\{ i \left(x\alpha_0 u_1 \xi^2 + \frac{\beta_0 v_1 \xi^2}{\sin \psi} \right) \left(\frac{\sin^2 \psi \Gamma C x u_0}{\beta_0^2} + u_{-1}^L \right) \right. \\
 & \quad \left. + i \left(x\alpha_0 u_0 \xi + \frac{\beta_0 v_0 \xi}{\sin \psi} \right) \left(\frac{2 \sin^2 \psi \Gamma C x \xi u_1}{\beta_0^2} + u_0^L \right) \right. \\
 & \quad \left. - \frac{i \sin^2 \psi \Gamma C x u_0 \xi^2}{\beta_0^2} \left(\alpha_0 u_1 x + \frac{\beta_0 v_1}{\sin \psi} \right) \right\} - x \rho_{-1}^L = -i \alpha_0 p_0^L + T_w \frac{d^2 u_1^L}{d\xi^2}.
 \end{aligned} \tag{4.86}$$

Then considering the azimuthal perturbation expansion at $O(\epsilon^{-1})$ leads to

$$\begin{aligned}
 & \rho_w \left\{ i \left(x\alpha_1 u_1 \xi^2 + x\alpha_2 u_0 \xi + \frac{\beta_1 v_1 \xi^2}{\sin \psi} + \frac{\beta_2 v_0 \xi}{\sin \psi} \right) \left(\frac{\sin^2 \psi \Gamma C x v_0}{\beta_0^2} + v_{-1}^L \right) \right. \\
 & + i \left(x\alpha_0 u_2 \xi^3 + x\alpha_1 u_0 \xi + \frac{\beta_0 v_2 \xi^3}{\sin \psi} + \frac{\beta_1 v_0 \xi}{\sin \psi} \right) \left(\frac{2 \sin^2 \psi \Gamma C x \xi v_1}{\beta_0^2} + v_0^L \right) \\
 & + i \xi^2 \left(x\alpha_0 u_1 + \frac{\beta_0 v_1}{\sin \psi} \right) v_1^L + 2 \left(\frac{\sin^2 \psi x \Gamma C u_0}{\beta_0^2} + u_{-1}^L \right) \\
 & \quad - \frac{3i \sin^2 \psi \Gamma C x v_2 \xi^4}{\beta_0^2} \left(\alpha_0 u_1 x + \frac{\beta_0 v_1}{\sin \psi} \right) \\
 & \quad - \left. \frac{2i \sin^2 \psi \Gamma C x v_1 \xi^4}{\beta_0^2} \left(\alpha_0 x u_2 + \frac{\beta_0 v_2}{\sin \psi} \right) + 2x v_1 \xi w_0^L \right\} \\
 & + \rho_0 \xi \left\{ i \left(x\alpha_0 u_2 \xi^3 + x\alpha_1 u_0 \xi + \frac{\beta_0 v_2 \xi^3}{\sin \psi} + \frac{\beta_1 v_0 \xi}{\sin \psi} \right) \left(\frac{\sin^2 \psi \Gamma C x v_0}{\beta_0^2} + v_{-1}^L \right) \right. \\
 & \quad + i \left(x\alpha_0 u_1 \xi^2 + \frac{\beta_0 v_1 \xi^2}{\sin \psi} \right) \left(\frac{2 \sin^2 \psi \Gamma C x \xi v_1}{\beta_0^2} + v_0^L \right) \\
 & \quad + i \left(x\alpha_0 u_0 \xi + \frac{\beta_0 v_0 \xi}{\sin \psi} \right) v_1^L - \frac{2i \sin^2 \psi \Gamma C x v_1 \xi^3}{\beta_0^2} \left(\alpha_0 u_1 x + \frac{\beta_0 v_1}{\sin \psi} \right) \\
 & \quad - \left. \frac{i \sin^2 \psi \Gamma C x v_0 \xi^3}{\beta_0^2} \left(\alpha_0 x u_2 + \frac{\beta_0 v_2}{\sin \psi} \right) + x v_0 w_0^L \right\} \\
 & + \rho_1 \xi^2 \left\{ i \left(x\alpha_0 u_1 \xi^2 + \frac{\beta_0 v_1 \xi^2}{\sin \psi} \right) \left(\frac{\sin^2 \psi \Gamma C x v_0}{\beta_0^2} + v_{-1}^L \right) \right. \\
 & \quad + i \left(x\alpha_0 u_0 \xi + \frac{\beta_0 v_0 \xi}{\sin \psi} \right) \left(\frac{2 \sin^2 \psi \Gamma C x \xi v_1}{\beta_0^2} + v_0^L \right) \\
 & \quad - \left. \frac{i \sin^2 \psi \Gamma C x v_0 \xi^2}{\beta_0^2} \left(\alpha_0 u_1 x + \frac{\beta_0 v_1}{\sin \psi} \right) \right\} = -\frac{i\beta_0}{x \sin \psi} p_0^L + T_w \frac{d^2 v_1^L}{d\xi^2}.
 \end{aligned} \tag{4.87}$$

Following Hussain (2009) we simplify these equations using the operation

$i\alpha_0(4.86) + \frac{i\beta_0}{x \sin \psi}(4.87)$. Then using the relations in (4.56) we can expand the

streamwise and azimuthal laminar flow equations (2.30)-(2.31) to find

$$u_1 = \frac{U''(0)}{2!} = -\frac{1}{2}, \quad (4.88)$$

$$v_1 = \frac{V''(0)}{2!} = 0. \quad (4.89)$$

Differentiating (2.30)-(2.31) then leads to

$$u_2 = \frac{U'''(0)}{3!} = -\frac{2V'(0)}{3!} = -\frac{v_0}{3}, \quad (4.90)$$

$$v_2 = \frac{V'''(0)}{3!} = \frac{2U'(0)}{3!} = \frac{u_0}{3}. \quad (4.91)$$

We eliminate u_1^L and v_1^L from the resulting equation using Equation (4.83), and simplify using Equations (4.69) and (4.71) leads to an ordinary differential equation in w_0^L , with solution

$$\begin{aligned} w_0^L = & -i \left(\alpha_1 x u_0 + \frac{\beta_1 v_0}{\sin \psi} \right) \frac{\Gamma \sin^2 \psi C \xi}{\beta_0^2} + k_1 \xi^2 \quad (4.92) \\ & + \Delta^{-\frac{3}{4}} \left\{ \gamma_0^2 C F_1(s) + \frac{2i \gamma_0^2 \Gamma x \sin^3 \psi C u_0}{\beta_0^3 T_w U(0,0)} F_2(s) - \frac{3i \alpha_0 \Gamma x \sin^2 \psi C \rho_0}{\beta_0^2 U(0,0)} F_3(s) \right. \\ & \left. + \frac{i(1-\sigma) \alpha_0 \Gamma x \sin^2 \psi C \rho_0}{2\beta_0^2 U(0,0)} F_4(s) \right\}, \end{aligned}$$

where $s = \Delta^{\frac{1}{4}} \xi$ and $k_1 = \text{constant}$.

The independent solutions $F_1(s), F_2(s), F_3(s)$ and $F_4(s)$ satisfy the following

$$F_1''' - s^2 F_1' + 2s F_1 = 1, \quad (4.93)$$

$$F_2''' - s^2 F_2' + 2s F_2 = U(0, \sqrt{2}\sigma^{\frac{1}{4}}s), \quad (4.94)$$

$$F_3''' - s^2 F_3' + 2s F_3 = \frac{d}{ds} \left(s U(0, \sqrt{2}\sigma^{\frac{1}{4}}s) \right), \quad (4.95)$$

$$F_4''' - s^2 F_4' + 2s F_4 = s^4 U(0, \sqrt{2}\sigma^{\frac{1}{4}}s), \quad (4.96)$$

satisfying the boundary conditions

$$F_i(0) = F_i(\infty) = 0 \text{ for } i = 1, 2, 3, 4. \quad (4.97)$$

Considering the continuity equation (4.83) at $\xi = 0$ finds

$$\begin{aligned} & i\alpha_0 u_1^L(0) + \frac{i\beta_0 v_1^L(0)}{x \sin \psi} + \frac{dw_0^L(0)}{d\xi} \\ &= \frac{i \sin^2 \psi x \Gamma C}{\beta_0^2} \left(\alpha_1 u_0 + \frac{\beta_1 v_0}{x \sin \psi} \right) - i \left(\alpha_1 u_{-1}^L(0) + \frac{\beta_1 v_{-1}^L(0)}{x \sin \psi} \right), \end{aligned} \quad (4.98)$$

Hence differentiating (4.92) and satisfying the boundary conditions at $\xi = 0$ yields

$$\begin{aligned} & \gamma_0^2 F_1'(0) + \frac{2i\gamma_0^2 \Gamma x \sin^3 \psi u_0}{\beta_0^3 T_w U(0, 0)} F_2'(0) - \frac{3i\alpha_0 \Gamma x \sin^2 \psi \rho_0}{\beta_0^2 U(0, 0)} F_3'(0) \\ & \quad + \frac{i(1-\sigma)\alpha_0 \Gamma x \sin^2 \psi \rho_0}{2\beta_0^2 U(0, 0)} F_4'(0) \\ &= \frac{(1+i)\Gamma \sin^2 \psi (\alpha_0 x)^{\frac{1}{2}}}{2\beta_0^2 T_w} \left(\alpha_1 u_0 + \frac{\beta_1 v_0}{x \sin \psi} \right). \end{aligned} \quad (4.99)$$

Taking the real and imaginary parts of this equation leads to

$$\gamma_0^2 F_1'(0) = \frac{\Gamma \sin^2 \psi (\alpha_0 x)^{\frac{1}{2}}}{2\beta_0^2 T_w} \left(\alpha_1 u_0 + \frac{\beta_1 v_0}{x \sin \psi} \right) \quad (4.100)$$

$$\frac{2\gamma_0^2 \Gamma x \sin^3 \psi u_0}{\beta_0^3 T_w U(0,0)} F_2'(0) - \frac{3\alpha_0 \Gamma x \sin^2 \psi \rho_0}{\beta_0^2 U(0,0)} F_3'(0) \quad (4.101)$$

$$+ \frac{(1-\sigma)\alpha_0 \Gamma x \sin^2 \psi \rho_0}{2\beta_0^2 U(0,0)} F_4'(0) = \frac{\Gamma \sin^2 \psi (\alpha_0 x)^{\frac{1}{2}}}{2\beta_0^2 T_w} \left(\alpha_1 u_0 + \frac{\beta_1 v_0}{x \sin \psi} \right).$$

Then substituting (4.100) into (4.101) we find the eigenrelation

$$\begin{aligned} \gamma_0^2 F_1'(0) - \frac{2\gamma_0^2 \Gamma x \sin^3 \psi u_0}{\beta_0^3 T_w U(0,0)} F_2'(0) + \frac{3\alpha_0 \Gamma x \sin^2 \psi \rho_0}{\beta_0^2 U(0,0)} F_3'(0) \\ - \frac{(1-\sigma)\alpha_0 \Gamma x \sin^2 \psi \rho_0}{2\beta_0^2 U(0,0)} F_4'(0) = 0. \end{aligned} \quad (4.102)$$

We now aim to find the values of $F_1'(0), F_2'(0), F_3'(0)$ and $F_4'(0)$, and to do this we follow the method of Hall (1986) (but outlined fully by Hussain (2009)) by transforming Equations (4.93)-(4.96) such that they can be solved in terms of the parabolic cylinder equations.

For F_1 we begin by letting $G = \frac{F_1}{s^2}$, which upon substitution into (4.93) leads to

$$s^2 G''' + 6sG'' + (6 - s^4)G' = 1. \quad (4.103)$$

This can be reduced to a second order differential equation via $H = G'$, given by

$$s^2 H'' + 6sH' + (6 - s^4)H = 1. \quad (4.104)$$

Making the change of variable $K = s^3H$, along with $u = \sqrt{2}s$, leads to the parabolic cylinder equation given by

$$K''(u) - \frac{u^2}{4}K(u) = \frac{u}{2\sqrt{2}}. \quad (4.105)$$

We let $K(u) = R(u)U(0, u)$ to obtain

$$R''U + 2R'U' = \frac{u}{2\sqrt{2}}. \quad (4.106)$$

Solving for R' using the method of integrating factors leads to

$$R' = \frac{1}{2\sqrt{2}} \frac{\int_{\infty}^u \theta U(0, \theta) d\theta}{U(0, u)^2}. \quad (4.107)$$

Rewriting this equation back in terms of F_1 we find

$$uF_1'(u) - 2F_1(u) = R(u)U(0, u). \quad (4.108)$$

Setting $u = 0$ and using the boundary condition (4.97) (noting that $s = 0 \Rightarrow u = 0$) gives the condition $R(0) = 0$. Differentiating (4.108) and a change of variable from u back to s leads to

$$F_1'(0) = \frac{\int_0^{\infty} \theta U(0, \theta) d\theta}{2U(0, 0)}. \quad (4.109)$$

A similar method is used to find $F_2'(0)$, $F_3'(0)$ and $F_4'(0)$, taking into account the changes in the right-side side of (4.94)-(4.96). To estimate each respective $F_i'(0)$ we follow Hussain (2009) by using a Simpson's rule method from $\theta = 0$ to

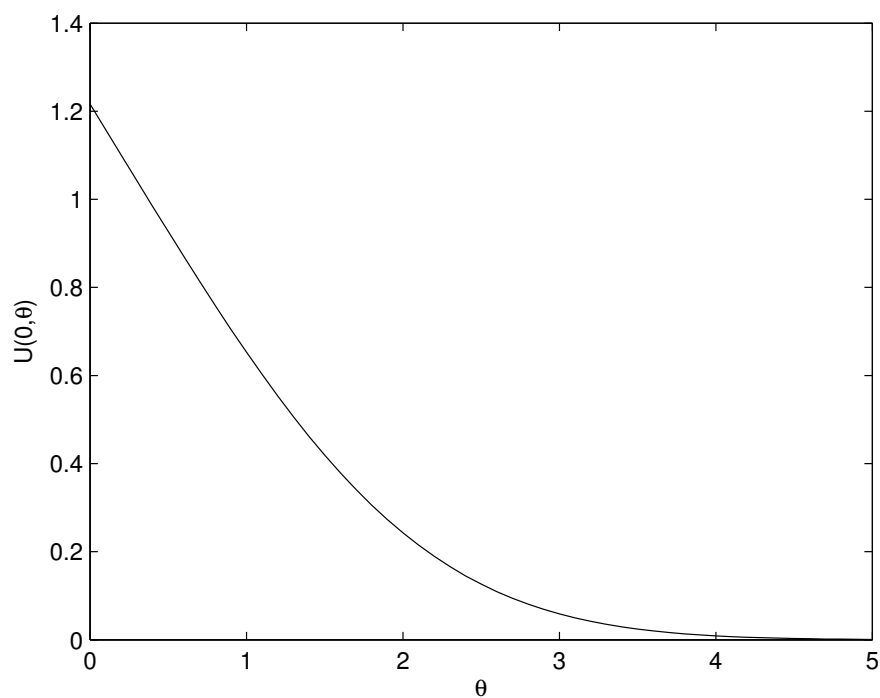


Figure 4.2: The graph of $U(0, \theta)$, showing the decay over the region of integration from $\theta = 0$ to $\theta = 5$.

$\theta = 5$ with a fixed step size of 0.1, noting that the parabolic cylinder function $U(0, \theta)$ decays exponentially (as shown in Figure 4.2). Using this method we

find that

$$F'_1(0) = 0.5984, \quad (4.110)$$

$$F'_2(0) = 0.2779, \quad (4.111)$$

$$F'_3(0) = 0.0192, \quad (4.112)$$

$$F'_4(0) = 1.6972. \quad (4.113)$$

We note here that the value found for $F'_1(0)$ is in agreement with Hussain (2009), and differs from that found by Hall (1986) and Seddougui (1990). As discussed by Hussain (2009), this is possibly be due to the choice of integration method.

Using (4.30), we can rewrite Equation (4.102) in terms of the leading order wavenumber to find

$$\begin{aligned} \gamma_0 = (F'_1(0))^{-\frac{1}{2}} & \left(1 + \frac{v_0^2}{u_0^2} - M_x^2 \right)^{\frac{1}{4}} \left(\frac{2u_0 F'_2(0)}{T_w^2 x U(0,0)} \left(1 + \frac{v_0^2}{u_0^2} \right) \right. \\ & \left. + \frac{3v_0 \rho_0 F'_3(0)}{u_0 x U(0,0)} - \frac{(1-\sigma)v_0 \rho_0 F'_4(0)}{2u_0 x U(0,0)} \right)^{\frac{1}{2}}. \end{aligned} \quad (4.114)$$

From the equation of state we have the relation $\rho_0 = -\frac{T_0}{T_w}$, so we proceed by differentiating the temperature relation (2.34) leads to

$$T_0 = -\frac{\gamma-1}{2} M_x^2 f'(0) + (T_w - 1)q'(0) \quad (4.115)$$

where $f'(0) = -0.4562$ and $q'(0) = -0.3241$ are found numerically. These values are different to those found by Seddougui (1990), where a slightly dif-

ferent temperature relation was used, as well as being computed with $\sigma = 0.72$ instead of $\sigma = 0.7$ used here.

Substituting all known values into Equation (4.114) leads to the following simplified equation for the leading order wavenumber

$$\gamma_0 = \frac{1.293x^{-\frac{1}{2}}}{T_w}(2.457 - M_x^2)^{\frac{1}{4}}(0.573 + 0.310T_0)^{\frac{1}{2}} \quad (4.116)$$

where

$$T_0 = 0.091M_x^2 - 0.3241(T_w - 1) \quad (4.117)$$

Following the same method we rewrite the real part of the eigenrelation (4.100)

to find the waveangle estimates given by

$$\sin \psi \left(\frac{\alpha_1}{\beta_0} - \frac{\alpha_0\beta_1}{\beta_0^2} \right) = \frac{2\gamma^{\frac{3}{2}}T_w^2F_1'(0)}{|u_0v_0|^{\frac{1}{2}}x^{\frac{1}{2}}} \left(1 + \frac{v_0^2}{u_0^2} - M_x^2 \right)^{-\frac{1}{2}} \left(1 + \frac{v_0^2}{u_0^2} \right)^{\frac{1}{4}}. \quad (4.118)$$

Substituting all known values into Equation (4.118) leads to the following simplified equation for the waveangle estimates

$$\sin \psi \left(\frac{\alpha_1}{\beta_0} - \frac{\alpha_0\beta_1}{\beta_0^2} \right) = \frac{2.669\gamma_0^{\frac{3}{2}}T_w^2}{x^{\frac{1}{2}}(2.457 - M_x^2)^{\frac{1}{2}}}. \quad (4.119)$$

As discussed by Hussain (2009), it is not possible to find α_1 and β_1 independently in this analysis. Instead we concentrate on the combination of α_1 and β_1 found in Equation (4.118) in terms of the waveangle ϕ between the stream-wise position and normal to the spiral vortices as discussed in §3.3. This leads

to

$$\begin{aligned}
 \tan\left(\frac{\pi}{2} - \phi\right) &= \frac{\alpha x}{\beta} = \frac{(\alpha_0 + \epsilon^2 \alpha_1 + \dots)x}{(\beta_0 + \epsilon^2 \beta_1 + \dots)}, & (4.120) \\
 &= \frac{\alpha_0 x}{\beta_0} + \epsilon^2 \left(\frac{\alpha_1}{\beta_0} - \frac{\alpha_0 \beta_1}{\beta_0^2}\right)x, \\
 &= \frac{1.207}{\sin \psi} + \epsilon^2 \left(\frac{\alpha_1}{\beta_0} - \frac{\alpha_0 \beta_1}{\beta_0^2}\right)x.
 \end{aligned}$$

The expanded wavenumber is scaled on the viscous mode wavelength, given by

$$\epsilon^4 \gamma = \epsilon^4 \gamma_0 + \dots \quad (4.121)$$

$$\epsilon^4 \gamma = \frac{\epsilon^4 1.293 x^{-\frac{1}{2}}}{T_w} (2.457 - M_x^2)^{\frac{1}{4}} (0.573 + 0.310 T_0)^{\frac{1}{2}} \quad (4.122)$$

Following Hussain (2009), we define the Reynolds number based on the boundary-layer thickness δ^* , given by

$$R_{\delta^*} = R^{\frac{1}{2}} x (\sin \psi)^{\frac{1}{2}}. \quad (4.123)$$

Then the local wavenumber is given by

$$\gamma_{\delta^*} = \frac{1.293 R_{\delta^*}^{-\frac{1}{2}} (\sin \psi)^{\frac{1}{4}}}{T_w} (2.457 - M_x^2)^{\frac{1}{4}} (0.573 + 0.310 T_0)^{\frac{1}{2}}, \quad (4.124)$$

and the local mode waveangle is given as

$$\tan\left(\frac{\pi}{2} - \phi\right) = \frac{1.207}{\sin \psi} + \frac{3.924 R_{\delta^*}^{-\frac{1}{4}} T^{\frac{1}{2}} (0.573 + 0.310 T_0)^{\frac{3}{4}}}{(\sin \psi)^{\frac{7}{8}} (2.457 - M_x^2)^{\frac{1}{8}}}. \quad (4.125)$$

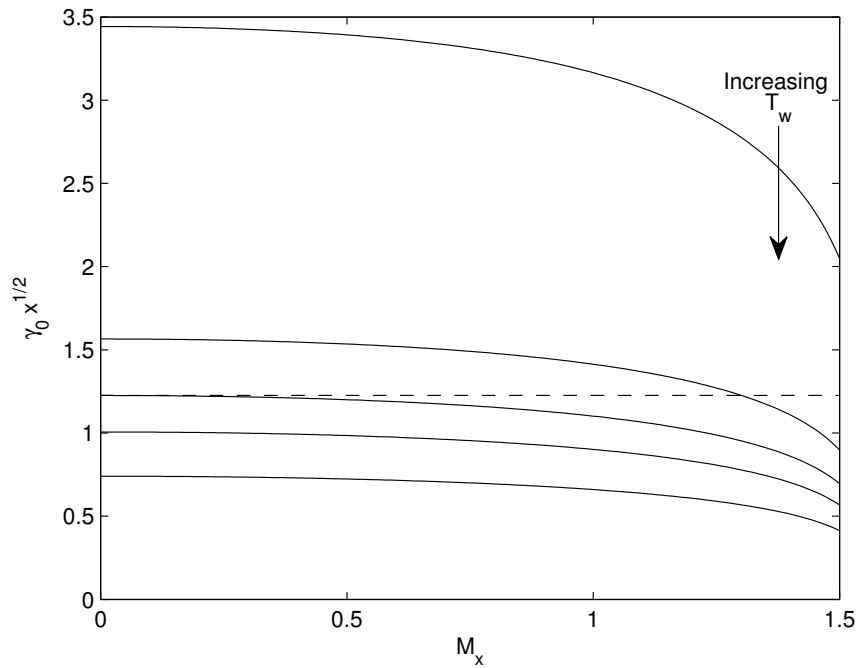


Figure 4.3: The effective wavenumber $\gamma_0 x^{\frac{1}{2}}$ for fixed $T_w = 0.4, 0.8, 1.0, 1.2, 1.6$. The solution for the incompressible case is also given (—).

4.5 Wavenumber and waveangle predictions

Figure 4.3 shows $\gamma_0 x^{\frac{1}{2}}$ as a function of M_x for $T_w = 0.4, 0.8, 1.0, 1.2, 1.6$, along with half angle $\psi = 90^\circ$. We see that the effective wavenumber of the flow decreases as the local Mach number grows, and the results are in agreement with those found by Seddougui (1990) for the compressible flow over a rotating disk. The appearance of the wall temperature, local Mach number and cone half-angle terms allow us to fully consider the effects of both compressibility,

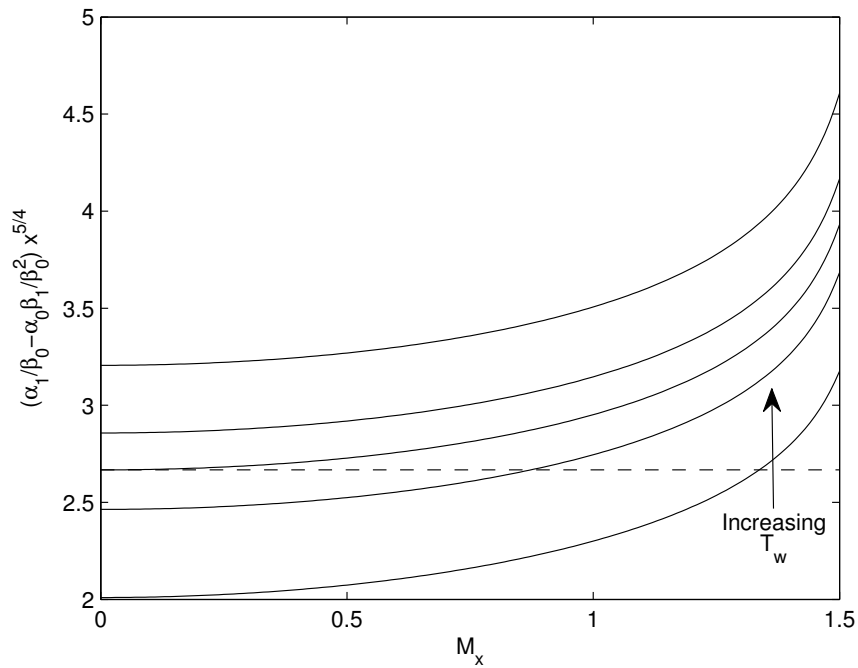


Figure 4.4: The correction to the wave angle for fixed $T_w = 0.4, 0.8, 1.0, 1.2, 1.6$. The solution for the incompressible case is also given (—).

and varying the broadness of the cone, on the stability characteristics of the flow. We see that for $T_w = 1$ the effective wavenumber is in good agreement with the incompressible case for low M_x . For $T_w > 1$ we find that the value of $\gamma_0 x^{\frac{1}{2}}$ is less than that found by Hall (1986) and Hussain (2009), which means that the wavelength of the modes is longer than in the incompressible case. The opposite is true for $T_w < 1$, suggesting wall cooling to be a stabilising feature, which is in agreement with Seddougui (1990).

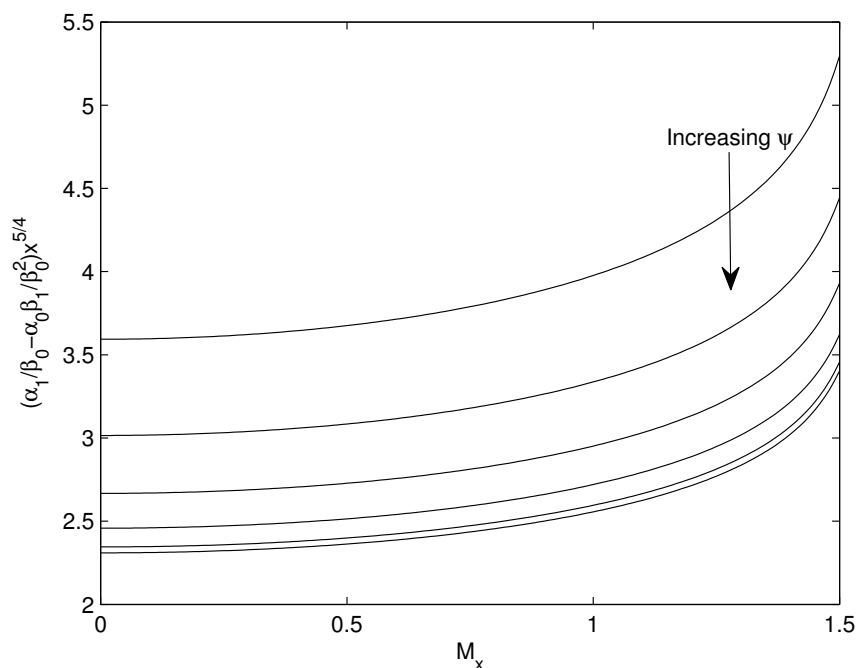


Figure 4.5: The correction to the wave angle for $T_w = 1$, with $\psi = 40^\circ - 90^\circ$ in 10° increments.

Figure 4.4 shows $(\frac{\alpha_1}{\beta_0} - \frac{\alpha_0\beta_1}{\beta_0^2})x^{5/4}$, the wave angle correction, as a function of M_x for $T_w = 0.4, 0.8, 1.0, 1.2, 1.6$, along with the incompressible result, where the half angle is $\psi = 90^\circ$. Note that again for $T_w = 1$ and low M_x the compressible case is in good agreement with the incompressible case. These results form part of Equation (4.120) to allow us to consider the orientation of the stationary vortices, given by the angle ϕ . The effect of a change in the cone half-angle on the wave angle correction is shown in Figure 4.5 for $T_w = 1$

and $\psi = 40^\circ - 90^\circ$ in increments of 10° .

Figures 4.6-4.8 show the asymptotic wavenumber prediction, using a log-log scale, and the waveangle prediction using a semi-log scale. In Figure 4.6 we have fixed $T_w = M_x = 1$ and the results show the effect of a varying half angle from $\psi = 40^\circ - 90^\circ$ in increments of 10° . In Figure 4.7 we show the effect of a change in wall temperature for $T_w = 0.4, 0.8, 1.2, 1.6$, where $\psi = 60^\circ$ and $M_x = 1$. Then in Figure 4.8 we fix $\psi = 60^\circ$ and $T_w = 1$ to show the effect of a change in local Mach number for $M_x = 0.3, 0.6, 0.9, 1.2$. Note that from Table 4.1 the maximum local Mach number for stationary three-dimensional modes to exist is $M_x = 1.3574$, hence the values of M_x in Figure 4.8 are valid for the choice of ψ .

Each of these figures shows how a change in one parameter affects the stability of the flow, and in the wavenumber plots the areas of stable and unstable flow are labelled. It is shown that increasing the cone half-angle can be used as a stabilising mechanism, although it does not cause a great change in the magnitude of the effective wavenumber. Decreasing the local Mach number is seen to have a similar consequence. The biggest effect on the value of the wavenumber is seen when varying the wall temperature. The results suggest that wall cooling can be used as an effective stabilising mechanism, which is

consistent with previous findings by Seddougui (1990).

These asymptotic wavenumber and waveangle plots are comparable to the lower branch of the neutral stability curves for stationary modes found by Garrett, Hussain & Stephen (2009). In their study they consider the perturbation equations using numerical methods, then compare the results to the asymptotic results in a high Reynolds number limit (similar to the analysis here). Due to the complexity of the compressible perturbation equations compared to the incompressible equations, no such numerical study has yet been undertaken. However, for any numerical study of the compressible perturbation equations, we would expect the results presented here to be in agreement in the same high Reynolds number limit.

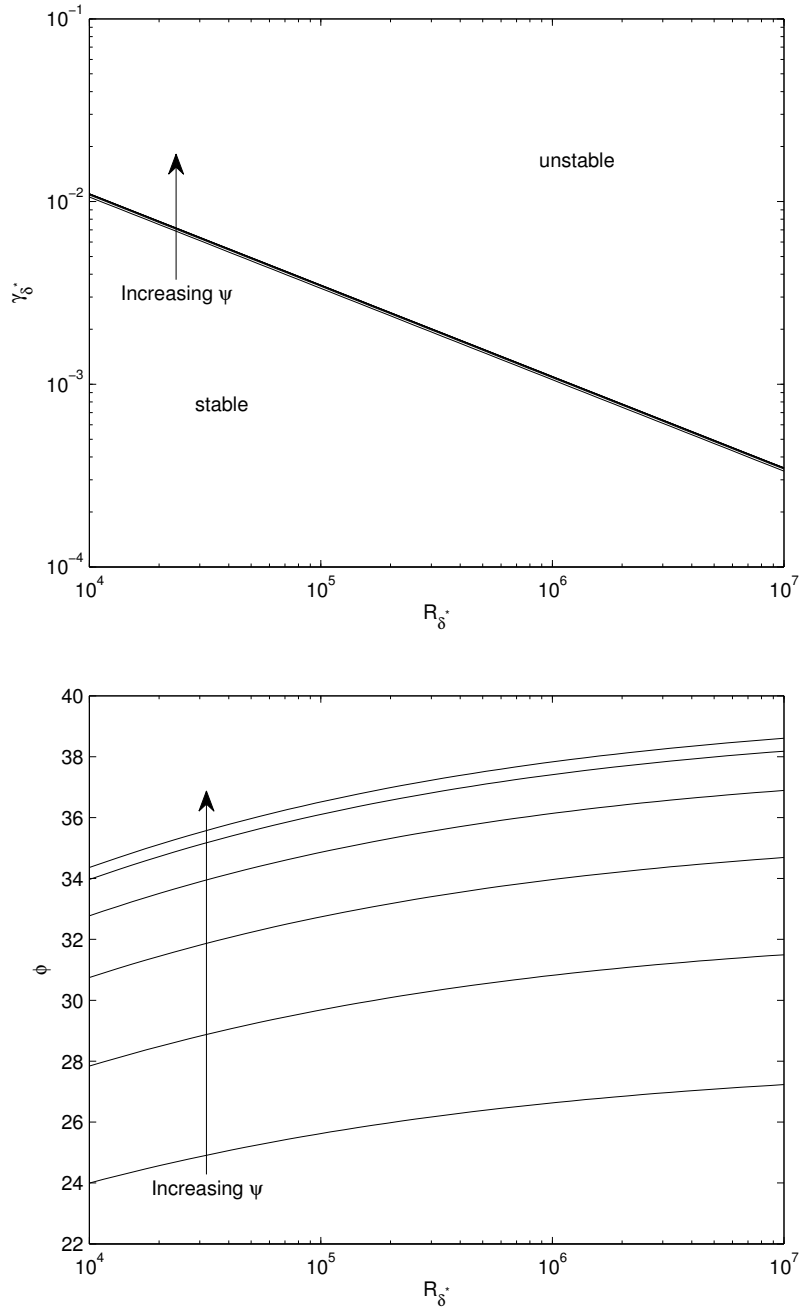


Figure 4.6: Asymptotic wavenumber and waveangle predictions for the viscous type II modes, for fixed $T_w = M_x = 1$ and varying $\psi = 40^\circ - 90^\circ$.

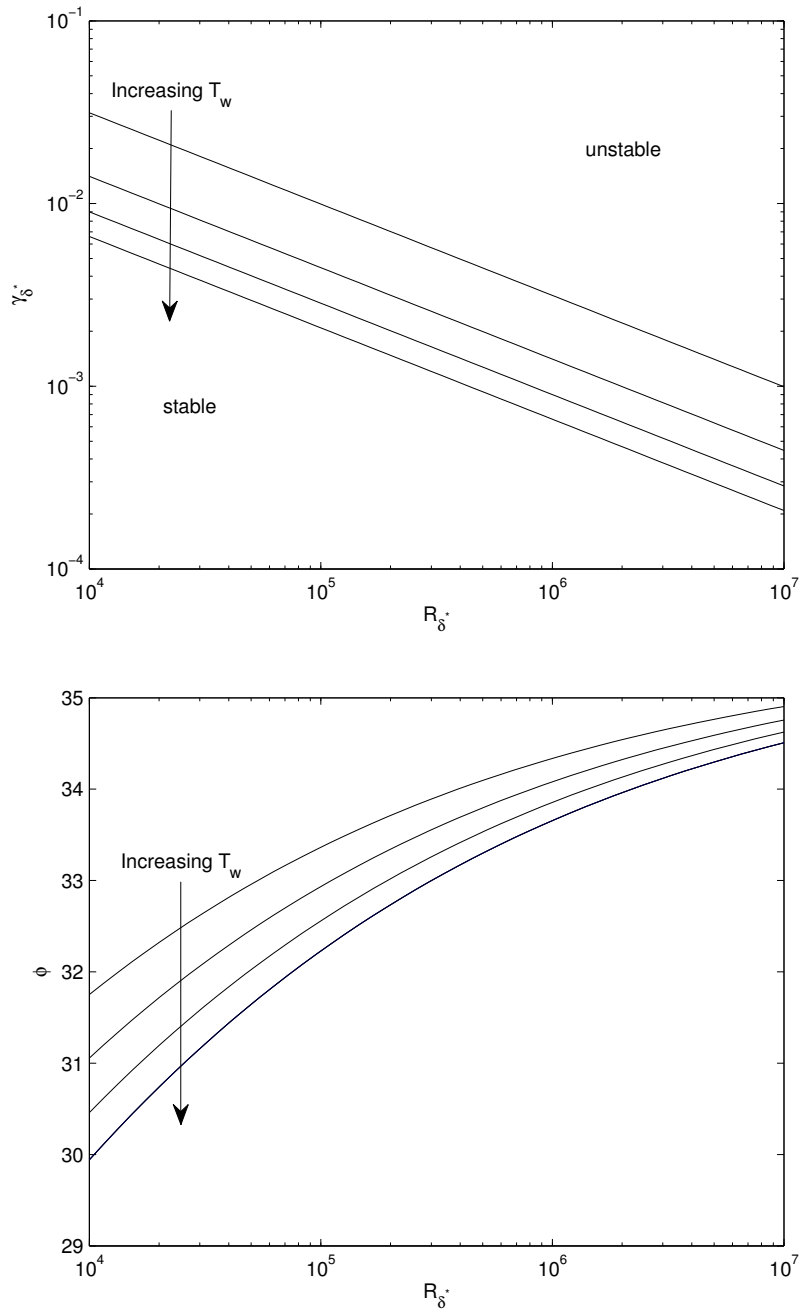


Figure 4.7: Asymptotic wavenumber and waveangle predictions for the viscous type II modes, for fixed $\psi = 60^\circ$, $M_x = 1$ and varying $T_w = 0.4, 0.8, 1.2, 1.6$.

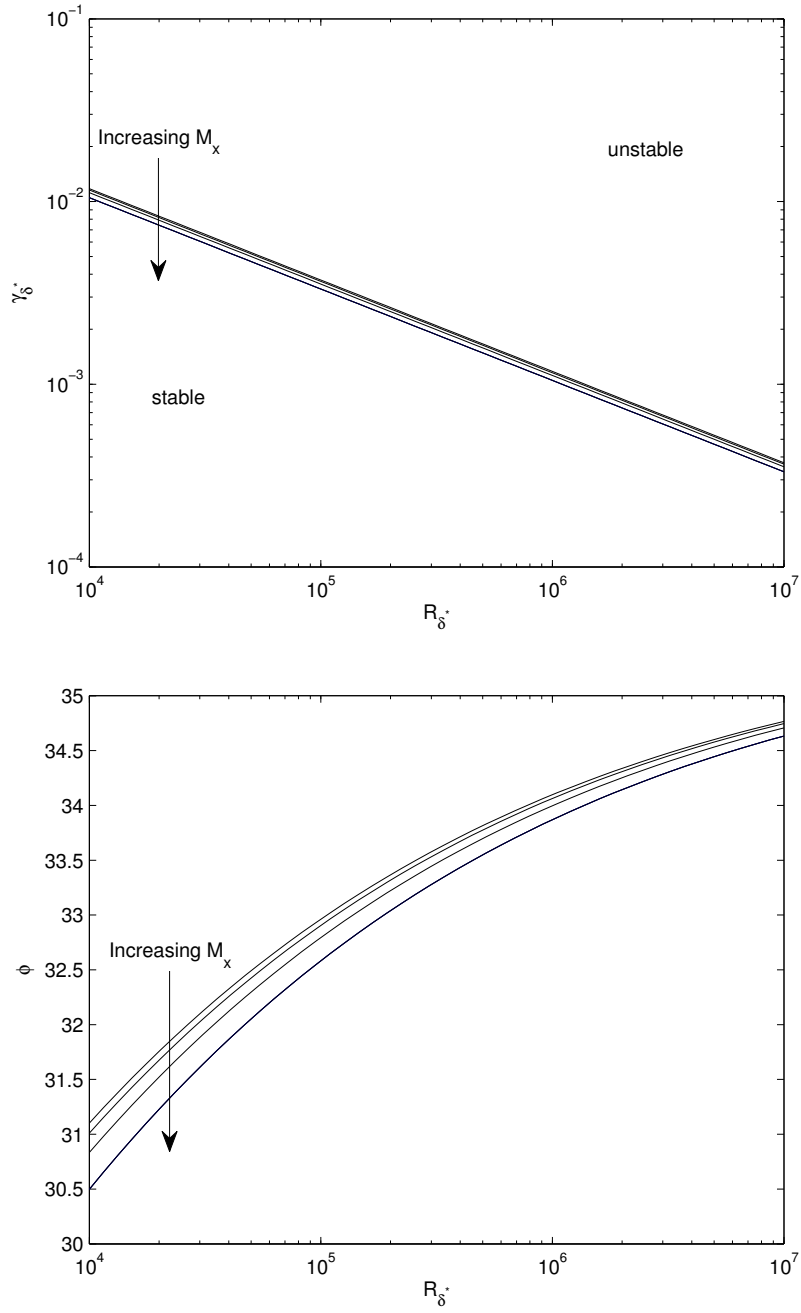


Figure 4.8: Asymptotic wavenumber and waveangle predictions for the viscous type II modes, for fixed $\psi = 60^\circ$, $T_w = 1$ and varying $M_x = 0.3, 0.6, 0.9, 1.2$.

Chapter 5

Conclusions

This thesis consists of a full stability analysis of the compressible boundary-layer flow over a rotating cone, with half-angle $\psi \geq 40^\circ$. The full governing Navier-Stokes equations have been non-dimensionalised. A Doronitsyn-Howarth transformation is used to remove the density quantities, which allows us to obtain the steady basic flow equations within the boundary layer, via the introduction of a stream function which satisfies the continuity equation. The solution to these equations show the laminar flow profiles in the streamwise, azimuthal and normal directions. From the energy equation we also find ODEs in terms of a viscous dissipation quantity and a heat conduction quantity. The solution of these allow us to find the temperature distribution of the flow for specific wall temperatures and local Mach numbers. We introduce a suction

along the cone wall, which is achieved by changing the boundary condition in the normal direction.

We then add a small perturbation field onto the mean flow field and linearise with respect to the perturbation quantities. Hall (1986), Seddougui (1990) and Hussain (2009) have all used the same small expansion parameters, based on the Reynolds number, and here we follow the same method. For a small parameter $\epsilon = R^{-\frac{1}{6}}$ we investigate the inviscidly dominated neutrally stable modes, which we call the inviscid type I modes following the previous literature. The modes appear away from the cone wall and were found using a critical layer analysis similar to that used by Hall (1986), and subsequently Hussain (2009).

Here we note that for the compressible case we have additional terms not found in the incompressible analysis, and naturally this adds complexity not found in the incompressible case. Due to this, the estimates for the wavenumber and waveangles associated with the spiral vortices are only found at leading order, as no satisfactory method has been found to consider the modes at first order. There is a gap in the literature for compressible flows which suggests that an alternative to the method used in the incompressible case is needed but has not yet been found, and this is left as an open problem.

Using a small expansion parameter $\epsilon = R^{-\frac{1}{16}}$ we investigate the wall domi-

nated neutrally stable modes, caused by a viscous–Coriolis force balance, which we label as the viscous type II modes. We proceed by considering a triple-deck analysis similar to that used by Seddougui (1990). This leads to both the leading order and first order estimates for the wavenumber and the waveangles related to the spiral vortices for the type II modes. We then present the lower branch asymptotic neutral curves, as described by Garrett, Hussain & Stephen (2009). We consider the effects of a change in the cone half-angle ψ , as well as how varying the wall temperature or local Mach number changes the flow characteristics.

In §5.1 we compare the results to previous findings, and describe the effect that both the cone half-angle and compressibility have on the flow. Due to there being very limited experimental work on compressible boundary-layer flows over axisymmetric bodies most comparisons will be made with theoretical work. However, it may occasionally be beneficial to consider the experimental work for incompressible flows, and these comparisons will be made where appropriate. In §5.2 we will consider possible routes for further research into compressible boundary-layer flows over a rotating cone.

5.1 Current work

To find the basic flow profiles we non-dimensionalise the full Navier–Stokes equations and make a series of self-consistent assumptions. Through the choices made we find that the laminar flow profiles match those found for the incompressible flow, which have been verified in a number of studies (for examples see Lingwood (1995), Hussain (2009)). However they are still suitable to be used during the stability analysis, as the perturbation equations are formed from the full Navier–Stokes equations and hence do not contain the same assumptions. We also find that through our choice of scalings, the cone half-angle ψ is scaled out of the equations as was also found by Hussain (2009). Therefore the velocity profiles are effectively those found in the case of an incompressible boundary-layer flow over a rotating disk, however they are still valid for our range of cone half-angles.

Temperature distributions are calculated upon solving the basic flow equations and are in agreement with those found by Turkyilmazoglu, Cole & Gajjar (2000). Physical flow profiles are then presented by reversing the Dorotonitsyn–Howarth transformation. The effects of changing the cone half-angle, wall temperature and local Mach number are all considered, where we would expect to see the same changes caused by varying these parameters

follow through to effect the stability characteristics in a similar way. From these profiles there is little change when varying the cone half-angle, an observation which justifies using the laminar flow rotating-disk profiles for the laminar flow rotating-cone due to the cone half-angle being scaled out of the equations. If we then assume that the greater the magnitude of the flow in the normal direction, the more susceptible the flow is to becoming turbulent, then the plots would suggest increasing either the wall temperature or local Mach number to be destabilising. When considering a surface suction it is difficult from the laminar profiles to make any conclusions, and will be reconsidered during the type I analysis.

For the type I modes we can compare our results to those found by Hall (1986) and Hussain (2009) for the incompressible case over a rotating disk and rotating cone respectively. There is currently no full asymptotic analysis into the type I modes for the compressible flow over a rotating disk and this is attributed to the difficulties we have faced. As mentioned by Hussain (2009), the fact that the cone half-angle is scaled out of the laminar flow equations is an advantage to the critical-layer analysis here. The analysis requires the effective velocity and second derivative to be zero at the same point, which is defined as the location of the critical layer. Because there is no dependency on ψ for the laminar flow equations the same is true for the location of the critical

layer, hence it only needs to be calculated for one set of values as opposed to for each cone half-angle.

Our results for the leading-order eigenmode solution in the normal direction w_0 are in good agreement with the incompressible results found by Hall (1986) and Hussain (2009) in terms of the shape of the profile. We find that the peak magnitude of the mode is greater than that of an incompressible flow, and this is plausible as we would expect the effects of compressibility to cause a greater magnitude in flow components as a result of a disturbance. Again from these results it is difficult to make any assumptions with regard to the role of the cone half-angle, however during the type II analysis we shall make some conclusions. Whereas an increase in the local Mach number is seen to have little effect here, a change in the wall temperature causes a noticeable increase in the peak magnitude of w_0 .

The effect of the suction parameter becomes clearer when considering the type I modes. The leading order eigenmode is almost completely dampened by the introduction of a surface suction. This is expected due to previous experimental work by Gregory & Walker (1960) and theoretical work by Lingwood (1997) and Lingwood & Garrett (2011), suggesting a surface suction could be used as a stability mechanism. Without being able to produce the first order correction terms we cannot consider the upper branch of the neutral stability

curve for the compressible case as seen in Garrett, Hussain & Stephen (2009) for the incompressible case.

Before discussing the neutrally stable lower branch modes we note two points of discussion from the analysis. First is the differing value of $F_1^1(0)$ between Hall (1986), Seddougui (1990) and the values found by Hussain (2009) and the study here. We find that $F_1^1(0) = 0.5984$, whereas Seddougui (1990) finds $F_1^1(0) = 0.5991$ which will slightly change the wavenumber and waveangle predictions found. The other point is the value of C used from the Dorotonitsyn-Howarth transformation. We set $C = 1$ all the way through the analysis. Seddougui (1990) does not state a value for C and it remains in her analysis. However, when computing our results we find ours match the incompressible results when setting $T_w = 1$ and $M_x = 0$, and it is assumed that Seddougui (1990) also sets $C = 1$ when finding her results.

A key result from our type II analysis is that the three-dimensional stationary modes do not exist for all local Mach numbers. We take care to ensure the local Mach numbers used are valid for the configuration of parameters used. Our results are consistent with those found by Seddougui (1990) for the compressible boundary-layer flow over a rotating disk, and we are able to see the effects of the cone half-angle. As the cone half-angle is increased we see the region of stability grow which implies that increasing the half angle can be

used as a stability mechanism. This is in agreement with Hussain (2009) for the incompressible case.

We note that we have been concerned with the case of air flow, and hence have set $\sigma = 0.7$ and $\gamma = 1.4$ throughout the analysis. Most gases have values of $\sigma \approx 0.16 - 0.8$ and $\gamma \approx 1 - 1.7$, however changes in these parameters would not cause a great change in the given results. Hence similar qualitative results are expected for all reasonable combinations of σ and γ .

5.2 Future work

When considering the previous literature there are several obvious options to extend the work presented here. In this section we shall describe these perturbations in relation to the previous work and how it will help the understanding of the observed laminar to turbulent transition.

An immediate extension of the type II analysis found here would be to consider the nonlinear terms in the lower deck of the triple-deck analysis. Seddougui (1990) found that for the compressible boundary-layer flow over a rotating disk, the nonlinear effects are destabilising. However the magnitude of the nonlinear effects is found to be dependent upon the wall temperature of the disk. For $T_w > 1$ they were seen to be of less importance than those

found by MacKerrell (1987) for the incompressible case. However, for $T_w < 1$ the nonlinear effects are found to be stronger than in the incompressible case. Whilst we would expect to be in agreement with Seddougui (1990) by expanding our analysis, we would also be able to consider the effect of the cone half-angle on the influence of these nonlinear effects.

A key area for the incompressible boundary-layer flows over rotating cones is the numerical analysis of the perturbation equations. Garrett (2002) derives the incompressible perturbation equations and then uses a set of transformed variables to rewrite the equations as a set of six first-order ordinary differential equations. This was an extension of Lingwood (1995) who used the same method for the case of a rotating disk. Garrett (2002) then solves this sixth-order system numerically and computes the neutral stability curves, including both the inviscid upper branch and the viscous lower branch. As with the asymptotic results found by Hussain (2009), the numerical results are in good agreement with Kobayashi & Izumi (1983) for broad half-angles, however as the half-angle is reduced the numerical results begin to deviate from the experimental results. The numerical results are important as they would verify the asymptotic results found here. However, there is no current numerical analysis of the compressible perturbation equations for these types of flows. This is due to the added complexity of the non-constant density terms which arise due to

the compressibility, and because of this there is no suitable transformation to reduce the equations to a solvable system of ordinary differential equations. Hence an alternative method must be found, and is a possible extension of this work.

As mentioned above, for the incompressible case the analysis presented here leads to results which differ from the experimental findings for smaller half-angles. Hence we expect the same for the compressible case. Kobayashi & Izumi (1983) found experimentally that the nature of the observed spiral vortices is dependent upon the cone half-angle. For $\psi > 30^\circ$ they find the familiar co-rotating crossflow vortices, which approach those found for a rotating disk as $\psi \rightarrow 90^\circ$, as verified by Garrett, Hussain & Stephen (2009). However, for $\psi < 30^\circ$ counter-rotating Görtler vortices are found. This is due to the nature of the instability changing from a crossflow instability to a centrifugal instability. A recent study by Hussain, Stephen & Garrett (2012) describes the analysis needed to capture this centrifugal instability, and deriving a similar compressible analysis would be a natural follow on from the work presented here.

The final suggestion for expanding this work is introducing an oncoming axial flow towards the rotating cone in the streamwise direction. This has been considered for the incompressible boundary-layer flow over a rotating cone

by Garrett (2002) and Hussain (2009) for numerical and asymptotic analyses respectively. For all values of the cone half-angle increasing the strength of the oncoming axial flow is seen to have a stabilising influence. Therefore this area could be of great interest when considering the practical applications.

Bibliography

- ABRAMOWITZ, M. & STEGUN, I. A. 1964 A Handbook of Mathematical Functions. Frankfurt: National Bureau of Standards.
- BERS, A. Linear waves and instabilities. In *Physique des Plasmas* (ed. C. DeWitt, J. Peyraud), Gordon & Breach, Chap. 4.
- BRIGGS, R. J. 1964 Electron stream interaction with plasmas. MIT Press, Chap. 2.
- COCHRAN, W. G. 1934 The flow due to a rotating disk. *Math. Proc. Cambridge Philos. Soc.* **30**, 365–375.
- COLE, J. W. 1995 Hydrodynamic stability of compressible flows. PhD Thesis, University of Exeter.
- DAVIES, C. & CARPENTER, P. W. 2003 Global behaviour correspond-

- ing to the absolute instability of the rotating disk boundary layer. *J. Fluid Mech.* **486**, 287–329.
- GARRETT, S. J. 2002 The stability and transition of the boundary layer on rotating bodies. PhD Thesis, University of Cambridge.
- GARRETT, S. J. 2010 Linear growth rates of types I & II convective modes within the rotating-cone boundary layer. *Fluid Dyn. Res.* **42**, 025504.
- GARRETT, S. J., HUSSAIN, Z. & STEPHEN, S. O. 2009 The crossflow instability of the boundary layer on a rotating cone. *J. Fluid Mech.* **622**, 209–232.
- GARRETT, S. J., HUSSAIN, Z. & STEPHEN, S. O. 2010 Boundary-layer transition on broad cones rotating in an imposed axial flow. *AIAA J.* **48**, 1184–1194.
- GARRETT, S. J. & PEAKE, N. 2007 The absolute instability of the boundary layer on a rotating cone. *Eur. J. Mech. B* **26**, 344–353.
- GREGORY, N., STUART, J. T. & WALKER, W. S. 1955 On the stability of three-dimensional boundary layers with application to the flow due to a rotating disk. *Phil. Trans. R. Soc. Lond. A* **248**, 155–199.

- GREGORY, N. & WALKER, W. S. 1960 Experiments on the effect of suction on the flow due to a rotating disk. *Phil. Trans. R. Soc. Lond.* **248**, 225–234.
- HALL, P. 1986 An investigation of the stationary modes of instability of the boundary layer on a rotating-disk. *Proc. Roy. Soc. London Ser. A.* **406**, 93–106.
- HEALEY, J. J. 2010 Model for unstable global modes in the rotating–disk boundary layer. *J. Fluid Mech.* **663**, 148–159.
- HUERRE, P. & MONKEWITZ, P. A. 1990 Local and global instabilities in spatially developing flows. *Annu. Rev. Fluid Mech.* **22**, 473–537.
- HUSSAIN, Z. 2009 Stability and transition of three dimensional rotating boundary layers. PhD Thesis, University of Birmingham.
- HUSSAIN, Z., STEPHEN, S. O. & GARRETT, S. J. 2012 The centrifugal instability of a slender rotating cone. *J. Alg. Comp. Tech.* **6**, 113–128.
- IMAYAMA, S., ALFREDSSON, P. H. & LINGWOOD, R. J. 2012 A new way to describe the transition characteristics of a rotating–disk boundary–layer flow. *Phys. Fluids.* **24**, 031701.

- IMAYAMA, S., ALFREDSSON, P. H. & LINGWOOD, R. J. 2013
An experimental study of edge effects on rotating-disk transition. *J. Fluid Mech.* **716**, 638–657.
- ITOH 2001 Structure of absolute instability in 3-D boundary layers; part 1. Mathematical formulation. *Trans. Japan. Soc. Aeronaut. Space Sci.* **44**, 96–100.
- ITOH 2001 Structure of absolute instability in 3-D boundary layers; part 2. Application to rotating disk flow. *Trans. Japan. Soc. Aeronaut. Space Sci.* **44**, 101–105.
- KAPPESSER, R., GREIF, R. & CORNET, I. 1973 Mass transfer on rotating cones. *Appl. Sci. Res.* **28**, 442–452.
- KÁRMÁN, T. V. 1921 Über laminare und turbulente Reibung. *Z. Angew. Math. Mech.* **1**, 233–252.
- KOBAYASHI, R., KOHAMA, Y. & KUROSAWA, M. 1983 Boundary layer transition on a rotating cone in axial flow. *J. Fluid Mech.* **127**, 341–352.
- KOBAYASHI, R., KOHAMA, Y. & TAKAMADATE, CH. 1980 Spiral vortices in the boundary layer transition regime on a rotating disk. *Acta Mech.* **35**, 71–82.

- KOBAYASHI, R. & IZUMI, H. 1983 Boundary layer transition on a rotating cone in still fluid. *J. Fluid Mech.* **127**, 353–364.
- KOHAMA, Y. 1984 Study on boundary–layer transition of a rotating disk. *Acta Mech.* **50**, 193–199.
- KOHAMA, Y. 1984 Behaviour of spiral vortices on a rotating cone in axial flow. *Acta Mech.* **51**, 105–117.
- KREITH, F., ELLIS, D. & GIESING, J. 1962 An experimental investigation of the flow engendered by a rotating cone. *Appl. Sci. Res.* **A11**, 430–440.
- LINGWOOD, R. J. 1995 Absolute instability of the boundary layer on a rotating disk. *J. Fluid Mech.* **299**, 17–33.
- LINGWOOD, R. J. An experimental study of absolute instability of the rotating disk boundary layer flow. *J. Fluid Mech.* **314**, 373–405.
- LINGWOOD, R. J. On the effects of suction and injection on the absolute instability of a rotating disk boundary layer. *Phys. Fluids* **9**, 13–17.
- LINGWOOD, R. J. & GARRETT, S. J. 2011 The effects of surface mass flux on the instability of the BEK system of rotating boundary–layer flows. *European J. Mech. B.* **30**, 299–310.

- MACKERRELL, S. O. 1987 A nonlinear asymptotic investigation of the stationary modes of instability of the three dimensional boundary layer on a rotating disk. *Proc. R. Soc. Lond.* **413**, 497–513.
- MALIK, M. R. 1986 The neutral curve for stationary disturbances in rotating-disk flow. *J. Fluid Mech.* **164**, 275–287.
- MALIK, M. R., WILKINSON, S. P. & ORSZAG, S. A. 1981 Instability and transition in rotating disk flow. *AIAA J.* **19**, 1131–1138.
- PIER, B. 2003 Nonlinear waves, secondary instability and transition in a three-dimensional boundary layer. *J. Fluid Mech.* **487**, 315–343.
- REED, H. L. & SARIC W. S. 1989 Stability of three-dimensional boundary layers. *Ann. Rev. Fluid Mech.* **21**, 235–284.
- RILEY, N. 1964 The heat transfer from a rotating disk. *Q. J. Mech. Appl. Math.* **17**, 331–349.
- SEDDOUGUI, S. O. 1990 A nonlinear investigation of the stationary mode of instability of the three dimensional compressible boundary layer due to a rotating disk. *Q. J. Mech. Appl. Math.* **43**, 467–497.
- SMITH, F. T. 1979 Non-parallel flow stability of the Blasius boundary-layer. *Proc. Royal Soc. A* **366**, 91–109.

- SOLAN, A., OLEK, S. & TOREN, M. Rotating compressible flow over an infinite disk. *J. App. Mech. Trans. Asme* **50**, 511–516.
- STEWARTSON, K. 1964 The theory of laminar boundary layers in compressible fluids. Oxford University Press.
- TEIN, C. L. & CAMPBELL, D. T. 1963 Heat and mass transfer from rotating cones. *J. Fluid Mech.* **17**, 105–112.
- TURKYILMAZOGLU, M. 2004 Basic compressible flow over a rotating disk. *Hace. J. Math. Stat.* **33**, 1–10.
- TURKYILMAZOGLU, M. 2005 Lower branch modes of the compressible boundary layer flow due to a rotating disk. *Stud. Appl. Math.* **114**, 17–43.
- TURKYILMAZOGLU, M. 2007 Influence of finite amplitude disturbances on the nonstationary modes of a compressible boundary layer flow. *Stud. Appl. Math.* **118**, 199–220.
- TURKYILMAZOGLU, M., COLE, J. W. & GAJJAR J. S. B. 2000 Absolute and convective instabilities in the compressible boundary layer on a rotating disk. *Theor. Comput. Fluid Dyn.* **14**, 21–37.